5-2014

The Crystal Growth of Cesium Cerium Chloride Scintillator for X-Ray and Gamma-Ray Spectroscopy Applications

Adam Coleman Lindsey
University of Tennessee - Knoxville, alindse9@utk.edu

To the Graduate Council:

I am submitting herewith a thesis written by Adam Coleman Lindsey entitled "The Crystal Growth of Cesium Cerium Chloride Scintillator for X-Ray and Gamma-Ray Spectroscopy Applications." I have examined the final electronic copy of this thesis for form and content and recommend that it be accepted in partial fulfillment of the requirements for the degree of Master of Science, with a major in Materials Science and Engineering.

Mariya Zhuravleva, Major Professor

We have read this thesis and recommend its acceptance:

Charles L. Melcher, Claudia J. Rawn

Accepted for the Council:
Dixie L. Thompson

Vice Provost and Dean of the Graduate School

(Original signatures are on file with official student records.)

The Crystal Growth of Cesium Cerium Chloride Scintillator for X-Ray and Gamma-Ray Spectroscopy Applications

A Thesis Presented for the
Master of Science
Degree
The University of Tennessee, Knoxville

Adam Coleman Lindsey
May 2014

Dedication

For my family and friends who instilled within me a self-respect that pushed me to achieve more than I could have alone. My older brother and two sisters have always been excellent examples to follow in life and they serve as the pillars supporting my confidence that I can make a difference in the world as they have before me. Of course none of us would be here without our parents and I must acknowledge my Mother's love and unwavering support that have helped shape me into the man I am today. My god parents who worked for decades looking after my family during their life, and also in death, your gifts have been seeds that have grown exponentially, and I will always remember to pay this forward.

I wish my late Father could be here to see my progress in the years since his passing and guide me further. He sacrificed much of his life to support my mother and siblings and I know he would be proud. My wife Lisa, who has been with me for over 9 years has been a source of inspiration, encouragement, happiness, hopefulness, and love that have carried me through times of stagnation, apprehension, sadness, anxiety, and fear. I am a greater man because of her.

Acknowledgements

I would like to acknowledge the fine advice of Dr. George Pharr, Dr. Claudia Rawn, and Dr. Veerle Keppens for providing my first consultations prior to entering my studies here at the University of Tennessee and encouraging me to pursue an advanced degree. Additional thanks go to Dr. Rawn for encouraging me to engage fellow students as a mentor, leader, and representative. I would like to acknowledge the support provided by the US Department of Homeland Security, Domestic Nuclear Detection Office under grant # 2012-DN-077-ARI067-02 for funding the project constituting the majority of my research. I would also like to acknowledge the financial support of Siemens Medical Solutions for their contributions to the Scintillation Materials Research Center as well as the Center for Materials Processing which has provided financial support to me and fellow students.

Thank you to Merry Koschan who has always been a source of great advice, critique and inspiration in my research. I wish to also thank the many people at the SMRC who welcomed me to their lab and helped make it my place of work and research. I would like to extend a special thanks to my fellow students that have worked to make this lab what it is today and reminded me that I am never alone in my studies. They are Dr. Harold Rothfuss, Dr. Kan Yang, Hua Wei, Fang Meng, Sam Donnald, Luis Stand, William McAlexander, and my lab sister, Bonnie Blalock. I have shared kind and sobering words with each of you and I deeply appreciate the human element you impart to my experiences here.

I wish to acknowledge the staff at UT that make my research possible. They are the glass blowers Arthur Pratt and Bo Bishop as well as the machinists Larry Smith, Danny Hackworth and Doug Fielden. Their workmanship is an integral part of solving the many engineering problems I have encountered. I wish to thank Frank Holiway for being the “man who gets things” and Randy Stooksbury for being the “man who lets us have the things the department already has”. Without these two, progress would truly be stifled.

A special thank you to Dr. Charles Melcher and Dr. Mariya Zhuravleva for seeing potential in me and supporting me through what I consider to be the most challenging and rewarding few years of my life.

Abstract

The detection and identification of sources of nuclear radiation is an integral tool in defending our nation from threats of nuclear terrorism as well as enforcement of nuclear non-proliferation agreements around the globe. To improve the capabilities in this application, new detection materials surpassing the performance of existing technology utilizing sodium iodide [NaI:Tl] scintillator crystals must be developed and their production cost lowered to meet the demand for the large volumes required. A recently discovered intrinsic scintillation material in the form of crystalline cesium cerium chloride ($CsCe_2Cl_7$) has demonstrated promising performance in the detection of X-ray and gamma ray radiation. In order to assess the potential of this material to be developed into larger scale growth of crystals greater than one cubic inch in volume, research into optimizing the growth processes at smaller volumes is necessary.

Single crystalline boules of $CsCe_2Cl_7$ were grown from the melt in sealed fused silica ampoules using the Bridgman method of crystal growth. A transparent growth furnace along with continuous observation apparatus were developed to aid in the investigation of the growth processes. A comparison of growth and cracking behavior under varied conditions was produced and growth protocols identified which improve crystal boule quality. Crystal quality benefits from controlling the self-seeding process through manipulation and control of critical freezing point isotherms during growth. Cracking appears to originate from aggressive detachment of the crystal from the fused silica ampoule wall while inclusions formed during growth by constitutional supercooling of the melt introduce additional crack nucleation sites through action as stress intensifiers within the bulk matrix. Reducing ampoule volume has a minor effect on cracking severity while additions of excess cesium chloride to the initial mixture produce a greater reduction in cracking. The anisotropic coefficients of thermal expansion as well as the refined crystal structure of cesium cerium chloride have been determined through single crystal Laue and temperature dependent powder X-ray diffraction pattern analyses respectively.

Table of Contents

List of Tables

List of Figures

List of Attachments

Objective

Single crystalline inorganic scintillator materials are widely used as radiation detectors within industries spanning homeland security, natural resource exploration, and medical imaging. In recent years, several new promising scintillator compounds have been discovered. This work addresses a grand challenge in radiation detection for national security applications: the development of a gamma-ray sensitive detection material that can achieve ≤1% energy resolution at 662 keV at room temperature and can be produced in large volume at low to moderate cost. Large volume is considered to be 1 cubic inch but could in principle be grown in much larger volumes. As part of a broad project focused on identifying a small number of novel materials with potential for further development into growth processes approaching the goal of 1 cubic inch, experimental growth of single crystals from the melt in small volumes coupled with relevant material property research is a necessary requirement to assess issues affecting yield and development of basic protocols for practical growth at larger volumes.

$CsCe_2Cl_7$, discovered recently as a promising intrinsic scintillator exhibits attractive performance with a fast decay time, good light yield, and emission wavelength suitable for efficient use with conventional photomultiplier tubes used in scintillator based detectors of X-ray and gamma-ray radiation. The hygroscopic nature of metal halides requires protection from ambient moisture to prevent degradation affecting scintillation performance and the very low hygroscopicity of $CsCe_2Cl_7$ in comparison with most other compositions in this class of materials is advantageous and provides additional motivation for investigation.

Efforts to grow this material cite its tendency to crack upon cooling when using the Czochralski method which results in decreased crystalline quality thereby limiting the material's scintillation performance and viability for future development. This thesis is comprised of a detailed comparison of crystal growth experiments aimed at improving the crystalline quality with respect to the growth procedures and an assessment of what improvements could be made through knowledge of the defect formation mechanisms governing polycrystallinity, inclusion formation, and cracking. Additionally, this study is intended to fill gaps in the scientific literature comprising the structural, thermodynamic, and thermophysical properties of $CsCe_2Cl_7$ relevant to single crystal synthesis and implementation into detector applications. Through the use of a transparent growth station commonly employed in research laboratories, direct and continuous observations of growth processes affecting crystal quality will be acquired to aid in the investigation. The thermal fields within growth stations will be measured and modeled to design suitable growth processes that maximize yield. In order to investigate the crystal structure and anisotropic thermal expansion behavior, single crystal Laue diffraction as well as high temperature x-ray powder diffraction analyses will be performed respectively. In addition to this, the thermodynamic behavior of melting and freezing will be investigated with differential scanning calorimetry. This method of investigation will provide a deeper understanding of material behavior pertaining to single crystal synthesis and can be readily applied to a wide array of compositions grown from the melt.

Chapter 1: Introduction to Radiation Detection

Electromagnetic radiation in the form of X-ray and gamma ray radiation lies outside the visible spectrum and is present in nature as naturally occurring cosmic radiation as well as the radioactive decay of naturally occurring elements found in the earth's crust that are typically enriched for use as fuel in nuclear reactors. Other sources of potentially lethal radiation come from various man-made fission products produced in nuclear reactors and their daughter nuclides possibly used in nuclear weaponry. Regardless of the source, electromagnetic radiation with energies ranging from a few hundred of electron volts (eV) to several million electron volts (MeV) is highly penetrating and ionizing to the matter it interacts with, and because of this, there exists significant challenges to the safe containment and shielding of radioactive material with regards to the hazards it presents to biological organisms. As a consequence of the highly penetrating nature of electromagnetic radiation, the accurate detection and identification of sources is also made challenging. However, it is also this quality that presents many important uses to society and various means of utilizing electromagnetic radiation have been developed over the past century.

1.1 Application

The subject of this study pertains to research and development of detection materials for use in homeland security applications where efficient detection and identification of nuclear radiation is the key function. Detectors of this type are implemented at thousands of locations ranging from security checkpoints at airport or ground transport terminals, border crossings, population centers, as well as weigh stations in order to identify radioactive contraband being transported or shipped by individuals aimed at using them for illicit purposes such as in nuclear weaponry for state warfare or acts of terrorism. Portable configurations of detectors ranging from ground or air vehicle mounted systems to backpack and handheld units capable of identifying radioisotopes in various conditions are required for inspections of areas suspected of processing or harboring illegal nuclear radioactive contraband as a method to enforce nuclear non-proliferation agreements around the globe. As a result, detectors used in this application must be supplied in large volumes possessing a marriage of low cost of production with detector performance.

Presently, the best technology currently available for radionuclide identification is based upon the use of high purity germanium (HPGe) semiconductor based detectors. However, the ultra-high purity germanium required for production and cryogenic operating temperatures make this technology prohibitively expensive for practical deployment for use in national security applications. As a result, cheaper alternatives are needed which still provide functional radionuclide identification and scintillator based detectors provide a significantly lower cost of production and operation (*1*).

1.2 Scintillator Based Detectors

Inorganic single crystal scintillators have been in use for decades to detect X-ray and gamma-ray radiation as they provide an efficient means of converting the high energy electromagnetic radiation into visible photons of light. Scintillators absorb individual quanta of high energy X-rays or gamma rays and respond through emission of a pulse of many quanta of lower energy electromagnetic radiation in form of visible photons. The visible photons must be converted into electrons in order to be quickly measured and recorded by observation devices and thus belong to the indirect detector category. This is typically accomplished through coupling the scintillator to a photo-multiplier-tube (PMT) whereby scintillation photons which strike a photocathode cause an electron to be emitted through the photoelectric effect. The

photoelectron is then accelerated by electrostatic potential toward several dynodes in the PMT which multiply it through sequential stages into millions of electrons that ultimately flow to the anode producing a current pulse signal for further processing by amplifiers, timing circuitry, and a multichannel analyzer (*2*). Through this process, the number of emitted scintillation photons as a response to ionizing radiation is proportional to the current signal registered in the aforementioned electronics.

For spectroscopy applications requiring fast and efficient radionuclide identification, the scintillator material must possess in general:

- A high density and effective Z number to provide good stopping power and probability of interaction with high energy X-ray and gamma-ray radiation.
- A high light yield to produce enough photoelectrons for subsequent processing by appropriate electronic circuitry.
- A high energy resolution or ability to resolve different energies of ionizing radiation which provide the signature of the radionuclide source(s).
- Cost effective means of production of single crystals to provide large volumes of material for various detector configurations.

Many inorganic crystalline scintillators have been discovered yet no single one offers the best performance in all categories for security applications. Consequently, amongst all crystalline scintillator materials, the metal halides possess a marriage of high light yield and best achievable energy resolution to date (*3*) and thus are well suited for spectroscopy despite lower densities typically under 5.5 g/cm^3. In comparison with oxide based scintillators that possess higher densities, only a few have demonstrated comparable energy resolution and light yield to metal halides such as cerium activated yttrium aluminum perovskite ($YAlO_3$:Ce or YAP) yet their higher melting point (~1900°C) introduces considerable cost to production of large volumes of single crystals and thus cannot compete with the cost of production of metal halides possessing a lower melting point (typically <1000°C) (*4*).

1.3 Single Crystalline Metal Halide Scintillators

For decades, thallium activated sodium iodide (NaI:Tl), first discovered by Hofstedter in 1948 (*5*), has been used in detectors across many applications. However, the poor energy resolution of this material of ≈7% at 662 keV from a ^{137}Cs source limits its performance in radionuclide identification which has motivated the search for other materials with better performance to replace it (*6*). In recent years, many novel metal halides have been developed yet have struggled to replace NaI:Tl due to difficulties and subsequent cost in production of large volume (> 1 cubic inch) single crystals. Cerium activated lanthanum bromide ($LaBr_3$:Ce) as well as the intrinsic scintillator cerium bromide ($CeBr_3$) both offer very good energy resolution of approximately 3% and 4% at 662 keV respectively yet because of their similar hexagonal structure, each have a weak cleavage plane that makes growth of uncracked single crystals difficult and costly. Over many years of research, the growth processes developed by company Saint-Gobain has yielded 3.5 inch diameter boules (*7, 8*). Because of the fragility and tendency to crack during growth, research into strengthening the material through aliovalent doping in parts per million (ppm) levels has achieved some improvement (*9*) yet costs of production remain prohibitively high for use in large detectors for security applications.

One of the best performing scintillators in terms of energy resolution is europium doped strontium iodide (SrI_2:Eu) which can achieve <3% energy resolution at 662 keV yet crystal growth processes for 1-2 inch diameter uncracked boules remains difficult and is limited to a few examples in literature (*10-13*). Thus for SrI_2:Eu, research to improve growth processes which increase the yield at larger diameters are required and ongoing. Another newly developed class of materials possessing the cubic crystal structure is the elpasolites family containing compounds such as cerium activated cesium lithium yttrium chloride (Cs_2LiYCl_6:Ce or CLYC). This scintillation material can be used for detection of neutrons due to the large neutron cross-section through the intrinsic incorporation of ^6Li into the matrix as well as a very efficient response to gamma-rays with an energy resolution of ~4% at 662 keV. Production of 1-2 inch diameter boules has been developed by Radiation Monitoring Devices Inc. over the last decade yet research continues to improve the energy resolution and growth process (*14*). Table 1 below shows a comparison of scintillation properties of NaI:Tl, $LaBr_3$, SrI_2:Eu and CLYC.

Table 1. Comparison of Properties of Metal Halide Scintillators in Advanced Development

	NaI:Tl	$LaBr_3$:Ce	SrI_2:Eu	CLYC
Density (g/cm^3)	3.67	5.29	4.59	3.31
Decay time (ns)	240	26	1100	70
Light Yield (ph/MeV)	39,000	63,000	90,000	20,000
E_{res} at 662 keV	7%	<3%	<3%	~4%
Wavelength (nm)	415	380	435	374, 409
Reference	(*7*)	(*7*)	(*15*)	(*14*)

Many newly discovered materials have offered improvements over NaI:Tl with energy resolutions below 5% at 662 keV. However, further research is necessary to determine successful growth parameters that optimize their yield before being considered for larger scale production. For example, they include but are not limited to the recently discovered europium activated cesium barium iodide and mixed halide barium bromide iodide ($CsBa_2I_5$:Eu and BaBrI:Eu respectively) (*16*). Europium activated barium chloride ($BaCl_2$:Eu), despite the reported energy resolution 3.5% at 662 keV, the compound possesses a high temperature phase transition which stands as an obstacle to growth of large uncracked single crystals (*17*).

As a result of the recent surge of newly discovered scintillation materials, many require further research beyond the discovery and characterization phase to determine and justify further development procedures. Moreover, this may occur through gains to the scintillation performance, yield in growth processes, or both through subsequent research in determining and overcoming the obstacles preventing those gains. One such newly discovered intrinsic scintillator, cesium cerium chloride ($CsCe_2Cl_7$), has been reported to possess promising performance by Rooh et al (*18*) as well as Zhuravleva et al (*19*) yet cite poor quality of the crystal. The following chapters present a study comprised of crystal growth experiments as well as the thermophysical, structural, and thermodynamic investigation of $CsCe_2Cl_7$ as it pertains to the potential for

further development into larger volume (>1 cubic inch) growth for use in homeland security applications of radioisotope identification through X-ray and gamma-ray spectroscopy.

Chapter 2: Crystal Growth

2.1 Growth Mechanics and Methods

2.1.1 Thermodynamics governing phase transformations

In order to begin a discussion of crystal growth, a transformation from the liquid or melt phase to the solid or crystal phase, a brief description of matter and its variable forms must be established. The following section provides a basic description of how the existence of a phase is dependent upon temperature and pressure and how the transformation from one phase to another is governed by the laws of thermodynamics.

The Gibbs-Helmholtz equation is given by:

$$\Delta G = \Delta U - T\Delta S + P\Delta V = \Delta H - T\Delta S < 0 \qquad (1)$$

This equation was developed by thermodynamicist Josiah Willard Gibbs and physicist Hermann von Helmholtz to determine the amount of free energy available in a system to do work. It states that the free energy of a system (G) is a function of the system's internal energy (U), temperature (T), the system's entropy (S), pressure (P), and volume (V). The enthalpy term (H) is convenient to use instead of the internal energy, pressure, and volume terms. Furthermore, for crystal growth in a sealed and rigid container, the pressure and volume may be considered as constant or otherwise contributing a negligible amount to the enthalpy thus reducing the free energy dependence of the system to the internal energy (heat), temperature, and entropy term. When considering the free energy of two different phases, as in the crystalline and melt phases in the context of crystal growth, one phase will possess a lower free energy than the other for a given temperature. For a phase to transform into another spontaneously, this free energy must be reduced. It is by the governing thermodynamic principles found in (1) that the increase in temperature above the melting point of a crystalline solid will spontaneously cause a transformation into the melt phase and vice versa.

Metal halides and their compounds are primarily comprised of elements from the alkali metals in group I, alkaline earth metals in group II and the halides in group VIIA of the periodic table. They form a highly ordered crystalline phase upon cooling and thus upon solidification, the entropy or disorder is thereby reduced making the ΔS term in equation (1) negative upon solidification. Therefore a reduction in the free energy is facilitated by the loss of heat during fusion (latent heat of fusion) and this transfer of heat out of the solidifying melt is the primary means of controlling the crystal growth process. Moreover, a study of the experimental methods and equipment for controlled crystal growth of one ternary lanthanide metal halide, $CsCe_2Cl_7$, using the Bridgman method is the subject of this thesis.

2.1.2 Analysis of the CsCl-$CeCl_3$ Phase Diagram

The CsCl-$CeCl_3$ pseudo-binary phase diagram illustrated in Figure 1 was first experimentally established by Sun and Morozov (*20*) and then later refined with thermodynamic calculations and calorimetry experiments by Kapala and Rutkowska (*21*). Compound formation free energies for the system have been thoroughly investigated and reported by Guane-Escard et al (*22*) along with earlier work by Papatheodorou and Kleppa (*23*).

This system contains two congruently melting compounds, the aforementioned $CsCe_2Cl_7$, and Cs_3CeCl_6 with a stoichiometric $CeCl_3$ to CsCl ratio of 2:1 and 1:3 respectively. The third compound Cs_2CeCl_5 does not melt congruently and thus cannot be grown from the melt. The lower left of the phase diagram features a solid to solid phase transition for the Cs_3CeCl_6 compound at approximately 673 K which is comprised of a pseudo-cubic to monoclinic structure transformation known to cause destruction to the higher symmetry phase grown from the melt which is unstable at the transition temperature (*24*). As a result, the growth of the Cs_3CeCl_6 compound from the melt presents an unavoidable obstacle to production of high quality bulk single crystals.

The $CsCe_2Cl_7$ compound on the right side of the phase diagram melts congruently at 945K (672°C), and possesses no solid to solid phase transformations therefore the growth of bulk crystals from the melt is possible. One interesting feature of this compound is its close proximity to the eutectic composition and temperature. If careful control of the melt composition is not maintained, the formation of the eutectic may be possible due to a deficiency of the CsCl component. As a result of this, synthesis of the $CsCe_2Cl_7$ compound is more sensitive to the starting mixture in comparison to the Cs_3CeCl_6 compound.

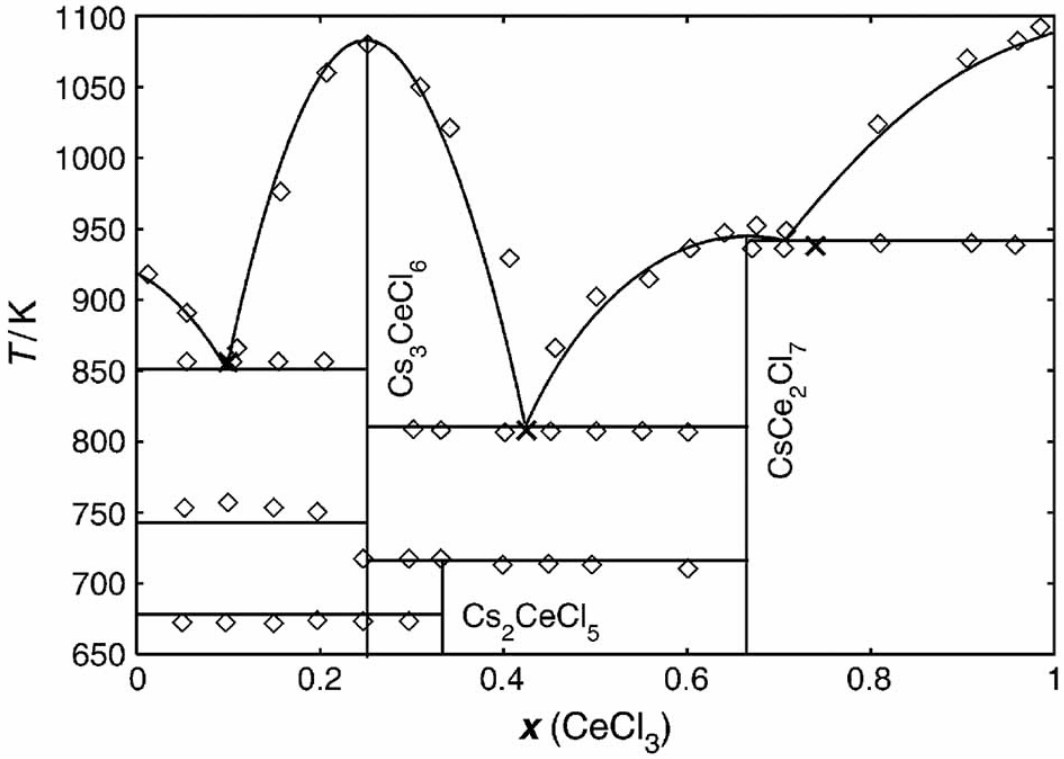

Figure 1. The Binary CsCl-$CeCl_3$ phase diagram containing congruent and incongruent compounds, as well as several eutectics. The lines are calculated phase boundaries with diamonds representing experimental data and X's the eutectics. Image taken from (*21*).

2.1.3 Methods of Bulk Crystal Growth for Metal Halides

While there are many methods to produce crystals of metal halides, few methods are suitable for production of single crystals for use in scintillator based detectors requiring dimensions larger than a few cm^3. For example, in the solution growth method, components dissolved in a solvent to a critical saturation level and then cooled and allowed to solidify around a seed crystal may produce crystals under very low thermal gradient conditions which are favorable; however growth rates of 1-2 mm/day are too slow for large yields required by industry. The Czochralski growth method consisting of a crystal which is "pulled" from the melt contained in a heated crucible is widely used in industry for the production of oxides yet has seen limited use for metal halide growth (*4*). While heating of the crucible can be achieved through inductive coils or resistive heating, these growth stations typically require seed or crucible rotation and translation mechanisms in addition to a force gauge to measure the mass of the growing crystal as part of the boule diameter control. As a result, the major disadvantage to the Czochralski growth method is the high cost of the multiple control systems. Furthermore, metal halides are susceptible to degradation in the presence of moisture or oxygen at high temperatures and thus the growth chamber must be supplied with an inert or halide gas atmosphere in addition to special material handling procedures needed to load the material into the crucible.

For crystal growth of metal halides with melting points at or below 1000°C, crystal growth from the melt in sealed ampoules within resistively heated furnaces provides an economical and efficient means of preventing degradation of the material while facilitating the growth of large diameter crystals at rates of a few cm per day. A method whereby a charge of molten metal within an ampoule or crucible traverses through a furnace and allowed to directionally solidify into a single crystal was first described by Bridgman in the early 20th century (*25*) and then later modified by Stockbarger to achieve improved results for lithium fluoride crystals some years later (*26*). A schematic of the Bridgman growth station with the modifications developed by Stockbarger is shown in Figure 2. The basic concept of this method involves placing a molten charge into a furnace with a temperature above the melting point of the material and slowly lowering the charge into a cooler area of the furnace so the charge freezes from the bottom up. The material to be grown is typically contained in a sealed cylindrical ampoule to prevent exposure to ambient conditions and to aid in extraction of the crystal after growth. Consequently, materials which may oxidize or degrade in atmosphere at high temperatures are best suited for this method as the ampoules can be evacuated or filled with an inert gas. Stockbarger's modification to the Bridgman apparatus created larger thermal gradients by introducing a second furnace and a diaphragm in between to shield and isolate the heat of one furnace from the other. Since the development of this method nearly a century ago, the basic equipment design and arrangement have changed very little owing to the inherent simplicity of the technique and as a result, the cost of producing a growth station using this method continues to be a cost efficient means of producing single crystals of new materials.

The only parameters necessary to control the growth process are the furnace temperatures and the motion of the ampoule through the established temperature gradient. A single grain may be obtained by growing from a seed crystal located in the lowest portion but poses some technical difficulty in preparing and positioning the seed so that it is not destroyed in the process of melting the primary charge. In the absence of a seed crystal, the melt at the lowest extremity can be frozen into numerous crystallites and subsequent competitive growth within the capillary causes a dominant grain to be isolated by use of restricting

geometry in the form of a necked region so that only a single grain emerges thereby producing a crystal with a random orientation. Once the crystal is grown, the cooler zone of the furnace can be used for further annealing and cooling to room temperature. Typical furnaces use resistive heating of a cylindrical bore with axial thermal gradients in the range of 10°C/cm and translation rates of approximately 1 mm/hr. Ampoules can be constructed with combinations of fused silica, platinum, and or glassy carbon depending on the material requirements.

One disadvantage with the Bridgman Stockbarger method is unwanted crystal nucleation and defect formation through interactions of the growing crystal interface with the ampoule walls and can be avoided by maintaining a flat or slightly convex interface shape throughout growth (*27, 28*). Chang and Wilcox (*27*) developed a simple relationship between the hot and cold zone temperatures for controlling the interface shape making the following assumptions; the thermal properties of the melt, crystal, and ampoule are equal, the ampoule is not moving, and convective flows are minimal. This relationship is given by:

$$\phi = \frac{T_m - T_c}{T_h - T_c} \qquad (2)$$

In equation 2, T_m is the melting or freezing temperature, while T_c and T_h are the temperatures of the cold zone and hot zone respectively. Chang illustrates that for a flat interface, which generally produce minimal thermal stresses, values of ϕ close to 0.5 are required while a convex interface is produced for ϕ values larger than 0.5. Beginning with an interface within the cold zone, the temperature of one or each zone can be increased to achieve a flattened or convex interface. In this manner, an approximation of zone settings in which the shape of the interface shape and position is controlled throughout growth can be achieved by only knowing the melting or freezing point of the material. In chapter 4, a detailed discussion of growth of single crystals of $CsCe_2Cl_7$ within a transparent two-zone vertical Bridgman furnace will be provided.

2.2 Factors Affecting Crystal Quality

2.2.1 Supercooling

In the process of solidifying a melt, the temperature at which crystallization begins may deviate from the melting temperature of the solid phase. The term supercooling or undercooling in liquids refers to the phenomenon of the liquid cooling below an equilibrium temperature, or melting temperature of the solid. The phenomenon of supercooling has been observed in all liquids and is seen generally to be more severe in multicomponent melt compositions with complex crystal structures and is less easily induced in highly pure single component systems with highly symmetrical crystal structures (*29*). The degree of supercooling can vary between a few degrees and several hundred degrees below the melting temperature (*30*). For all compositions, the determination of a characteristic supercooling, or magnitude of the temperature difference between the melting or freezing points, can be obtained through differential scanning calorimetry (DSC) measurements and thus provide an important parameter when designing

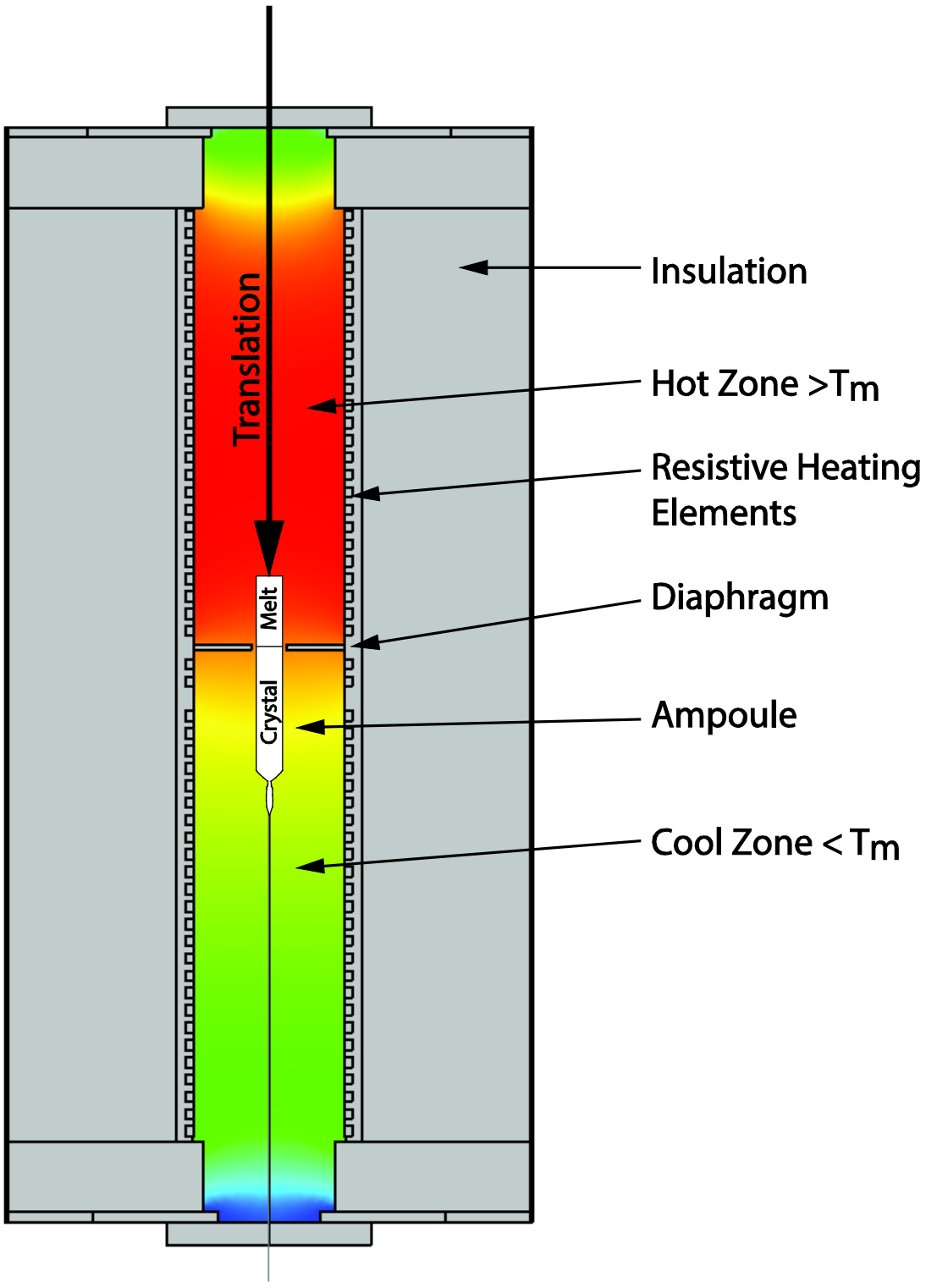

Figure 2. Schematic of a Bridgman-Stockbarger Crystal Growth Station

crystal growth apparatus. The following is a brief description of the general principle and the implications for crystal growth. When a liquid is cooled below its equilibrium temperature it is said to be in a metastable state. Further cooling increases the instability until a critical temperature is reached whereby crystallization occurs spontaneously. Furthermore, the geometry of the container supporting the supercooled melt may provide an adequate nucleation site to initiate formation of a crystallite thereby promoting heterogeneous nucleation of the solid phase. In the absence of container geometry (ampoule wall or crucible), impurities or otherwise a seed crystal, the supercooled melt will spontaneously nucleate numerous crystallites homogeneously throughout the bulk volume. With scintillation materials, the presence of grain boundaries between individual crystallites create excess light scattering of the scintillation light emission and thus reduce the efficiency of light collection. As a result of this, when designing a growth process for melts exhibiting a large characteristic supercooling as illustrated in Figure 3, special attention must be given to the seeding, or nucleation process. The unique geometries which facilitate heterogeneous nucleation in the absence of a seed within undercooled melts will be treated in a later section in Chapter 3. Another mechanism which produces deviations in the freezing temperature for impure melts is described in the next section.

2.2.2 Constitutional Supercooling

Theories describing the behavior of melts containing impurities or otherwise a solute within a solvent system upon solidification have been developed over several decades which first began by rigorous studies by Tiller, Jackson, Rutter, and Chalmers (*31*) and later on developed by Hurle (*32*) for melts in which mixing plays a larger role of solute distribution. Chalmers coined the term constitutional supercooling to describe the behavior of a melt containing solute or impurity concentration inhomogeneity after decanting studies (*33*) provided evidence that a solid/liquid interface may develop three dimensional features which were the product of local perturbations in the equilibrium temperature of the liquid due to the build-up of solute rejected by the growing crystal.

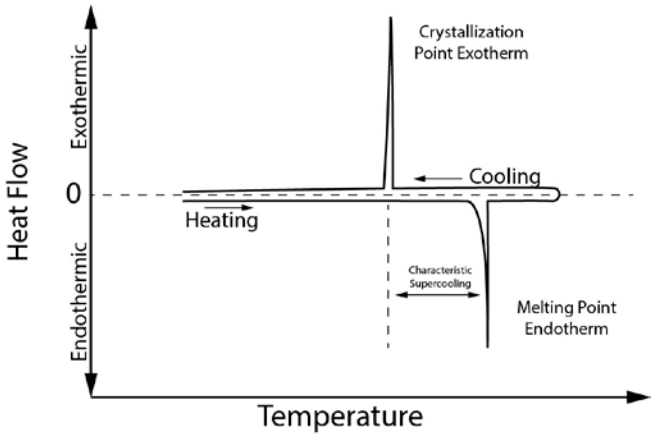

Figure 3. Differential Scanning Calorimetry measurement of the melting and freezing (endothermic and exothermic peaks) of a material exhibiting a characteristic supercooling.

The presence of this effect was shown to be dependent on the speed of the growth, initial concentrations of solute, and the temperature gradient surrounding the growth interface and extending into the melt. In cases of bulk crystal growth, the solute can be considered an impurity in the mixture that is introduced either intentionally as a dopant or as contamination through synthesis processes or degradation and thus the theories describing this phenomenon may apply to many materials and explain the cause for many defects witnessed in actual crystal growth (*34, 35*). An illustration of defects produced in metal halide single crystals by constitutional supercooling can be seen in Figure 4.

As illustrated in Figure 4, the inclusions caused by constitutional supercooling of the melt produce light scattering sites in the crystal which are deleterious to scintillation performance. A brief explanation of the theory of constitutional supercooling and how it applies to crystal growth now follows.

A schematic of the liquidus and solidus equilibrium temperatures for varying concentration of an impurity solute is shown in Figure 5 and the left side depicts a system where the solubility of the impurity in the liquid phase is larger than in the solid. In this system as the melt begins to freeze, the solid phase formed will have a lower concentration of the solute. As more solid phase is grown, the melt phase becomes richer in solute and thus the equilibrium temperature decreases. This behavior is due to the segregation behavior of the solute whereby the segregation coefficient, k, is less than unity and is defined as:

$$C = kC_0(1-g)^{k-1} \qquad (3)$$

In this equation, the concentration of solute in the crystal is C, with C_0 the initial solute concentration in the melt, and g, the fraction of melt solidified. The inverse behavior whereby the solubility of the solute is greater in the crystal than in the liquid is shown in the right hand side of Figure 5.

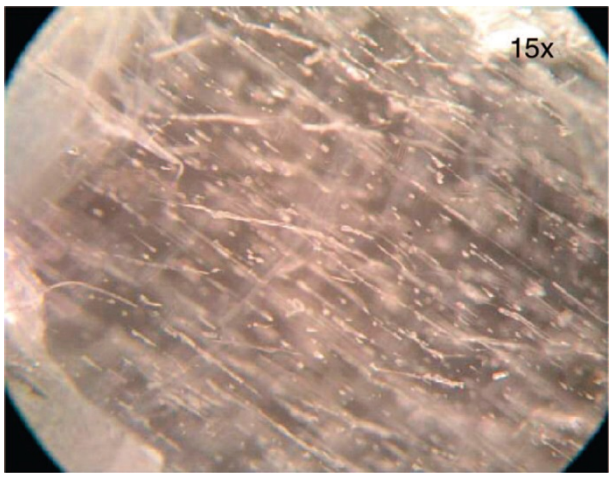

Figure 4. Melt inclusions caused by constitutional supercooling seen under magnification in $LaBr_3$. Image of taken from (*36*).

Given the relationship in equation (3), for segregation coefficients of k < 1, the slope of the liquidus equilibrium temperature versus solute concentration is m < 0, and the equilibrium liquidus temperature throughout the melt at point x is given by:

$$T_x^E = T^0 + mC_x \qquad (4)$$

In equation (4), T^0 is the melting temperature of the pure solvent and C_x is the concentration of solute at point x in the melt (*31*). These equations developed by Tiller assume that diffusion and convection are not enough to thoroughly diffuse the solute evenly throughout the melt and thus the equilibrium liquidus temperature will be lowest close to the interface, and as the solute concentration "decays" with distance from the interface a corresponding increase in the liquidus equilibrium temperature occurs. This is illustrated in Figure 6. If a large enough thermal gradient parallel to the interface growth direction is present, the melt will not be constitutionally supercooled and the interface will remain stable. If this thermal gradient is not sufficient, the melt ahead of the interface will become supercooled and can solidify producing protuberances from an otherwise featureless interface. The protuberances extend into the melt further than the surrounding interface and can cause additional supercooling and subsequently the protuberance will continue to grow and produce irregularities in the solidified structure (*30*). An illustration of this is shown in Figure 7.

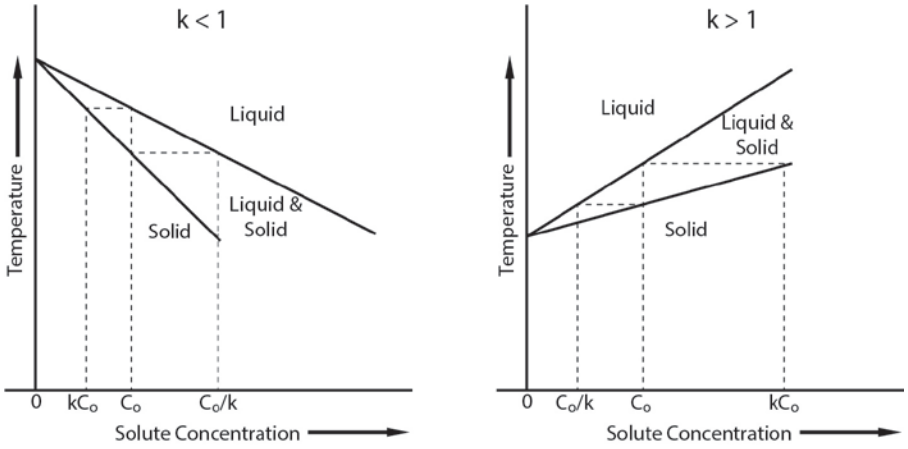

Figure 5. Constitutional diagram for a solute which lowers the freezing point (left) and one which raises the freezing point (right). Adapted from (*31*).

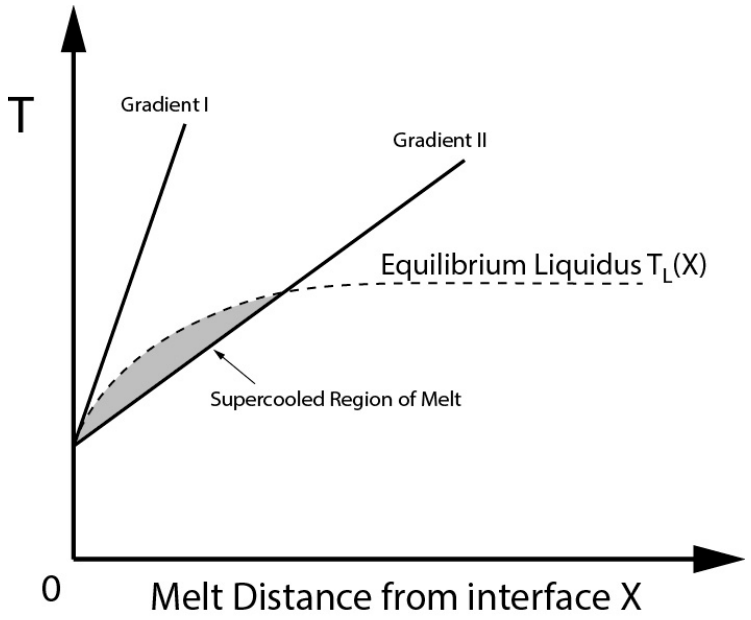

Figure 6. The equilibrium liquidus temperature for a melt with decreasing solute concentrations away from the growth interface show with Gradient I (sufficient thermal gradient) and Gradient II which produces constitutional supercooling ahead of the growth interface.

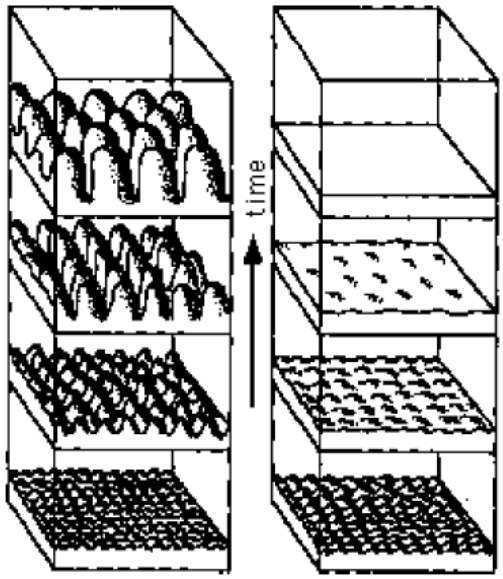

Figure 7. Protuberances along the growth interface for an unstable interface (left), and a stable interface (right). Adapted from (19).

In practice, a crystal grower must determine the necessary thermal gradient as well as the growth rate for a given material that prevents instability. Tiller et al (*31*) originally derived the criterion for marginal stability with respect to constitutional supercooling for motionless melts as given by:

$$\frac{G^*}{v} = \frac{m_l}{D_l}\left(\frac{k_0 - 1}{k_0}\right)C_0 \qquad (5)$$

Equation (5) provides a relationship for the limiting marginal stability in terms of the minimal gradient, G^*, the growth rate, v, for a solute-solvent system with liquidus slope m_l, a solute diffusion coefficient D_l, with initial concentration C_0 and segregation coefficient k_0. This relationship dictates that a solid-liquid interface (SLI) will be more resilient to disturbances by requiring smaller G^*/v values. From a feasibility standpoint, the costs associated with the growth process are most closely limited by the thermal gradients achievable by the growth furnaces and the rates of production, or stated more simply, the ratio of G^*/v.

The theories developed to describe constitutional supercooling phenomenon provide a simplified concept that may guide the development of stable growth processes. The next section will briefly describe defects relevant to bulk crystal growth of scintillation materials and possible causes.

2.2.3 Defect Formations

Many impurity type defects may be introduced prior to and during synthesis due to exposure to moisture causing hydrolysis of the metal cation (*37*) and prolonged exposure to oxygen at high temperatures may cause formations of metal-oxides. As a result of this, the removal of oxygen and adhered trace moisture on the raw metal halide precursor materials is crucial to prevention of contamination during synthesis. During synthesis, precursor materials of binary or ternary compounds are mixed together according to the stoichiometric balance of the desired compound and heated to a molten state where new bonds are formed during the chemical reaction process. Incomplete synthesis due to improper mixing of a multicomponent mixture in addition to shifts from stoichiometry caused by the disproportionate volatilization of one species will produce melts with variations in freezing temperature. The directional solidification of the improperly synthesized or contaminated melt will produce defects in the resulting crystal irrespective of the growth method. In addition to this, the effects of constitutional supercooling stemming from improper synthesis and/or poor mixing during growth are major contributors to growth instability and the formations of inclusions and secondary grain nucleation.

Defects in scintillation materials are critical to their performance. Nearly all components of the scintillation yield are to some extent dependent on the structural quality of the lattice (*38*). Defects of the crystal can be categorized by atomic scale defects such as point defects, and dislocations, as well as macro scale defects such as the aforementioned impurity inclusions, cracks, and polycrystals. For ionic crystals such as the metal halides, anion and cation vacancies must be charge balanced and thus tend to create Frenkel defects (anions and cations in interstitial sites). These types of atomic scale defects serve to trap charge carriers and reduce the scintillation performance and thus must be minimized. Macro scale defects such as grain boundaries and macro cracks serve as light scattering surfaces within the crystal and reduce the efficiency of light collection by the presence of extraneous reflections. Light collection is also extremely sensitive to material transparency whereby impurity inclusions, voids, and surface scratches

cause additional losses to scintillation efficiency. Moreover, any inhomogeneity in the crystal contributes to reduced uniformity of the response due to variations in the locations of radiation interaction.

Considering all the modes of defect formation, the development of synthesis and growth protocols for new materials must be approached as an exercise of minimizing defects through the combined knowledge of their formation mechanisms, material property characterization, and to a large degree, trial and error experimentation to make improvements (*38*). This is to say that despite the several decades of advances in understanding of crystal growth processes, practical crystal growth remains part art form and part science.

Chapter 3: Motivation, Method, and Equipment

3.1 Motivation

$CsCe_2Cl_7$ was first patented in Korea for its potential use in a scintillation based X-ray and gamma-ray detector by inventors Kim, Kang, Park, and Rooh in 2010 and followed by United States and European patent applications filed in 2011 by Yang, Zhuravleva, Melcher, and Szupryczynski (*39, 40*). The scintillation performance characterization and a description of initial crystal growth experiments of single crystals of $CsCe_2Cl_7$ have been published in the Journal of Crystal Growth by Rooh et al (*18*) and Zhuravleva (*41*) and consist of limited growth trials at small diameters using the Czochralski and Bridgman methods of crystal growth respectively. The physical and scintillation properties published in these studies are shown as a comparison with published values for commercially available scintillation materials thallium doped sodium iodide (NaI:Tl) and cerium doped lutetium oxyorthosilicate (LSO:Ce) in Table 1.

Table 2. Comparison of Physical and Scintillation Properties of $CsCe_2Cl_7$, NaI:Tl, and Lu_2SiO_5:Ce

Compound	Melting Temp. (°C)	Structure	Density g/cm3	Z - eff	Scintillation Decay (ns)	Light Output ph/MeV	Energy Resolution at 662 keV (%)	Radio-luminescence Peak max (nm)	Ref.
$CsCe_2Cl_7$	674	Hexagonal	3.6	48	50 (52%) + 210 (48%)	26,000	7.5	385	(*41*)
		Hexagonal			50	28,000	5.5	410	(*18*)
NaI:Tl	651	Cubic	3.67	50	250	45,000	5.6-7.1	415	(*42*)
Lu_2SiO_5:Ce	2047	Monoclinic	7.4	66	40	27,000	7.5-7.9	420	(*42*)

$CsCe_2Cl_7$ has been found to possess good light output of over 25,000 photons per mega-electron volt (ph/ MeV) with an energy resolution as high as 5.5 % (measured as FWHM of Gaussian peak/centroid) for the .662 MeV gamma from a ^{137}Cs source. Additionally, the primary decay time of approximately 50 nanoseconds (ns) for $CsCe_2Cl_7$ provides a faster counting rate than Eu^{2+} activated scintillators (*43*). Judging solely on the reported scintillation performance, $CsCe_2Cl_7$ provides advantages over many scintillators in use in the field.

3.1.1 Prior Growth Efforts

Efforts to grow $CsCe_2Cl_7$ from the melt by Rooh et al (*18*) using the Czochralski method were reported to suffer from polycrystallinity and cracking during growth and cooling, thereby limiting the yield of large single crystals and preventing its further development into detector devices. The authors report a small temperature range in which the crystal would grow and their paper cites scintillation characterization of a 3 x 3 x 1 mm^3 polished piece taken from the grown boule measuring 10 mm long and 10 mm in diameter. Pulling rates of 1-2 mm/ hr and cooling rates of 10°C/ hr were used.

Zhuravleva (*41*) reported single crystals grown from the melt of 30 mm in length and 10 mm in diameter using the Bridgman method to produce small uncracked portions less than 1 cm^3 with scintillation characterization carried out on cut and polished plates of 3 x 3 x 1 mm^3. This paper reports light yield and energy resolution performance could be improved through addressing growth related difficulties to improve crystal quality. Here again, translation rates of 1-2 mm/ hr and a cooling rate of 10°C/ hr were used.

While the research of Rooh et al and Zhuravleva provided enough material to perform scintillation performance characterization, they portray the growth of $CsCe_2Cl_7$ to be problematic citing the poor quality of the crystals or limited yield of uncracked crystals during growth experiments at small diameters. In order to be considered feasible for development into growth at larger diameters suitable for processing and implementation into the field, successful growth of high quality crystals at smaller diameters must be demonstrable.

As a result of this, an improved understanding of growth conditions responsible for the formation of defects such as polycrystals, macro-cracking and inclusions offers the possibility of developing growth processes which improve the crystal quality and yield of uncracked crystals at larger diameters. The aim of this study is to identify growth conditions which improve upon previous efforts through an examination of the entire growth process from initial melting to cooling to room temperature.

3.1.2 Inconsistencies in Reported Structure of $CsCe_2Cl_7$

A literature review of the reported structure for $CsCe_2Cl_7$ produces a few inconsistencies. In the 1980's Meyer performed powder diffraction structure studies on a series of related compositions of the formula $CsRE_2Cl_7$ where (RE=Sm-Lu, Y) yet $CsCe_2Cl_7$ was not investigated directly (*44-46*). Meyer deduced that these compounds will belong to either the $P2_1/c$ monoclinic space group or the Pnma orthorhombic space group. Seifert's review article (*24*) cites Meyer's prior work and assigns the orthorhombic space group $Pna2_1$ to the group of ALn_2Cl_7 compounds with (A=Cs, Rb) and (Ln=La, Ce, Pr, Nd). This contradictory report also conflicts with Seifert's own prior work where the author identified $CsCe_2Cl_7$ as having a hexagonal structure according to (*18*). Moreover, there is no entry in the International Crystal Structure Database (ICSD) for $CsCe_2Cl_7$ and no powder diffraction files exist in any databases available. Due to the absence of reliable reference data, this study aims to produce a definitive structural study of $CsCe_2Cl_7$ through single crystal Laue diffraction pattern analysis which will provide the basis for the determination of anisotropic thermal expansion behavior, a material property critical to growth of bulk single crystals.

The remainder of chapter 3 will detail the methods and equipment used during the investigation of $CsCe_2Cl_7$ crystal growth along with the thermo-physical and structural characterization comprising this thesis work.

3.2 Method Description

3.2.1 Single Crystal Growth of $CsCe_2Cl_7$ Using the Bridgman Method

The focus of the growth experiments in this study are to improve understanding of the growth behavior of $CsCe_2Cl_7$ through an emphasis on determining process variables such as pulling rate, temperature gradient surrounding the growth region, and cooling rates which improve crystal quality. Also of great interest is ampoule design which promotes the growth of a single grain and the interface shape of the growth front throughout growth.

Due to the hygroscopic nature of metal halides, all handling of materials prior to growth were performed in an MBraun nitrogen filled glove-box maintaining an atmosphere less than 0.1 ppm oxygen and moisture to prevent decomposition or hydration. The synthesis procedures of $CsCe_2Cl_7$ consisted of mixing a stoichiometric amount of CsCl and $CeCl_3$ beads of 99.99% purity into quartz ampoules and then evacuating and heating them for several hours until sealed with a hydrogen oxygen torch. The evacuation and heating was performed simultaneously through use of a vertically oriented Lindberg Blue M clamshell furnace coupled to a two stage roughing pump/turbo molecular pump in order to produce high vacuum levels of at least 1×10^{-6} torr while heating the ampoules to approximately 150-200°C for at least 12 hours. Once sealed under vacuum, the ampoules were heated to 850°C for a minimum of 12 hours which is 40°C above the melting point of $CeCl_3$ and 205°C above the melting point of CsCl. After soaking at the synthesis temperature, the melt was cooled to room temperature over several hours thereby producing a polycrystalline ingot of synthesized $CsCe_2Cl_7$. The ingots were then subsequently grown in the same ampoule in which synthesis occurred, or in some growth experiments, the ingot was loaded into a separate ampoule and then melt filtered through a porous quartz frit in order to remove insoluble impurities from the material prior to growth.

For the purposes of confirming proper synthesis, powder X-ray diffraction patterns (PXRD) were produced from synthesized ingots of $CsCe_2Cl_7$ by the use of a Bruker D2 Phaser with an X-ray source operated at 30kV and 10mA using a copper target which produced K-alpha emission lines detected by a 1-dimensional LYNXEYE detector. Powder samples were measured through a protective Kapton amorphous polymer domed sample stage which protects the sample from decomposition in ambient air while adding very little background counts in the detector during measurement.

Two types of resistance heated vertical Bridgman furnaces were used for growth. A 24 zone two inch diameter bore electro dynamic gradient (EDG) furnace from the Mellen Company was operated in Bridgman mode whereby the ampoule was lowered through an established thermal gradient by a 5-phase stepper motor operating a fine pitch lead screw linear sled. The other growth station consisted of a custom built transparent two zone furnace and a DC motor driven traverser from Thoughtventions Unlimited LLC. The latter furnace was designed and built specifically for research on metal halide crystal growth and its development into the growth station used in this work is detailed in section 3.3 Equipment Development.

In order to investigate different ampoule geometries, growth parameters, and material handling protocols, a total of 9 samples were prepared and a list of crystal growth samples is shown in Table 2. For growth experiments taking place in the transparent furnace, repeated growth trials were sometimes performed on

the same prepared sample and photographic documentation of the crack formations were produced prior to remelting and growth. In the interest of this study, a qualitative comparison was made for the cracking behavior for varying annealing treatments after growth and served to draw conclusions to the effectiveness of preventing macroscopic cracks upon cooling. Furthermore, through use the of continuous observation method detailed in section 3.3, the growth interface shape was monitored and its shape evolution during different stages of growth provided insight into the formation of defects as well as stability of the growth front in the presence of impurities in the melt.

Table 3. $CsCe_2Cl_7$ Crystal Growth Samples

Ampoule ID	Melt Filtered	Charge Mass (grams)	Ampoule Diameter (mm)	Growth Station
44	Yes	55	25	24-Zone Mellen
51	No	75	25	Transparent Furnace
66	Yes	40	15	Transparent Furnace
68-1	Yes	40	15	Transparent Furnace
68-2	Yes	40	15	Transparent Furnace
68-3	Yes	40	15	24-Zone Mellen
77	No	37.5	15	24-Zone Mellen
82	No	37.5	15	Transparent Furnace
91	No	37.5	15	Transparent Furnace

3.2.2 Structure Refinement of $CsCe_2Cl_7$

Due to the inconsistencies in the reported structure for $CsCe_2Cl_7$, a definitive structure refinement was necessary not only to provide a clarification for published literature, but to facilitate further investigation of anisotropic thermophysical behaviors relevant to crystal growth, such as the thermal expansion behavior. While structure refinement from X-ray powder diffraction data for cubic crystals is rather straightforward, crystals possessing lower symmetry often require single crystal Laue diffraction data

which provide more reflections from polychromatic radiation thereby improving the overall basis for refinement.

Single crystal Laue diffraction patterns were produced through collaboration with Dr. Bryan Chakoumakos and Dr. Radu Custelcean of Oak Ridge National Laboratory. A crystallite < 0.1 mm^3 was isolated from a boule grown in this study and suspended in paraton oil and held in place within a wire loop attached to a goniometer. While cold nitrogen gas flowed over the crystal, Laue diffraction patterns were captured in transmission mode using a molybdenum target and 2D silicon X-ray detector (Figure 8). A complete dataset was produced by taking Laue patterns across a large section of the Ewald sphere. The intensities of the reflections were then integrated with a trial hexagonal, and later monoclinic space group to produce a list of lattice plane reflections with accompanying Miller indices (hkl) and intensities for further refinement.

The anisotropic coefficients of thermal expansion were determined through collaboration with Professor Waltraud M. Kriven of University of Illinois at Urbana–Champaign. Due to the hygroscopic nature of $CsCe_2Cl_7$, heating of the material in atmosphere would cause subsequent degradation and makes conventional dilatometry measurements extremely difficult to perform. Using the method and software detailed in (*47, 48*), a few milligrams of a powdered mixture of nominally 90% synthesized $CsCe_2Cl_7$ and 10% platinum powder by weight is loaded into 0.3-0.5 mm diameter quartz capillaries and sealed with a torch flame to protect the material from oxygen and moisture during heating. The capillary containing the metal halide/platinum powder mixture is then heated with a thermal image furnace with ability to heat from room temperature to well above the melting point of $CsCe_2Cl_7$. While held at various temperatures, the capillary is placed in the path of X-rays from a synchrotron source at the National Synchrotron Light Source, Brookhaven National Laboratory to produce temperature dependent diffraction patterns. The temperature is monitored through observing the peak shifts from the platinum powder, of which the thermal expansion coefficients are known, thus providing a means of calibrating the temperature during each measurement. The powder diffraction patterns are then analyzed using Rietveld refinement techniques to determine the amount of lattice stretching as a function of temperature. Figure 9 shows the capillaries being loaded and the thermal image furnace used at the synchrotron source.

3.2.3 Scintillation Performance Characterization

In order to assess the quality of the crystals grown in this study, scintillation light output, photopeak energy resolution, radioluminescence, photoluminescence, and optical transmission measurements were performed. Scintillation light output measurements were performed on cut and polished samples approximately 4 x 4 x 1.5 mm^3 from each boule directly coupled to a photomultiplier tube (PMT) and covered with a domed Spectralon reflector. The samples were also covered and coupled to the PMT using mineral oil in order to prevent degradation during the measurement. A Hamamatsu 3177-50 PMT was used for absolute light output measurements while some pulse-height spectra measuring the energy resolution of the 662 keV gamma photon from a Cs-137 source were recorded using a Hamamatsu R6231-100 PMT. Scintillation light yield proportionality was measured as a function of excitation energy using a set of sealed radiation sources with gamma energies ranging from 14 keV to 1274 keV. Transmission and absorption spectra of thin polished plates of 1.5 mm thickness were measured with a Varian Cary 5000 UV-VIS-NIR Spetrophotometer operating in the range of 200-800nm.

Radioluminescence spectra were measured at RT under continuous irradiation from an X-ray generator (35 kV and 0.1 mA). Photoluminescence spectra were obtained with a Horiba Jobin Yvon Fluorolog3 spectrofluorometer equipped with Xe lamp and monochromator.

The crystallization and melting points were determined through differential scanning calorimetry measurements of 35-50 mg samples in alumina crucibles under a flow of argon gas in a Setaram Labsys EVO instrument. Hygroscopicity measurements measuring the moisture absorption over a 60 min time interval at a precisely controlled 40% relative humidity were produced using the from a DVS Intrinsic instrument by Particulate Systems on roughly spherical specimens of approximately 80 mg.

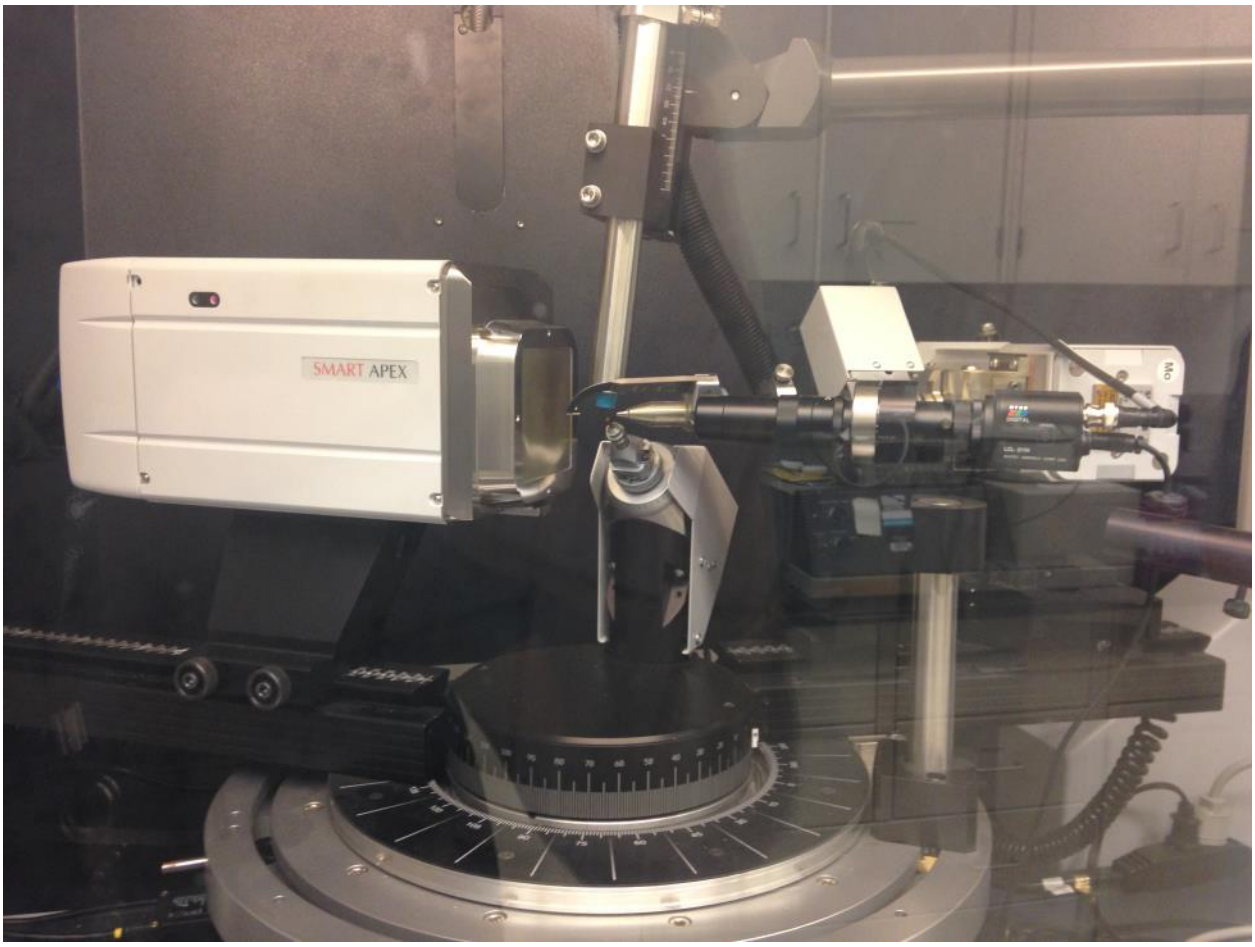

Figure 8. Laue X-ray diffraction apparatus with 2-D detector used in this study.

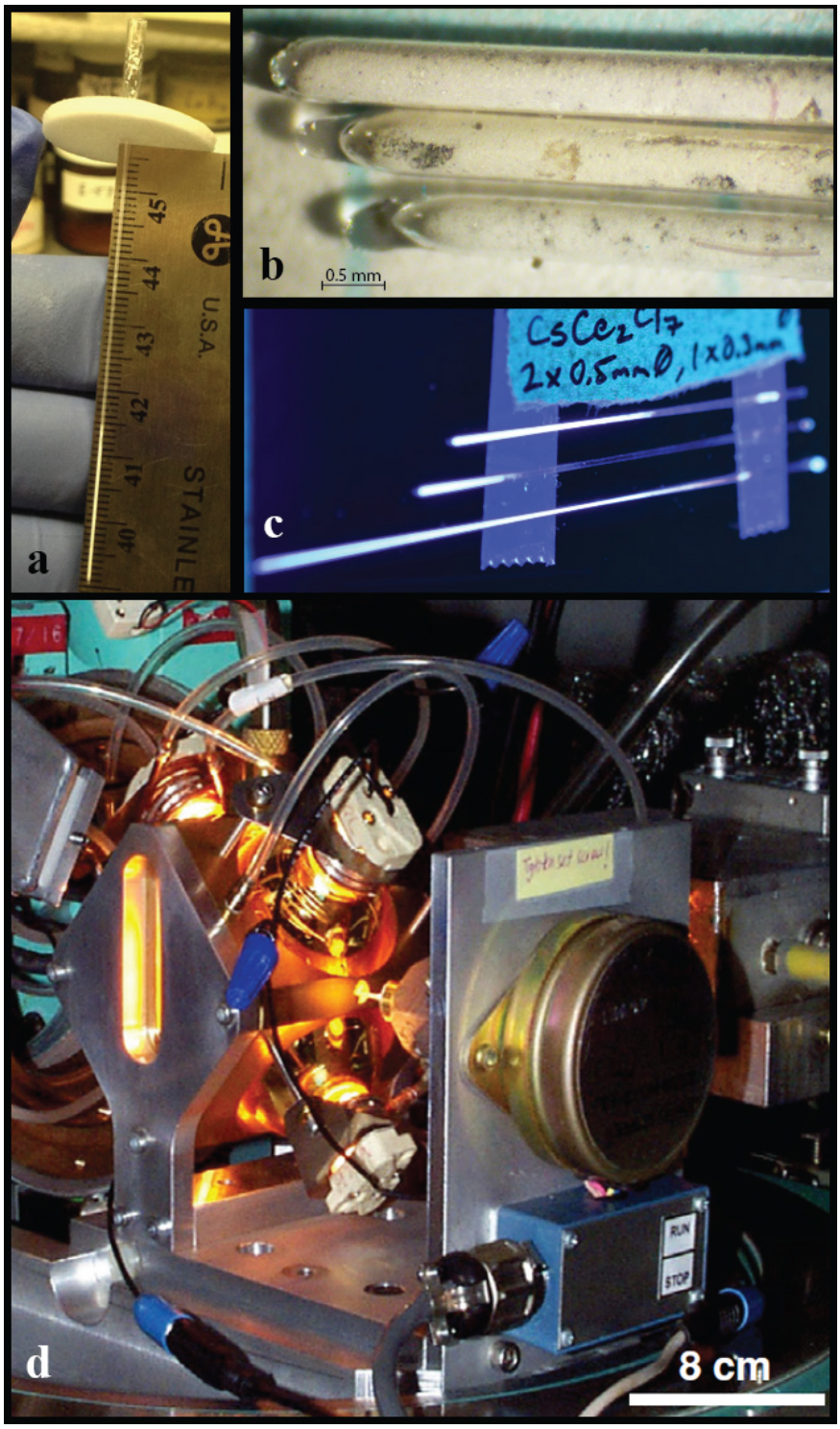

Figure 9. a.) 0.3 mm diameter quartz capillary being loaded in the glovebox, b.) the loaded capillaries under magnification showing the dispersed platinum powder, c.) the capillaries under ultra-violet light, d.) the 4 lamp thermal image furnace used with the synchrotron X-ray source. Image in d.) taken from (*48*).

3.2.4 Thermal Profiling and Numerical Modeling of Growth Stations

Determinations of the thermal profile or measure of the temperature gradients within each furnace are necessary to determine the isothermal region where the growth interface will occur. This allows the crystal grower to predict where the crystallization isotherm exists within the furnace based upon specified zone temperature settings and to plan the translation of the ampoule containing the charge accordingly. 24 and 36 inch long K-type exposed junction temperature probes were used in conjunction with a multichannel data logging instrument to record temperatures with an accuracy of +/- 0.1°C. While this measurement was typically done with the furnace at the operating temperature to be used during the actual growth, an accurate measure of the actual temperature profile with the ampoule and charge in position was often difficult to obtain.

The measured axial temperature profile of the transparent furnace with zone settings of 800°C for the top zone and 500°C for the lower zone were measured to determine achievable thermal gradients and provide a basis for comparisons with numerical models. The results were produced by moving a 1/16 inch diameter K-type thermocouple probe axially through the center of the furnace bore and logging the temperature after achieving thermal equilibrium for each position. The thermocouple's radial position within the bore was held constant by moving it through a long quartz capillary tube fixed to the center of the bore and extending through both ends of the furnace.

The axial thermal profile provides a simple assessment of the locations of critical isotherms such as the melting and freezing points of the crystal to be grown along with an approximation of thermal gradients within the furnace. Oftentimes taking measurements during crystal growth can be problematic due to the presence of probes and vibrations interfering with the growth process. Numerical models of the growth stations were developed in commercially available crystal growth modeling software CGSim from the STR Group. This software uses finite element analysis in 2D space which approximates a three dimensionality through rotational axis-symmetry of the crystal ampoule and furnace geometry. Through a combination of referencing design drawings and manual linear measurements, the furnace geometry was replicated in the software and construction materials specified for each block of geometry. The thermal properties of each material were input into the software described as either constant or as a function of temperature according to available references for furnace insulation, heating elements etc.

By establishing positions of the model control thermocouples identical to the actual furnace geometry, the software was used to simulate the radiative, conductive and convective heat flows in either a steady state or unsteady simulation for target zone temperatures specified for each scenario. In an unsteady simulation, the thermal model of the furnace is produced over several reference frames with either changing heater output, or position of insulation and ampoules, or both. In this manner, contour plots of critical isotherms such as melting point as well as axial and radial thermal gradients could be numerically modeled within the growth stations to diagnose growth conditions suspected of causing defects for particular geometries and procedures. In an effort to understand the effects of additional diaphragms between furnace zones on the thermal gradients surrounding the growth interface, material properties of the growing crystal were approximated within the software based upon available reference data for NaI:Tl, assuming the thermal conductivities, viscosity and heat capacity of the melt and crystal to be similar enough to produce a reasonable model.

3.3 Equipment Development

3.3.1 Transparent Furnace Growth Station

For the purpose of investigating the growth of metal halide crystals, a transparent furnace was commissioned to be built with the dimensions and functionality determined through a collaborative design process with the fabricator. Dr. Stephen Bates of Thoughtventions LLC fabricated the furnace out of a 5 inch diameter quartz cylinder which is coated on the inside with a layer of zinc and gold. This gold coating reflects infrared wavelengths produced by the heaters and above approximately 650°C, the coating becomes fully transparent to visible wavelengths (*49*). This allows an observer to have a clear view of the processes inside the furnace at high temperature without requiring dense insulation. At the maximum temperature of 900°C, the exterior of the quartz cylinder must be gently cooled by three fans to prevent degradation of the gold coating during months of continuous use.

The furnace consists of two discretely controlled resistive heater wires coiled around 3 alumina support rods located inside the gold coated quartz cylinder. The two heaters are controlled through commercially available temperature controllers with ramp/soak programming capability. A custom made traverser unit was also supplied which uses a variable speed DC motor attached to a series of gears to smoothly translate an ampoule suspended from the top of the furnace without vibration at rates between 1-5 mm / hr based upon voltage supplied to the motor.

While no frame or supports were supplied for the lightweight furnace or traverser, the required stands were designed based upon the 8020 series of structural members and fasteners in 3d using computer aided design (CAD) software to produce a sturdy foundation for the growth station to be mounted to. An independent frame was constructed for the ampoule support with vibration dampening feet in order to isolate the growing crystal from the furnace frame and minimize effects from vibrations in the surrounding room. Brackets were fabricated to position the furnace on the frame so that observation could be performed comfortably without compromising the functionality. An illustration of the major components and images of the furnace being constructed is shown in Figure 10.

3.3.2 Continuous Observation Equipment

The major benefit to the transparent furnace is the ability to observe the crystal growth process in order to identify growth conditions which produce defects in the growing crystal. However, due to the slow growth rates and cooling periods, the entire experiment may last several weeks and continuous observation becomes a tedious task. In an effort to observe the melt/crystal interface shapes and contours as well as resolve temporally unique events such as cracking and supercooling throughout growth, a continuous observation method was developed utilizing time lapse macro-photography. Compared with video capturing the entire process which would produce hundreds of hours of footage requiring an unreasonable amount of storage space and a tedious review, time lapse offers the benefit of extremely high resolution images without compromising temporal resolution of transient events or requiring large amounts of data storage capacity. Images can be captured typically every 5-30 minutes in high resolution and then later compiled into high definition videos at 10-30 frames per second using free software ImagesToVideo. In this manner, a several weeks long growth process is condensed into a video merely seconds long facilitating a simple review and investigation of the entire growth process.

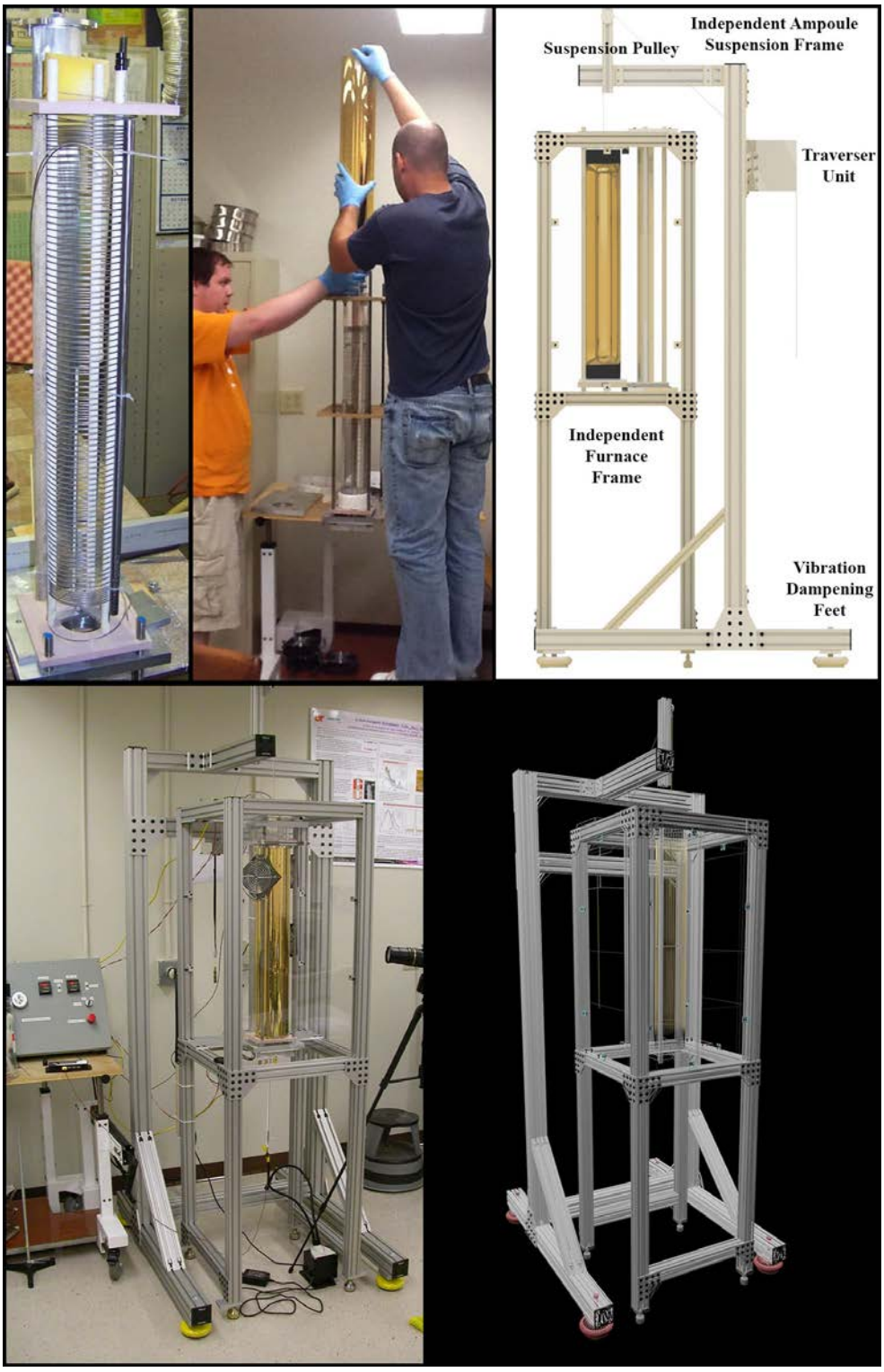

Figure 10. Clockwise from Top Left: Transparent furnace during fabrication. The furnace during assembly in the laboratory. Major components of the growth station. A 3D visualization of the furnace and stand prior to construction. The completed furnace installed in the custom built frame.

The camera consists of a 16.0 megapixel Nikon D5100 digital SLR body with built in intervalometer coupled with a Nikon 40 mm f/2.8g micro Nikkor DX AF-S lens. This combination allows the image of an object very close to the lens to be captured on the image sensor without any magnification or distortion. The result allows the camera to be placed a few inches away from the growing crystal while resolving details of only a few microns in dimension.

Normally, the inside of the furnace is lit only by the red glow of the resistive heating elements, causing many details to be lost due to poor illumination of the subject. To improve the quality of the captured images, a source of illumination was fabricated to deliver a beam of diffuse white light into the furnace, without compromising the functionality of the growth station. This was achieved by coupling a high efficiency, high intensity 15-watt white light emitting diode (LED) to a 70 cm long fused silica rod acting as a light guide. Parabolic reflectors at the LED source located below the furnace focus the light into one end of the light guide and the other end is inserted through a small opening in the lower insulation of the transparent furnace. The light guide was made more efficient through wrapping the cold portions of the fused silica rod with reflective aluminum foil. This allows the crystal to be illuminated with a cold white light at all furnace temperatures without interfering in the growth process. An illustration of the time lapse image recording setup is shown in Figure 11.

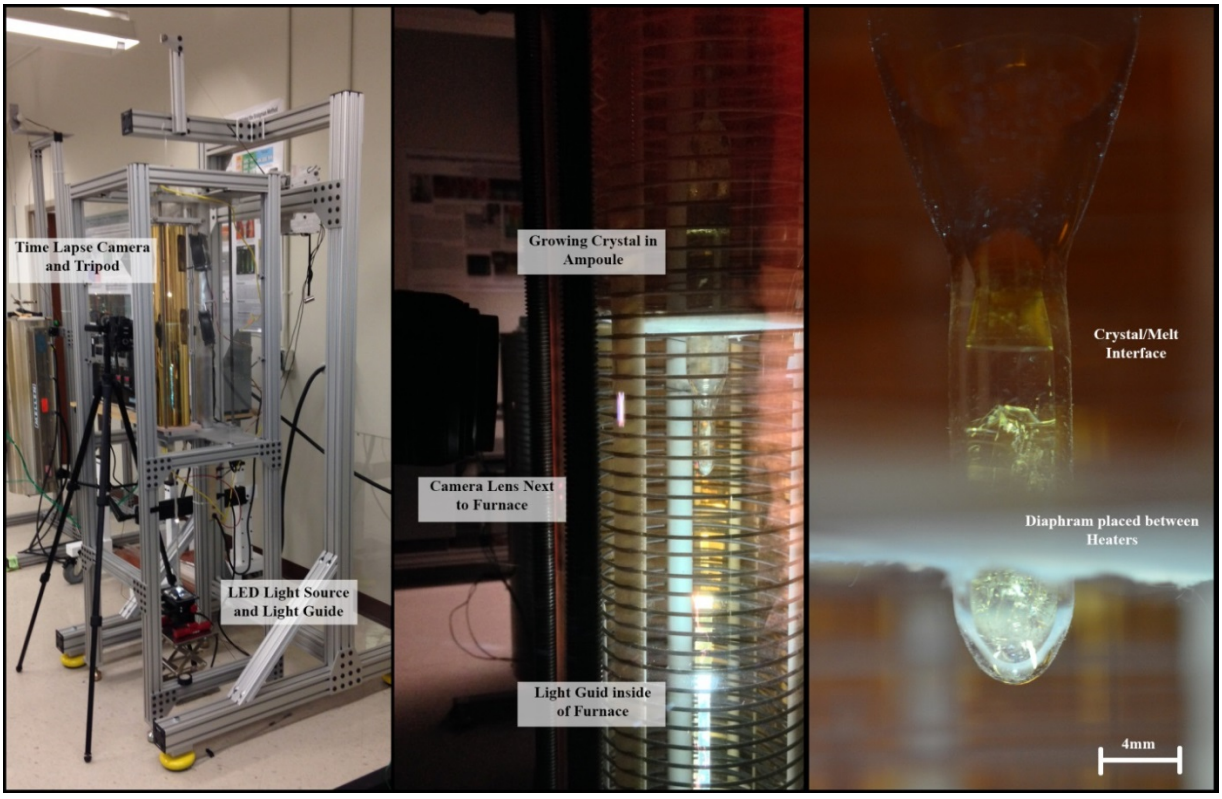

Figure 11. From Left to right. The growth station with time lapse camera, tripod and light source. The lens focusing through the resistive heater winding is placed a few inches from the growing crystal located above the light guide within the furnace. Example image illustrating the details captured with this set-up.

3.3.3 Ampoule Design

For materials exhibiting a large difference between melting and freezing temperatures, the self-seeding process is made difficult by spontaneous homogenous nucleation of numerous crystallites within the supercooled melt. In a paper by Niwa and Masumoto (*50*), a capillary tipped ampoule design is shown to allow a supercooling melt to freeze within the capillary and through competitive growth toward a necked region, isolate a single grain which emerges to grow at the full diameter. The diameter of the capillary is less important than the length which may vary according to the achievable thermal gradients in the furnace. For example, to isolate a grain from a melt that supercools 20°C, the first to freeze region must be shorter in axial length than the thermal gradient in the furnace as well as a corresponding capillary length, which must extend across the range of temperatures between the melting and undercooled freezing point of the material. In other words, for a furnace which produces 10°C/cm axial thermal gradient, the capillary must be at least 2 cm long in order for the material to fully freeze below the necked region shown in Figure 12. For a material exhibiting a characteristic supercooling that is large in comparison with the axial temperature gradient in the furnace, the self-seeding must be assisted with the use of a necked capillary and a large (steep) enough thermal gradient surrounding the capillary.

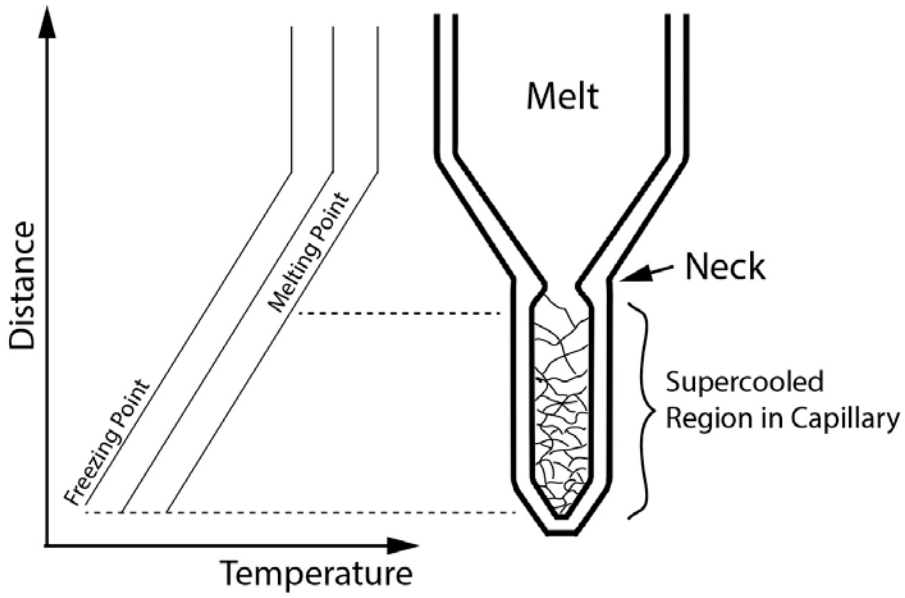

Figure 12. The necked capillary design used for isolating a grain during self-seeding a supercooling material.

To provide a method of filtering out insoluble impurities contained in the melt, growth assemblies incorporating a fritted ampoule that allow the pre-synthesized material to flow through a porous quartz frit located above the growth chamber were used in some experiments. In this manner, insoluble impurities could be filtered out and prevented from reaching the growth chamber in the lowest portion of the ampoule prior to freezing.

3.3.4 Data Logging

In order to monitor and record temperatures in multiple points simultaneously a pair of OMEGA QUADTEMP data loggers were acquired and used with 24 and 36 inch long exposed junction K-type thermocouples with 1/16 inch diameter shafts. In most cases, these units were used to monitor the exterior surface temperatures of the crystal growth ampoule along multiple points to track gradients and determine furnace thermal profiles.

Chapter 4: Results and Discussion

4.1 Structural, Thermodynamic, and Thermo-physical Analysis of $CsCe_2Cl_7$

4.1.1 Synthesis and Phase Identification through Powder X-ray Diffraction

At the beginning of this investigation, there existed no suitable reference pattern in the accessible crystal structure databases and thus a confirmation of proper synthesis of $CsCe_2Cl_7$ was made difficult. As a result, the verification of proper synthesis of a single phase in small sample sizes was initially performed through a comparison of the measured powder X-ray diffraction (PXRD) pattern with the published PXRD pattern of a related compound, $CsPr_2Cl_7$, thought to be isostructural with $CsCe_2Cl_7$ but with slightly smaller lattice parameters belonging to the $Pna2_1$ orthorhombic space group according to Seifert (*24*). The fit to the $CsPr_2Cl_7$ pattern seen in Figure 13 produced a reasonable comparison for verifying the existence of a single phase as most peaks were in good agreement with the pattern yet some peaks in the measured data were not represented. This suggested that either the synthesis procedure was incomplete, with additional phase(s) present in the measured data, or the pattern was not an adequate analog for comparison with the unknown structure of $CsCe_2Cl_7$. With regards to multiple phases caused by incomplete or improper synthesis, diffraction peaks from the CsCl and/or $CeCl_3$ constituents or another compound containing them would need to be identified within the measured data to confirm the assumption. A mixture of multiple phases could be attributed to the orphan peaks missing in the available $CsPr_2Cl_7$ pattern yet no matches to the readily available PXRD pattern for the components or related compounds could be fitted to the measured data.

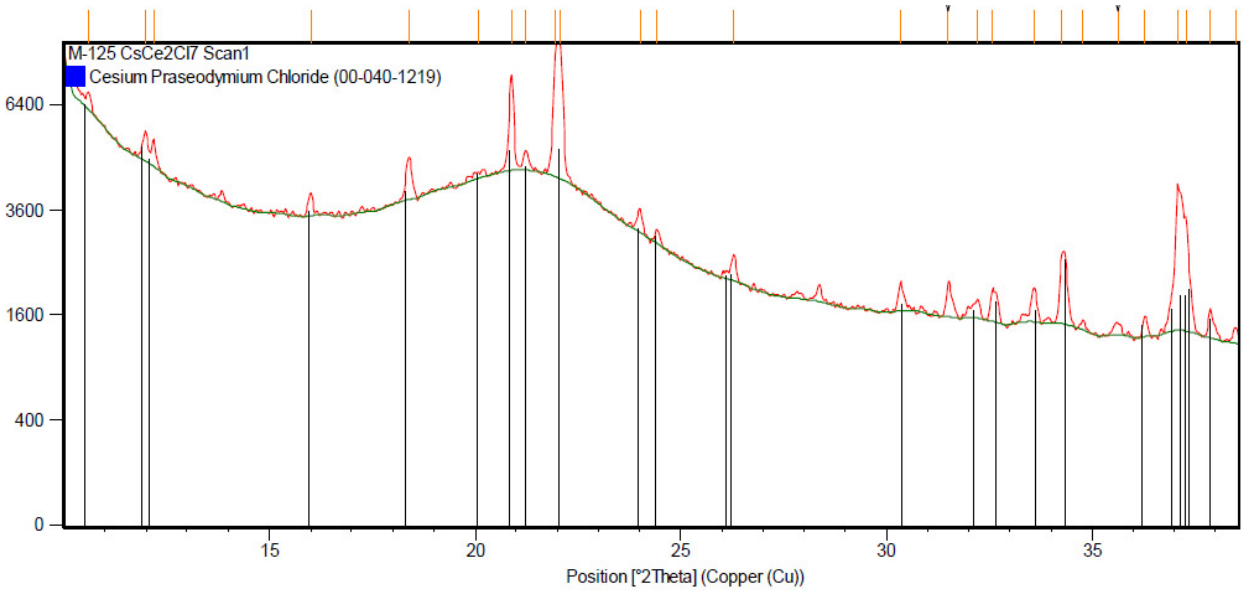

Figure 13. Comparison of measured PXRD data from $CsCe_2Cl_7$ with the available pattern from $CsPr_2Cl_7$ showing a reasonable fit, but with a few unmatched peaks, suggesting they are not isostructural.

Furthermore, the creation of a calculated pattern from the published $CsPr_2Cl_7$ structure using the published lattice parameters in (*24*) did not improve the fit nor account for extra peaks in the measured data.

In consideration of the latter case, without a refined structure for $CsCe_2Cl_7$ any comparison with the pattern of the Pr compound is based upon the assumption it is isostructural, and provides merely a qualitative comparison at best. In either case, synthesis was carried out in a similar fashion for other compounds for which a structure pattern could be used to verify the existence of a single phase. The next section provides results from an effort to resolve the structure of $CsCe_2Cl_7$.

4.1.2 Structure Refinement from Laue Diffraction Data

The Laue diffraction data of a small crystallite fragment taken from a grown crystal of $CsCe_2Cl_7$ was acquired in the lab of Dr. Radu Custelcean and later refined by Dr. Bryan Chakoumakos at Oak Ridge National Laboratory (ORNL). The initial results indicated a hexagonal symmetry but further refinement produced an agreement value R1=6.9% fitting a monoclinic structure belonging to the $P2_1/b$ space group using the SIR-2011 program within the WinGX structure analysis package in addition to SHELXL-2013. This space group is known to mimic the hexagonal space group $P6_3$ through twinning when the unique angle is nearly 120°. Table 3 contains the new refined data from this study. Figure 14 contains an illustration of the ball and stick atomic model for the unit cell based upon an electron density map generated from the refinements. With 16 formula units, $CsCe_2Cl_7$ possesses a larger unit cell than previously reported with lower symmetry compared with the purported hexagonal and orthorhombic structure. The atomic model depicts cerium as black, cesium as red, and chlorine as blue.

The refined data was organized into a crystallographic information file (*.cif) that is a commonly used format in crystal structure databases. The cif file can then be used to create simulated diffraction patterns from various sources (Figure 15). The cif file was also used to simulate the powder data acquired from the Bruker D2 phaser's Cu-Kα X-ray source and a comparison with PXRD produces an excellent fit confirming proper synthesis techniques (Figure 16).

Table 4. Refined Structure of $CsCe_2Cl_7$

Crystal Structure	Monoclinic
Space Group	$P2_1/b$
Formula Units Per Cell	16
a (Å)	19.365(1)
b (Å)	19.385(9)
c (Å)	14.876(1)
Gamma Angle (°)	119.83(4)
Volume of Unit Cell ($Å^3$)	4844.506

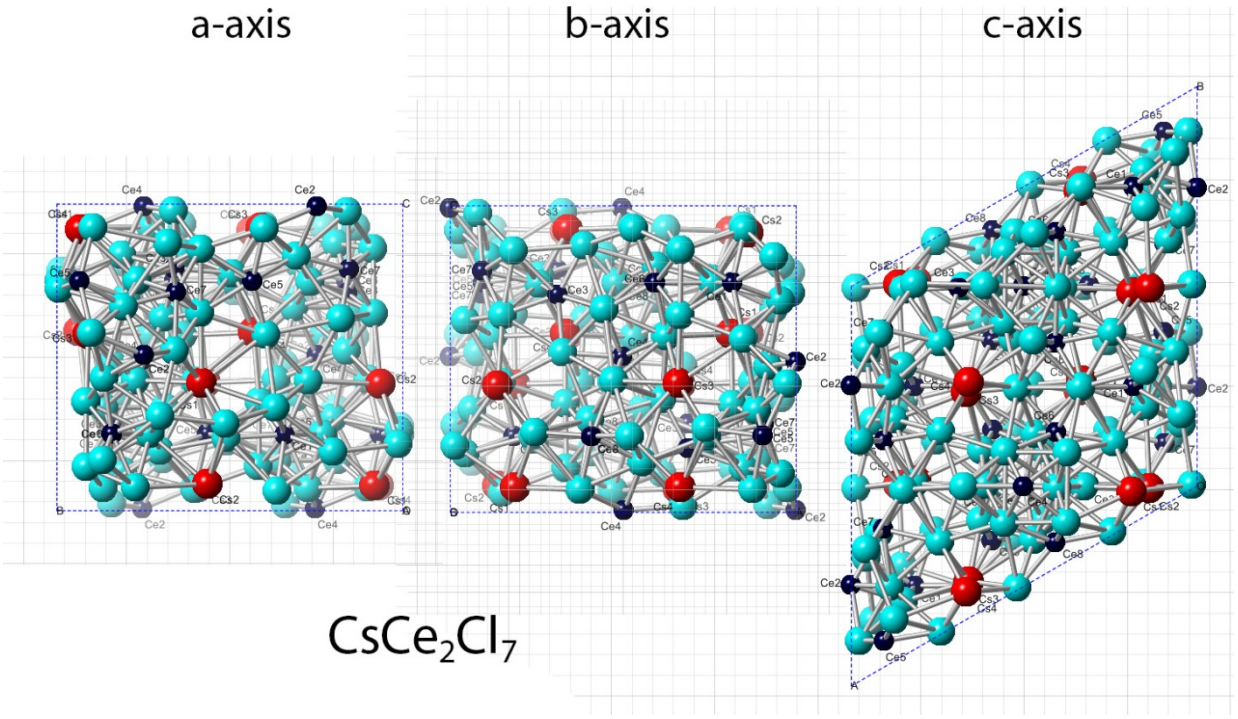

Figure 14. Atomic model of the refined $CsCe_2Cl_7$ structure as viewed along the crystal axes.

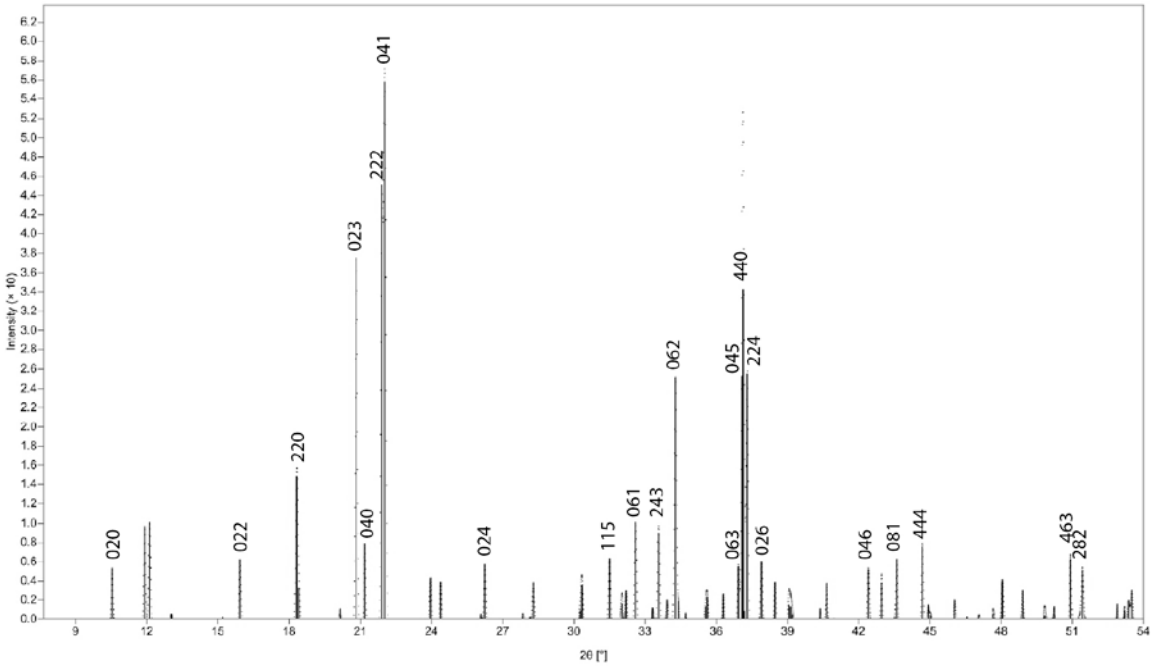

Figure 15. The calculated powder pattern for $CsCe_2Cl_7$ with labeled hkls for angle dispersive X-rays from Cu-Kα radiation based upon the single crystal Laue data.

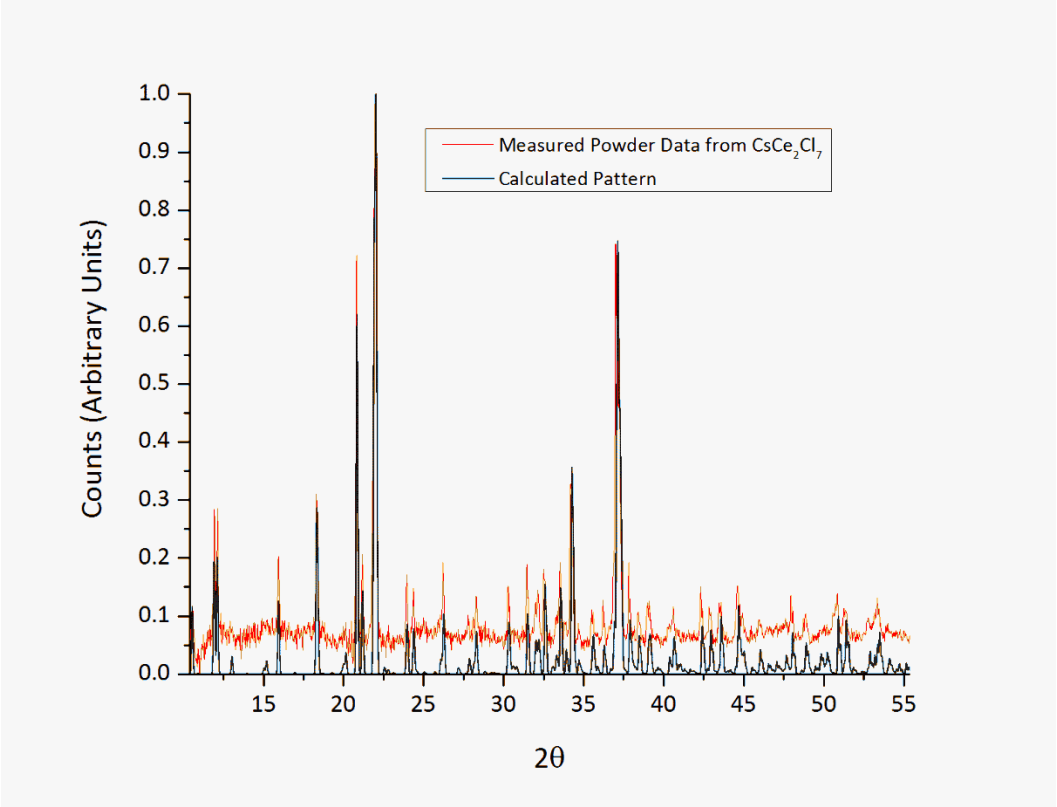

Figure 16. Measured PXRD data from $CsCe_2Cl_7$ (red) with background subtracted compared with the calculated pattern from the refined structure (black).

4.1.3 Differential Scanning Calorimetry

The results from measurements of the melting point and crystallization point isotherms using differential scanning calorimetry (DSC) on the Labsys EVO instrument are shown in Figure 17. The crystallization point is approximately 58°C below the melting point of 672°C. Some variance in the crystallization point is observed and results shown are typical. The large degree of supercooling can be attributed the complex structure of $CsCe_2Cl_7$ which requires a large degree of ordering in the melt prior to the phase transition representing a free energy barrier preventing the melt from freezing closer to the melting point.

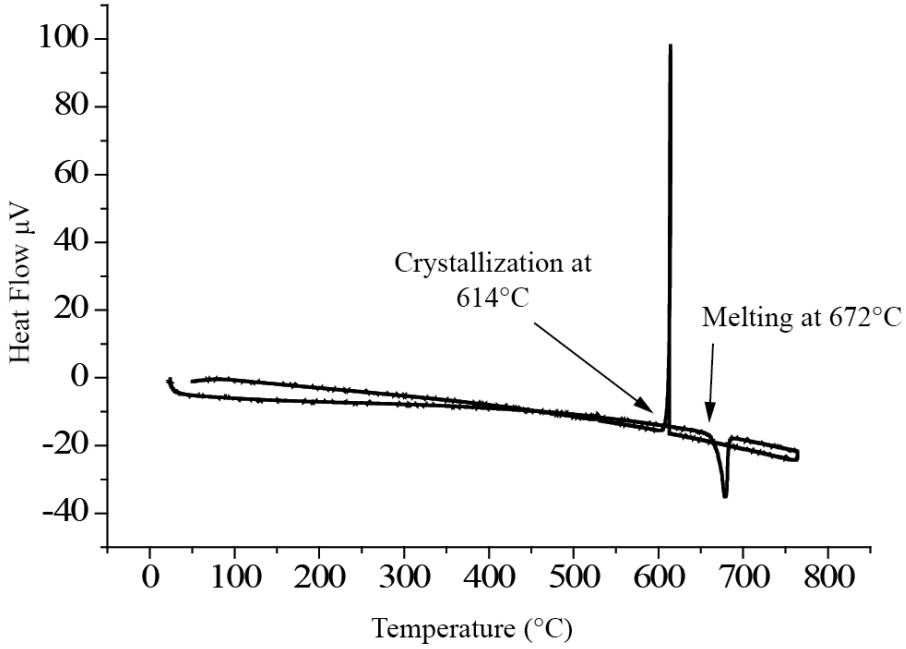

Figure 17. The differential scanning calorimetry measurement of $CsCe_2Cl_7$. This material exhibits a characteristic supercooling of approximately 58°C.

4.1.4 Hygroscopicity

The plot of the moisture uptake given by percent mass change over time at 40% relative humidity is depicted for $CsCe_2Cl_7$ along with other metal halide scintillators in Figure 18. The results indicate $CsCe_2Cl_7$ has the lowest hygroscopicity of all compositions tested which is advantageous to canning procedures required for prevention of decomposition.

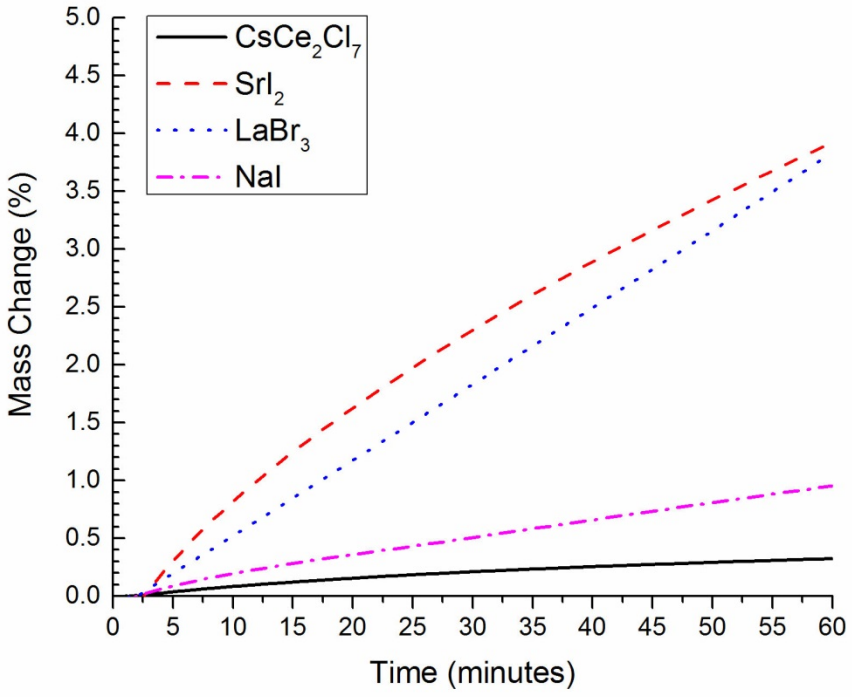

Figure 18. The hygroscopicity curves for $CsCe_2Cl_7$ in comparison with SrI_2, $LaBr_3$, and NaI.

4.1.5 Coefficients of Thermal Expansion through Temperature Dependent PXRD

The results from the temperature dependent PXRD using synchrotron X-rays at the National Synchrotron Light Source at Brookhaven National Laboratory are shown in Figure 19. The structure of $CsCe_2Cl_7$ was not observed to undergo any phase transformations upon heating and the same structure is present after cooling back to room temperature. Provided with the .cif file produced from the structure refinement of the Laue data, a least squares fit of the temperature dependent PXRD data yielded the anisotropic coefficients of thermal expansion and a comparison with those of commercially produced NaI, SrI_2 and $LaCl_3$ are provided in Table 4. (*7, 51, 52*). The comparison shows that $CsCe_2Cl_7$ possesses a modest thermal expansion for each crystal axis with $\alpha_a = 2.13 \times 10^{-5}$ (K^{-1}), $\alpha_b = 2.67 \times 10^{-5}$ (K^{-1}), and $\alpha_c = 2.71 \times 10^{-5}$ (K^{-1}) compared with $\alpha_a = 4.74 \times 10^{-5}$ (K^{-1}) for NaI as an example. The dimensionless anisotropy of thermal expansion given as α_a/α_b or α_a/α_c is least for $CsCe_2Cl_7$ with ratios of approximately 0.8 in comparison with $LaCl_3$ and SrI_2 with values of 2.2 and 1.7 respectively for α_a/α_c. This finding suggests that the low thermal expansion anisotropy of $CsCe_2Cl_7$ produces a lesser sensitivity to crystal orientation under thermal induced strains as compared with materials possessing a highly anisotropic thermal expansion behavior. The temperature dependence of the unique angle (gamma) is shown in Figure 20.

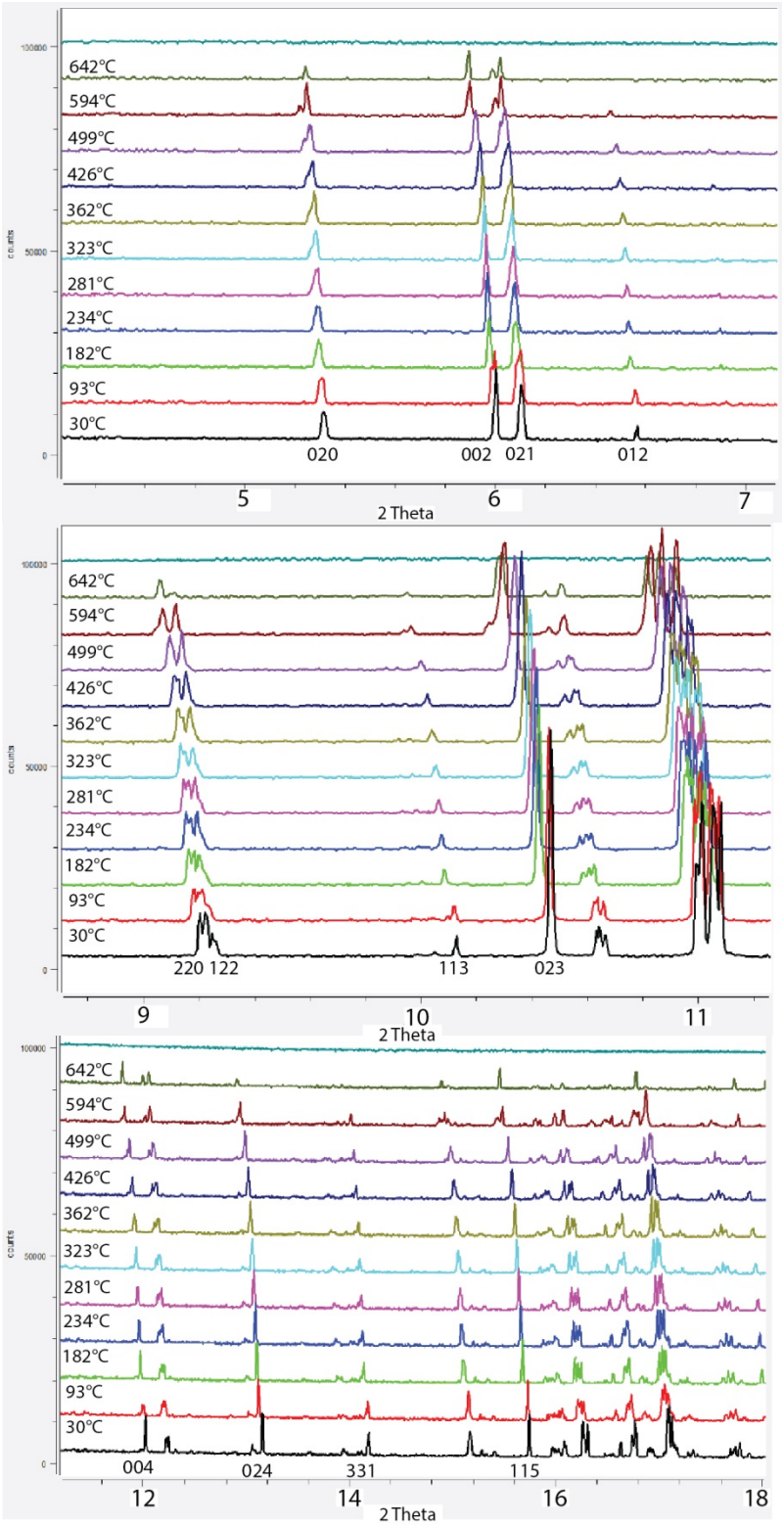

Figure 19. Temperature dependent diffraction of $CsCe_2Cl_7$. Specific major peaks are identified by miller index below each plot.

Table 5. Anisotropic Coeffiecients of Thermal Expansion of $CsCe_2Cl_7$ and other Metal Halide Scintillators

Material (lattice type)	Crystal Axis	Coefficient of Thermal Expansion α (K^{-1} x 10^{-5})	Anisotropy Ratio α_a/α_b	Anisotropy Ratio α_a/α_c
$CsCe_2Cl_7$ (monoclinic)	a	2.13	0.798	0.786
	b	2.67		
	c	2.71		
NaI (Cubic)	a	4.74	-	-
SrI_2 (Orthorhombic)	a	1.55	0.718	1.685
	b	2.16		
	c	0.92		
$LaCl_3$ (hexagonal)	a	2.40	-	2.182
	c	1.10		

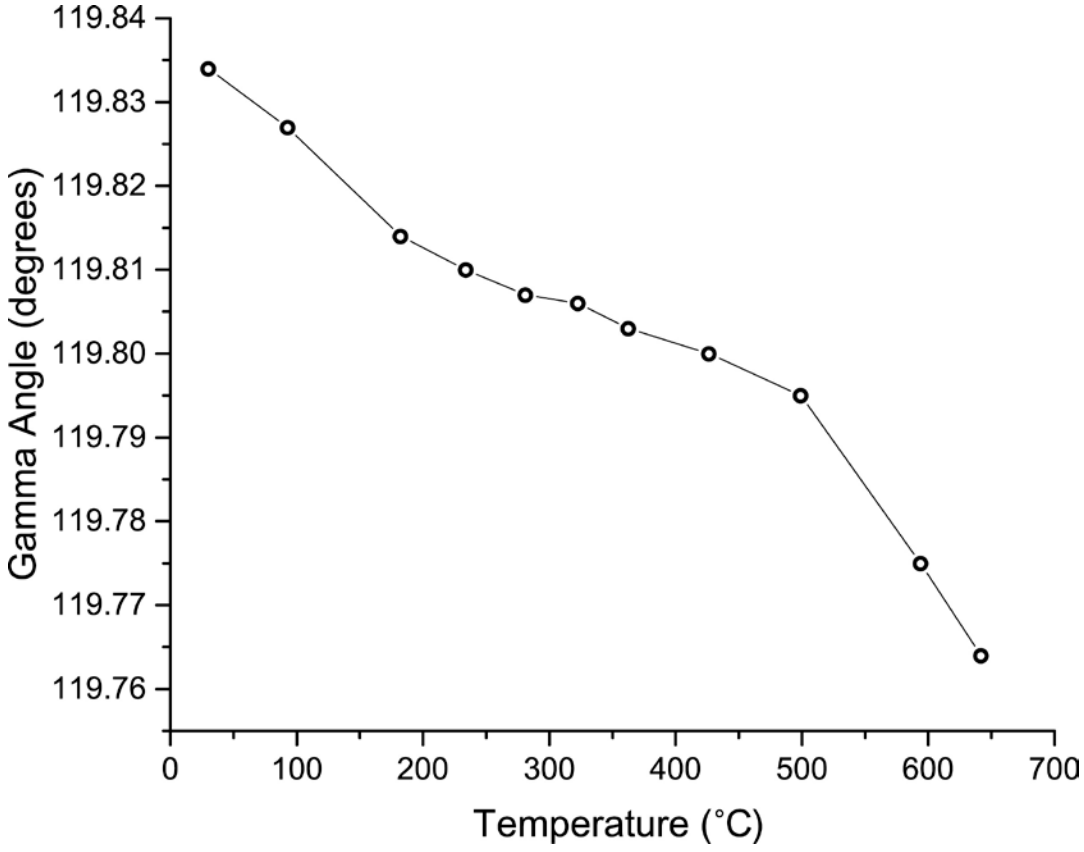

Figure 20. Unique angle temperature dependence for the monoclinic unit cell of $CsCe_2Cl_7$.

4.2 Thermal Profiling and Numerical Modelling of the Transparent Furnace

The growth experiments performed in the custom made transparent furnace offered a challenge in determining the unique thermal behavior and optimizing the conditions necessary for crystal growth of $CsCe_2Cl_7$. Since the furnace design contains no bulky insulation, the primary means of heat transfer are radiative and convective. In the absence of a charge in the bore, the measured axial temperature profile is based on air temperatures produced through natural convection from the close proximity to the heating elements. Thus a probe measuring the air of the furnace would underestimate the temperature. An object placed in the furnace is susceptible to the radiative heat that is reflected by the gold coating and the surface emissivity then dominates the measured temperature on the surface. This results in differences of 20-50°C between measured temperature on the surface of a growth ampoule and the surrounding ambient temperature. Moreover, in order to determine the precise temperature a growing crystal is subjected to, a placement of a thermocouple probe in intimate contact with the quartz ampoule surface or an analog of a similar material is required.

The measured geometries and axial thermal profile of the transparent furnace was used as the basis for a numerical model created in CGSim to aid in assessing the thermal environment under varying conditions. The measured data served as the basis for tuning the furnace material descriptions and modeled thermal behavior to achieve a reproduction of the measured data with an accuracy of +/- 15°C within a geometrical model with distance tolerances of +/- 0.5 mm to the actual furnace. The location of the reference temperature for each heater zone was initially established to correlate to the position of control thermocouples on the actual furnace to within 1 mm in the axial and radial dimensions of the axis-symmetric model. While this provided a good first approximation, a more accurate model was attained through subsequent adjustments to emissivity and reflectivity values for the heating elements and reflective coating of the interior of the furnace respectively. Several revisions to these values were necessary to improve model accuracy and are not presented in this study. Additional improvements were made when the air within the furnace was given accurate temperature dependent density and heat capacity based upon data available from the National Institute of Standards and Technology (*53*). An important aspect of the numerical model is that it does not supplant observations but serves to enhance the understanding of the characteristic thermal behavior of a growth experiment and to interpolate temperature values where measurements are very difficult to produce, such as within the sealed growth ampoule or gradient conditions during growth when the ampoule must not be disturbed.

The measured axial temperature profile of the transparent furnace under zone settings of 800°C for the top zone and 500°C for the lower zone is shown in Figure 21 along with a simulated profile produced with CGSim. The results indicate that the transparent furnace produces temperatures at the center of the bore approximately 25-30°C below the zone set point and must be factored when designing a growth experiment. The axial thermal gradient which is critical to the vertical Bridgman growth method from both the measured and simulated profile did not exceed 13°C/cm under the maximum difference in zone temperatures without modifications. Due to the supercooling behavior of $CsCe_2Cl_7$, a gradient larger than 13°C/cm would be required for controlled self-seeding and thus a diaphragm placed between the heaters was determined necessary to shield the radiation of one heater from the other effectively increasing the achievable thermal gradient.

Different concepts of a diaphragm were numerically modeled to investigate their effectiveness. First a 10 mm thick nickel metal diaphragm was chosen as its large thermal conductivity and high melting point could act as a susceptor to the heat radiating from the furnace walls. The result is seen in Figure 22. The gradient is increased to nearly 40°C/cm with this arrangement. Although this concept approached a more ideal thermal profile, implementing its structure within the furnace was deemed unnecessarily difficult and thus an easier implemented material was chosen in the second concept modeled. Figure 23 features the results of modeling a 3 mm thick Kaowool diaphragm placed between the heaters which produced a larger 60°C/cm gradient within the region of the insert and thus would provide the basis for the design and implementation of an experimental diaphragm.

The Kaowool diaphragm is comprised of alumina and silica fibers with a few percent organic binder which produces a durable flexible consistency before firing and allows a somewhat simple handling procedure to fabricate an insert which matches the outer diameter of the growth ampoule, providing a close fit and effective control of the thermal gradient in the immediate region.

The result of profiling the gradient imposed by the experimental furnace diaphragm is shown in Figure 24. Multipoint axial thermal profiling produced an approximately 75°C/cm axial gradient 1 cm above the diaphragm and a 10°C/cm axial gradient 1 cm below the diaphragm. This agrees well with the numerical model and represents an ideal initial zone setting for growth experiments of $CsCe_2Cl_7$ as the melting point isotherm is located very close to the diaphragm, thereby able to contribute to the stability of the isotherm and influence the shape of the growth interface.

4.3 Crystal Growth of $CsCe_2Cl_7$ and Observations

4.3.1 First Attempt at Growth

E-44 was grown using the fritted ampoule concept whereby the charge is first synthesized in a separate ampoule and then loaded into the growth ampoule assembly. The assembly features a chamber with a fritted ampoule nesting inside an outer ampoule with a conical tipped geometry. Once the synthesized charge is loaded into the upper fritted ampoule and brought to a molten state, it flows through the porous quartz frit and into the growth chamber below. This process produced very clean material with no black residue thought to be carbon impurities.

The resultant 22 mm diameter boule was grown in the 24-zone Mellen furnace with an approximately 15-20°C/cm axial gradient. The pulling rate was 1 mm/hr and after growth, the boule was cooled to room temperature at 4°C/hr. The resultant boule appeared to have a very large defect density which made it poorly translucent with bands of inclusions scattered throughout the bulk likely caused by constitutional supercooling. The center of the boule contained an intersection of multiple grains indicating secondary nucleation during growth and subsequent cracking along the grain boundary. An image of the boule and a polished section illuminated with transmitted light is seen in Figure 25.

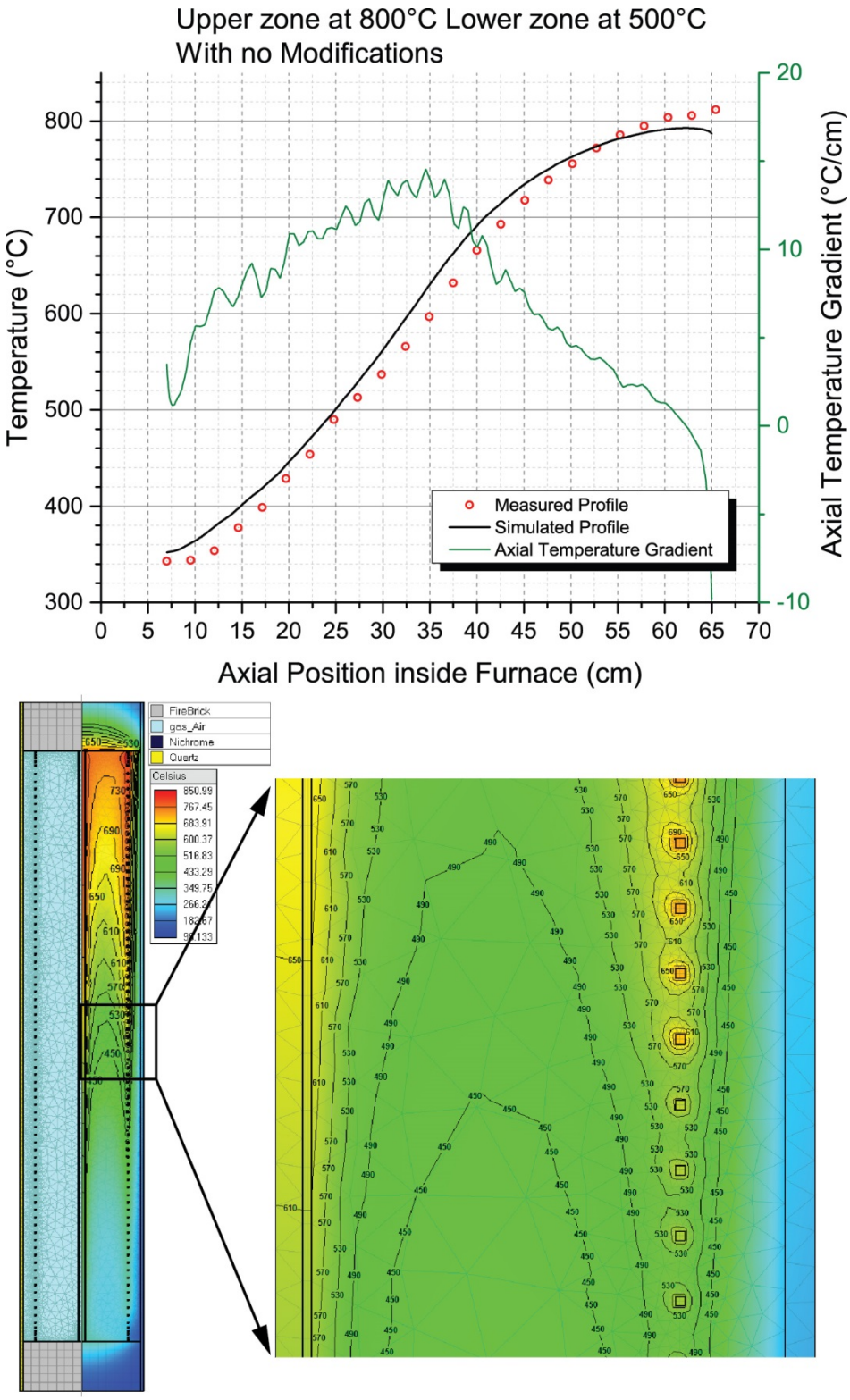

Figure 21. Comparison of measured temperature profile data with numerical model of the transparent furnace.

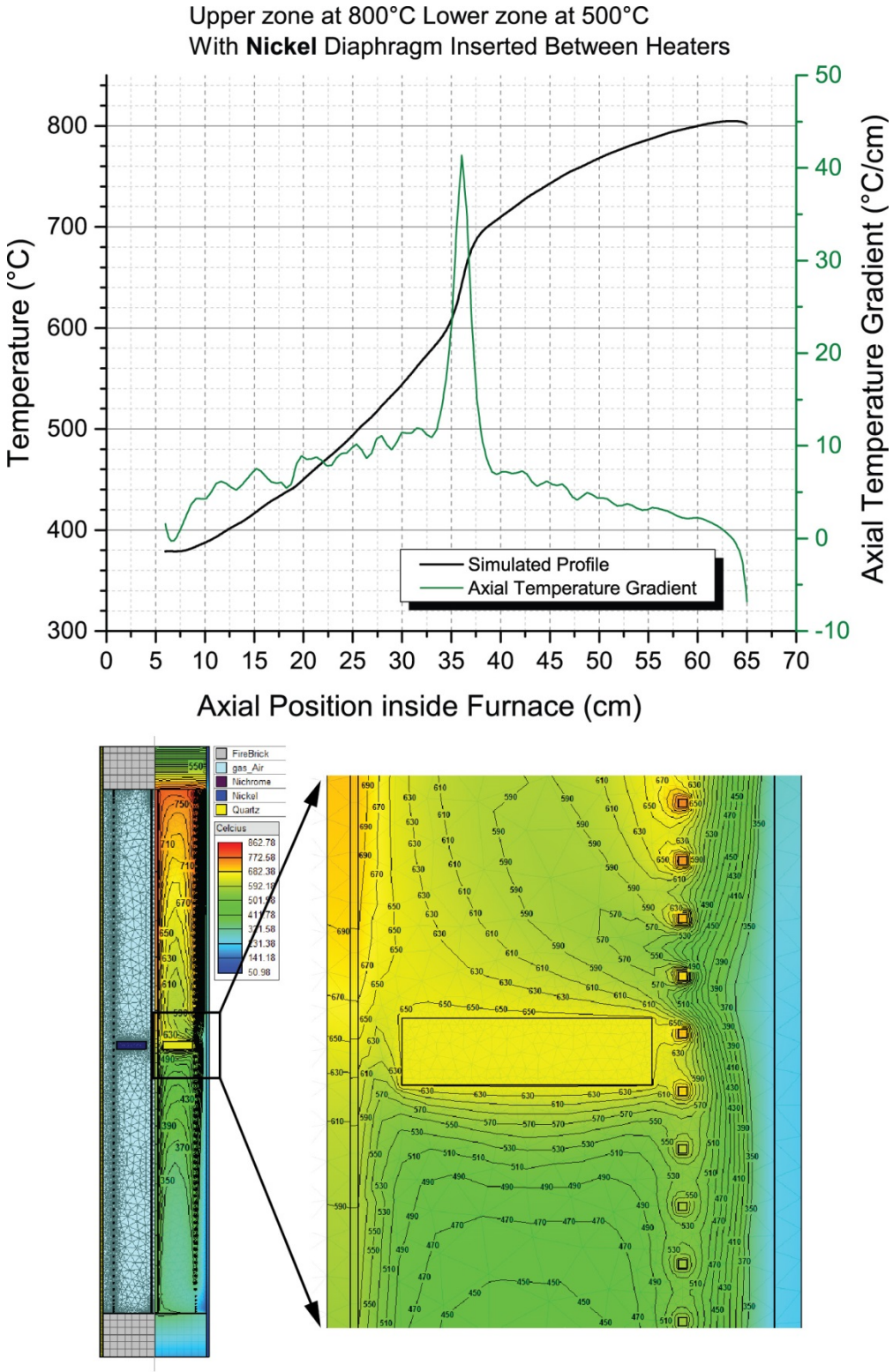

Figure 22. Numerical model of transparent furnace with 10 mm thick nickel metal diaphram used to augment the temperature gradient between the heater zones.

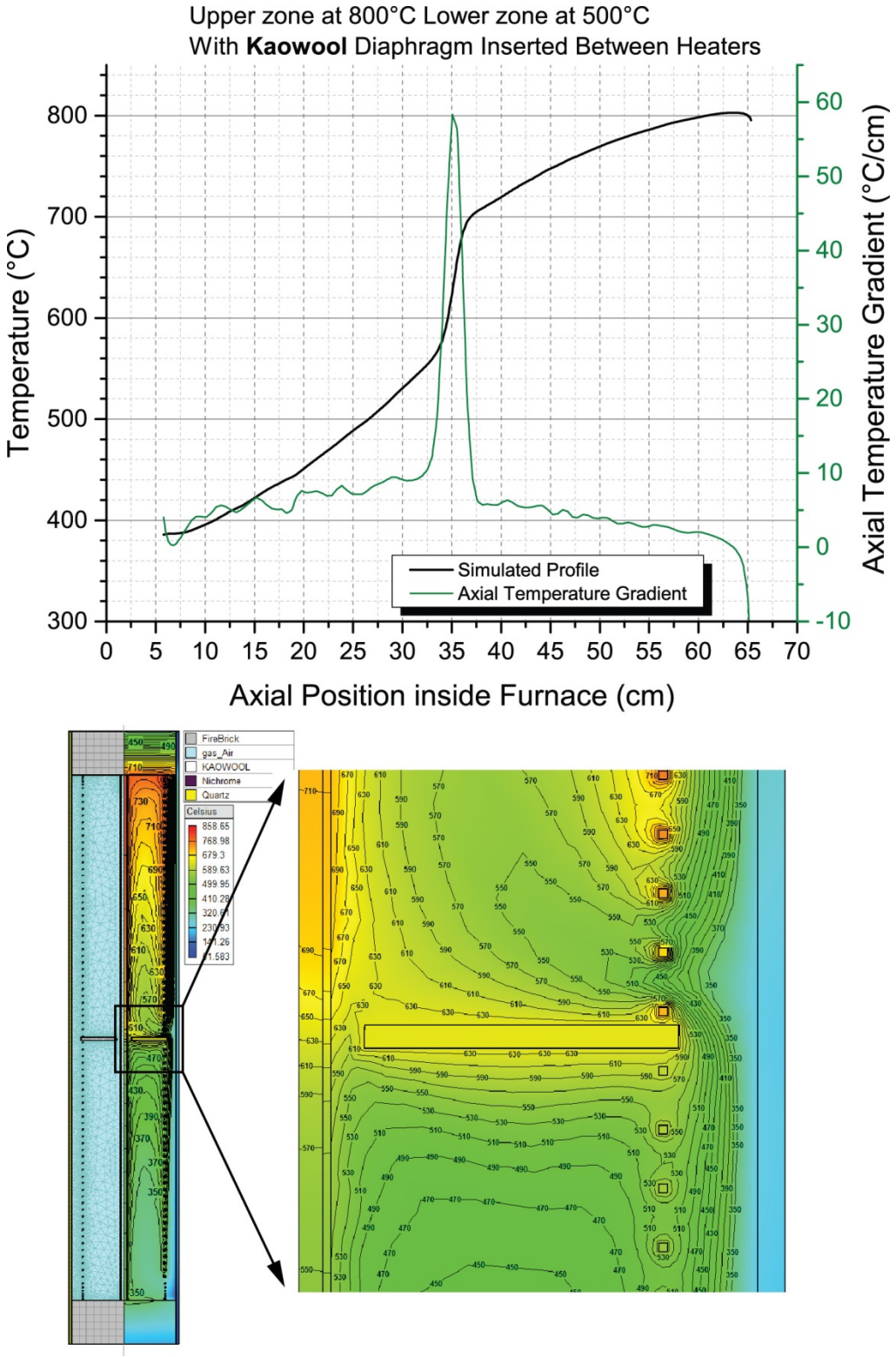

Figure 23. Numerical model of the transparent furnace with 3 mm thick Kaowool diaphragm eventually implemented in the furnace.

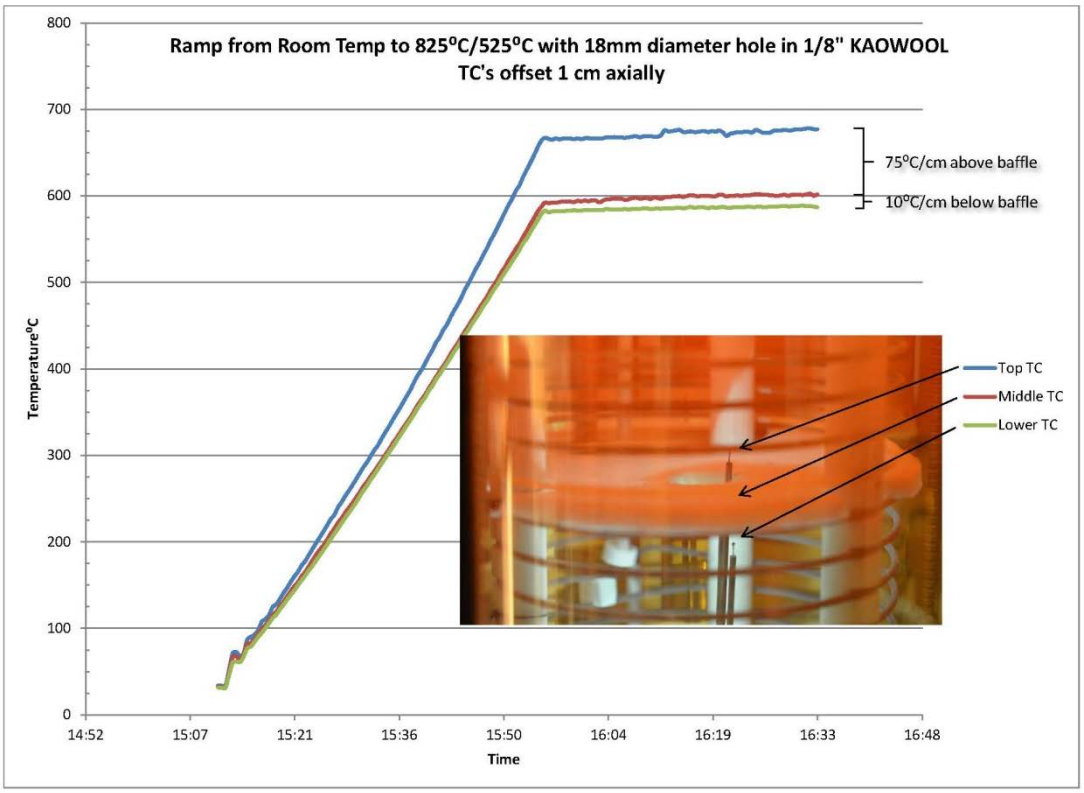

Figure 24. Multipoint axial thermal profile capturing the enhanced temperature gradient created by insertion of the diaphragm between the heaters.

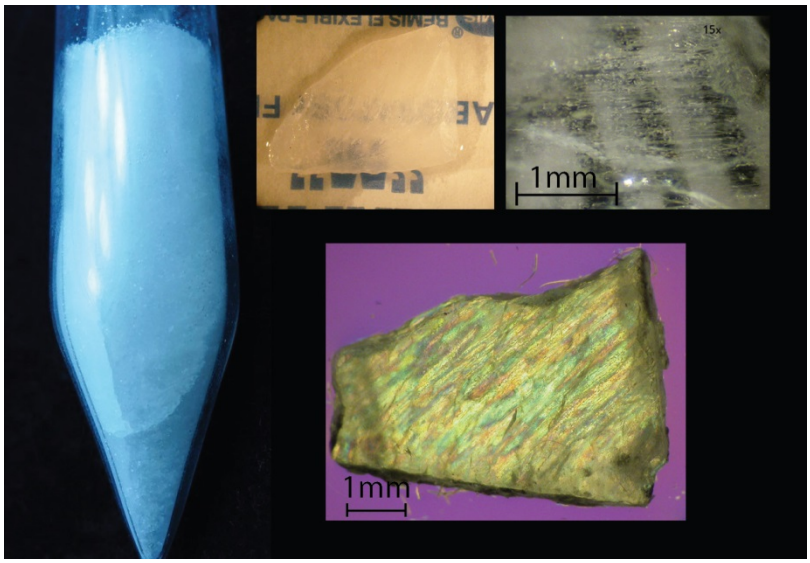

Figure 25. Clockwise from left: The boule of E-44 in ampoule after growth. A 3 mm thick polished piece with poor translucency. A 1 mm thick polished piece with visible inclusions under magnification. The same piece with transmitted polarized light to reveal strain fields along inclusion bands.

A thinly polished sample 1 mm in thickness viewed with transmitted polarized light reveals strain fields running parallel to bands of inclusions throughout the crystal, indicating residual stresses from the cooling process surrounding the inclusions. Subsequent observations of several growth experiments using the transparent furnace would facilitate a deeper understanding of the factors affecting crystal quality.

4.3.2 Growth within the Transparent Furnace

E-51 was prepared from a batch of synthesized material that was set aside from an earlier growth attempt and was unfiltered prior to growth. The charge was approximately 75 grams loaded into a 22 mm diameter ampoule with conical tip geometry. This first crystal grown in the transparent furnace offered several insights during the multiple growth experiments with various pulling rates. The most noticeable issue was the supercooling phenomenon during initial freezing at the bottom of the taper tip geometry. Supercooling was seen to cause a 1-2cm portion of the lowermost melt to rapidly solidify creating several crystallites competing for growth and thus a polycrystalline grain structure at full diameter. This occurred without failure at both 5 mm and 2.5 mm/hr pulling rates.

The melt in E-51 appeared slightly yellow with a crust of black carbon impurities floating on top. The zone settings of 775°C in the top zone and 550°C in the lower zone created a solid liquid interface (SLI) near the axial center of the furnace and a temperature probe on the ampoule surface indicated the SLI was at approximately 674°C, in agreement with the reported melting point. Although the SLI could be clearly seen, the macroscopic shape of the interface was seen to be concave toward the melt with a discontinuous jagged profile indicative of a polycrystal growth front. This suggests the interface shape could be made more flat with a decreased tendency to nucleate secondary grains if a larger thermal gradient were used in conjunction with a means to isolate a single grain at the start of growth.

Due to the lack of insulation in the transparent furnace, the melting point isotherm was observed to travel with the ampoule during translation which produced a growth rate approximately 50% slower than the actual pulling rate. This differential in growth and pulling rate was seen to be reduced by slowing the pulling rate but appeared to only have a marginal effect. This indicates that the combined thermal mass of the ampoule and crystal strongly influenced the surrounding gradient by causing the freezing point isotherm to migrate lower into the cool zone where the thermal gradient is decreased. In this instance, the growth process took place under changing thermal conditions resulting in instabilities of the growth front later in growth.

Attempts at cooling the boule to room temperature after growth at 20°C/hr produced severe cracking while subsequent regrowth and cooling at 4°C/hr still produced moderate cracking but with an improvement to the size of uncracked regions. An illustration of the concave SLI during growth at 2.5 mm/hr and the resultant boule after cooling to room temperature at 4°C/hr is seen in Figure 26. A section of the boule exhibiting the best quality grains was removed and a portion polished to investigate the clarity is also shown. The isolated section reveals a crystal of improved clarity over E-44 with sub millimeter sized inclusions scattered throughout the bulk.

The result of this growth experiment provided the motivation to address issues with supercooling during initial freezing which produced a polycrystalline boule, and the concavity and instability of the growth front stemming from an inadequate control over the thermal gradient during growth. In addition to addressing these issues, the following growth experiments would explore the cracking behavior with the implementation of continual observations with time lapse photography.

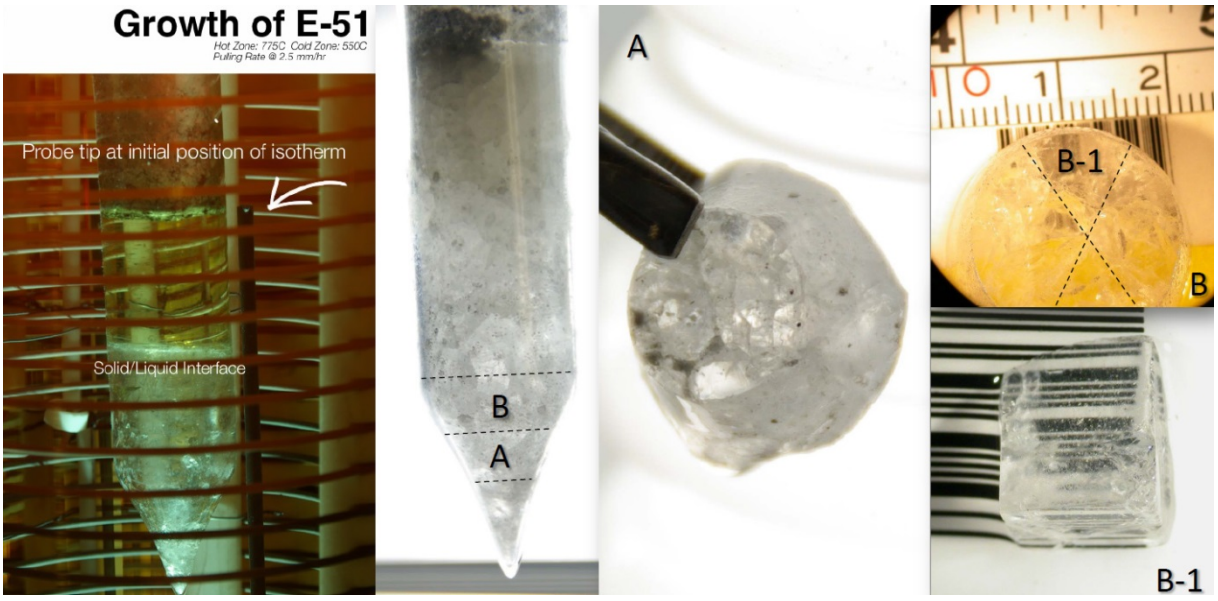

Figure 26. Left to right: The growing crystal with observed solid liquid interface. The boule at room temperature backlit with fluorescent light. The lower section removed from the boule showing a polycrystalline appearance. A portion of the boule with a large grain exhibiting improved clarity but with small inclusions.

4.3.3 Thermal Gradient and Annealing as Process Variables

The following growth experiments would address the supercooling and interface control issues by the introduction of a grain selecting capillary tip ampoule geometry and a furnace diaphragm insert as described in the preceding chapter respectively. The capillary tip geometry was first used in a sample labeled E-66 but contained a flaw whereby the neck within the capillary was too narrow and prevented the melt from fully flowing into it. This was compounded by the presence of contaminants within the synthesized material which prevented it from fully filtering into the growth chamber and thus the effort to grow E-66 was abandoned. As a result, the neck in the capillary tip was made broader in subsequent experiments to promote complete flow of the melt into it.

In order to make comparisons of resultant crystal quality as functions of process variables such as thermal gradient, pulling rate and cooling procedures, three identical samples were prepared with no variance of their synthesis or handling procedures and loaded into identical ampoules employing the fritted ampoule for filtering of the melt prior to growth. These samples provided the first opportunity to investigate the effectiveness of an added diaphragm within the furnace in order to enhance the thermal gradient and to capture the results with direct observation techniques.

While special attention was given to reproduce the handling procedures for each sample, unfortunately all three samples were prepared using a faulty vacuum fitting which allowed the material to be exposed to trace amounts of ambient oxygen and moisture during vacuum heating which manifested in a melt with a dark reddish color, likely due to the presence of metal oxides in the material. In addition to a darker melt color, the last to freeze portion of each sample was observed to have a depressed freezing point due to the presence of additional impurities caused by their segregation and concentration during directional solidification.

E-68-1 –Observations with Diaphragm Insert with Large Thermal Gradient

Two growth attempts using the diaphragm were conducted using pulling rates of 1 mm/hr and zone settings of 825°C/525°C representing a very large thermal gradient. In each attempt, the large gradient at the diaphragm produced a flat, featureless SLI which maintained its shape and position within the furnace which resulted in stable growth of a single grain. In Figure 27, the growth interface can be seen within the capillary above the diaphragm early on during growth. The interface remained approximately flat and featureless upon reaching the full diameter and migrated to within the thickness of the diaphragm and thus was occluded from view.

A secondary grain was seen to nucleate approximately 70% into growth. The nucleation originated from the area of the ampoule closest to a tear in the diaphragm which introduced a large curvature of the critical isotherm. This observation illustrated the sensitivity of the growth interface to small disturbances of the melting point isotherm under a severe thermal gradient. After all melt had solidified and had cooled approximately 150°C below the melting point, parallel bands of inclusions caused by constitutional supercooling during growth can be seen in the boule in Figure 28. Crack nucleation and propagation was directly observed during this experiment. During growth, the $CsCe_2Cl_7$ melt and crystal appear to wet the surface of the quartz ampoule and as the crystal thermally contracts upon cooling below the diaphragm, small transverse cracks nucleate from the crystal-ampoule interface resulting from the release of stress as the bond between the crystal and quartz is broken. Large thermal gradients along the crystal produce

aggressive and uneven detachment processes which produce fine transverse cracks along the entire length as seen in a similar study by Feigelson (*54*). This is likely caused by a weak chemical bond between crystal and the quartz surface. Upon further cooling to room temperature at 4°C/hr, the transverse cracks caused during the detachment process propagate through the crystal while additional finer cracking can be seen developing as well despite the slow cooling rate.

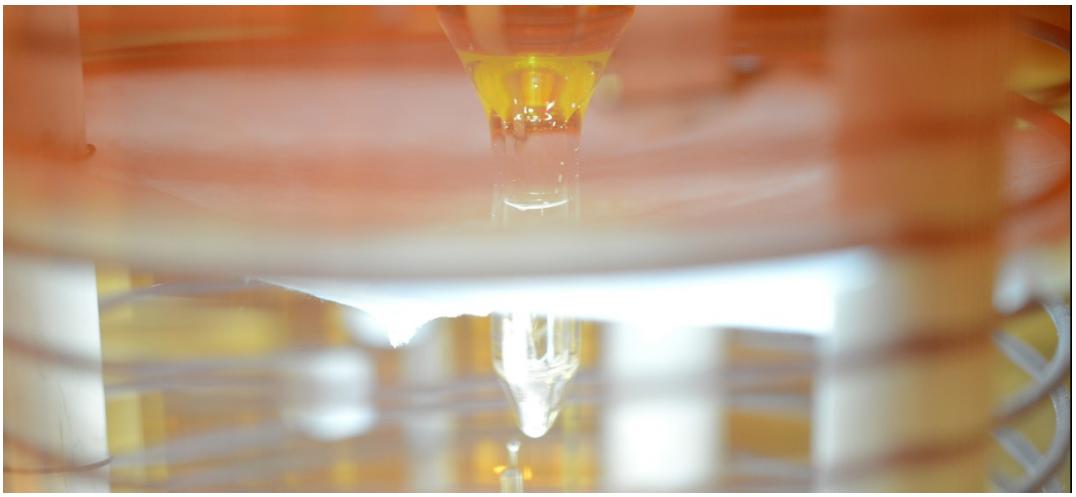

Figure 27. The flattened and stable interface produced with the use of the diaphragm inserted between the heaters of the transparent furnace.

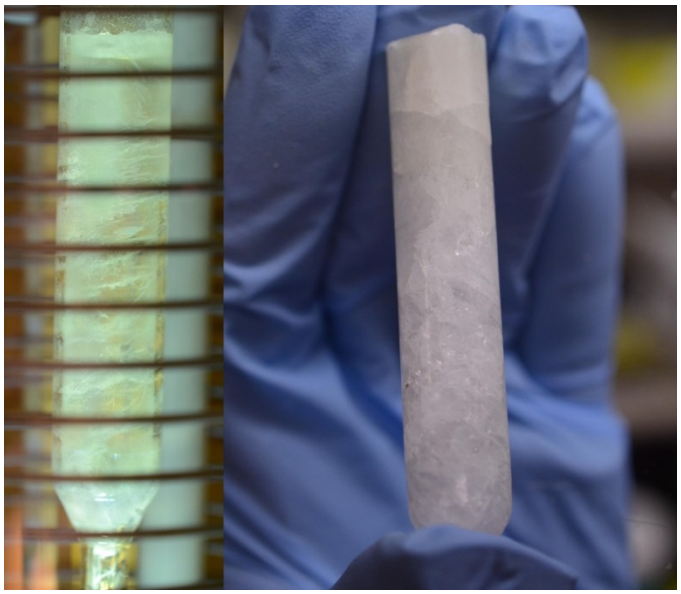

Figure 28. Inclusions bands in the boule prior to cooling (left). The boule removed from the ampoule exhibiting severe cracking.

E-68-2 Observations with Diaphragm Insert with Small Thermal Gradient

The aggressive detachment of the crystal from the ampoule wall under severe gradient conditions seen in growth experiments with E-68-1 provided motivation to investigate the cracking behavior during growth under less severe gradient conditions, with the hypothesis that the reduced gradient may lessen crack formation at the expense of controlling the growth interface. A minimal gradient of approximately 5°C/cm was achieved through zone settings of 725°C/675°C. A pulling rate of 1 mm/hr was used.

A concave interface was observed to develop in the capillary above a polycrystalline seed at the beginning of growth and increase in concavity throughout growth as seen with E-51. The rejection of impurities to the radial center perpetuated the concavity of the interface and a breakdown of the growth interface was observed as the concentration of impurities reached a critical point, whereby spontaneous nucleation is captured after approximately 80% of the crystal had solidified as seen in Figure 29.

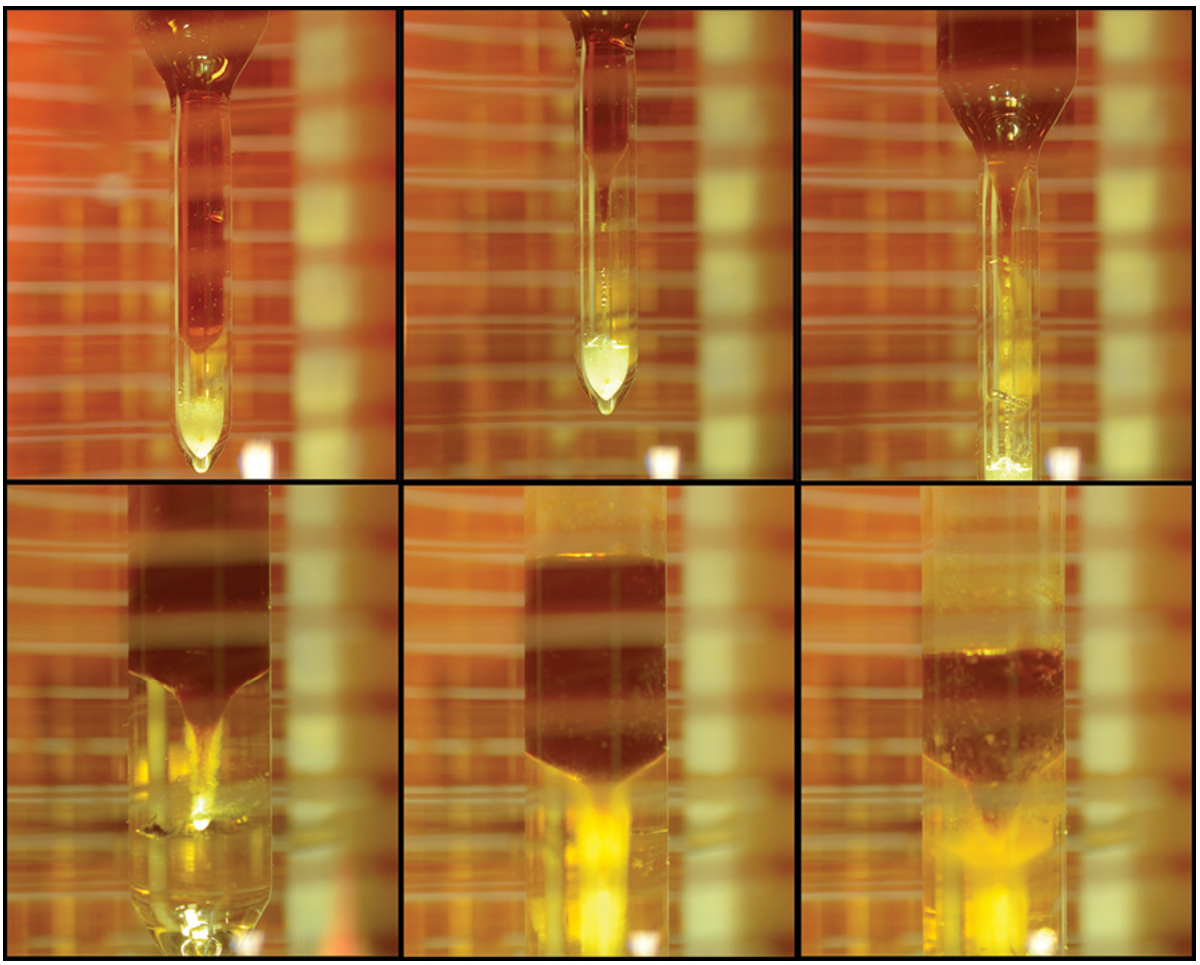

Figure 29. Series of images from the timelapse of growth under minimal gradient. The concave interface causes a core of defects to develop in the radial center of the boule. The growth interface is seen to partially breakdown in the lower right frame due to a buildup of impurities in the melt.

The reduction in gradient was observed to prevent aggressive detachment of the crystal from the ampoule wall yet inclusion bands and severe cracking were observed upon cooling at 4°C/hr. In order to aid in the relaxation of any residual stresses in an attempt to reduce the cracking behavior, a subsequent growth experiment was conducted with identical gradients and pulling rates but with an introduced annealing step whereby after solidification, the boule was held at 640°C for 24 hours prior to cooling to room temperature. The 24-hour annealing close to the melting point produced a minor improvement on the cracking severity as seen in Figure 30.

The growth experiments on E-68-1 and E-68-2 comprised the two extremes of thermal gradients as the growth process variable and resulted in differences in the onset of cracking yet the severity of cracking was similar upon cooling. An experiment with the identically prepared sample E-68-3 would use a thermal gradient process variable between the two extreme thermal gradients and utilize the 24-zone Mellen furnace to carefully control the thermal profile without the use of a diaphragm insert.

E-68-3 – Use of a Moderate Gradient for Growth in the 24-Zone Mellen Furnace

Using the 24-zone Mellen furnace, E-68-3 was grown at 1 mm per hour pulling rate, and a moderate gradient of approximately 15°C/cm, and a 48 hour annealing step prior to cooling to room temperature at 4°C/hr. The results again show a boule with severe cracking yet slightly improved over the non-annealed and 24 hour annealed boule suggesting that the cracking will occur irrespective of furnace, with only a small dependence on the thermal gradient used. This observation also suggests that attempts to prevent thermal induced cracking from removal of residual stresses through high temperature annealing is ineffective at worst and provides a minor improvement at best as seen in Figure 31.

Figure 30. The E-68-2 boule at room temperature without annealing step prior to cooling (top) and with 24 annealing step (bottom). The additional procedure produces a minor improvement to the cracking behavior.

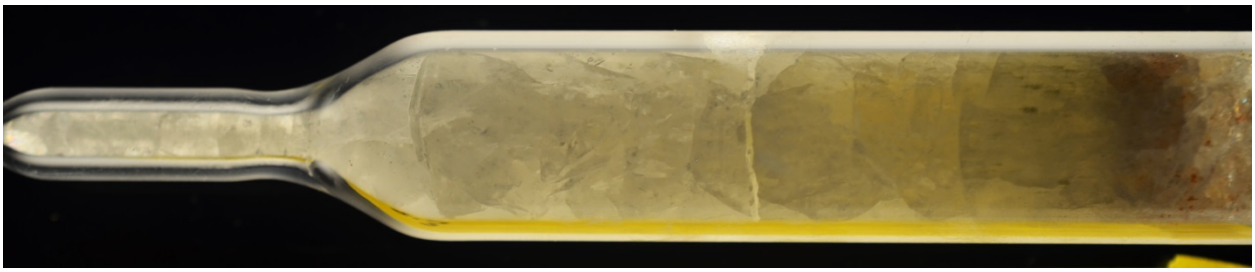

Figure 31. Boule E-68-3 at room temperature after a 48-hour high temperature annealing step exhibiting only minor improvement to the cracking behavior.

The growth experiments of E-44, E-51, and E-68 series samples all shared a common procedure which included a separate synthesis step prior to loading into the growth ampoule. In order to assess how this may play a role in the quality of the resultant crystal, subsequent growth experiments would implement a different handling method. Additionally, the use of the annealing step prior to cooling would continue to be included in the experimental process to facilitate a comparison with previous results.

4.3.4 Potential Volatilization Concerns

In order to investigate the advantages and disadvantages of combining the synthesis and growth into a single ampoule, the E-77 and E-82 samples were produced using simplified procedures thereby eliminating the fritted ampoule and removing the material transfer step which is thought to introduce unnecessary exposure to the synthesized material prior to growth. Furthermore, a review of Lisek, Kapala, and Miller's investigation of the partial pressures of gaseous species over the melts of various compositions in the $CsCl\text{-}CeCl_3$ system in (*55*) suggest that complexes containing Cs^+ and Cl^- volatize from the melt in much larger quantities than Ce^{3+} containing complexes and thus a melt reaching equilibrium with the high vacuum above it would shift away from the initial composition towards a melt richer in Ce. This hypothesis is further supported by inductively coupled plasma mass spectrometry (ICP-MS) measurement of E-68-2 indicating a shift from the stoichiometric Cs-Ce balance of approximately 2.2 mol % from a 1:2 ratio of $CsCl\text{-}CeCl_3$ (See appendix A for ICP-MS report of $CsCe_2Cl_7$).

Thus in order to address a potential for inhomogeneous volatilization of the melt, the volume above the melt was minimized for E-77 and E-82, where the former was sealed under vacuum and the latter was sealed with a partial pressure of dry argon to limit evaporation of the melt.

E-77 was grown in the 24-zone Mellen furnace similarly to E-68-3, with identical pulling rates, but with zone settings slightly cooler to minimize overheating the melt to further reduce volatility. An additional 48 hour high temperature annealing step prior to cooling to room temperature at 4°C/hr was also used. The results are shown in Figure 32.

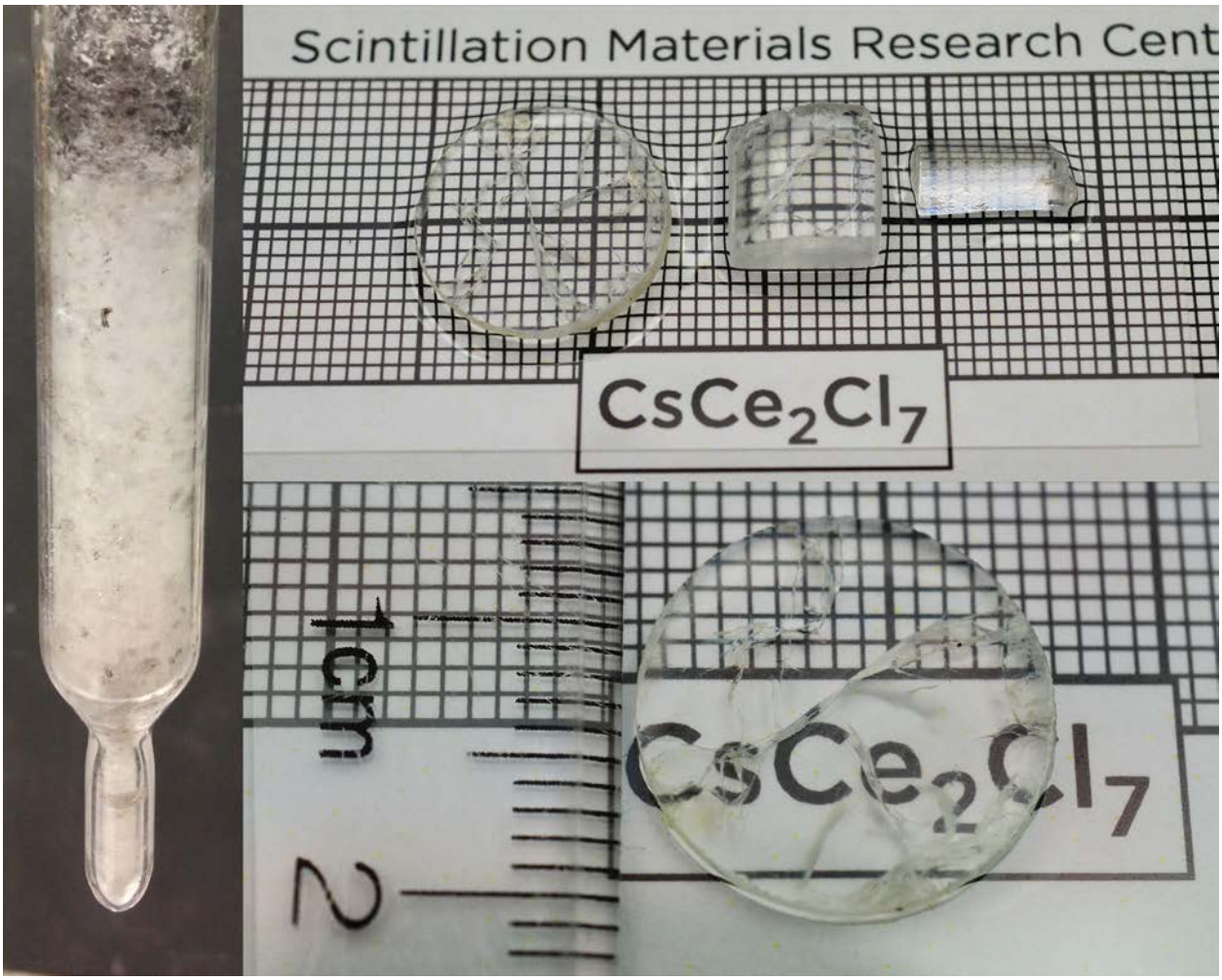

Figure 32. The E-77 boule after growth (left). Portions cut and polished from the boule exhibiting excellent clarity and a reduced cracking behavior with no evidence of visible inclusions.

E-77 produced a crystal with severe cracking but was limited to the first to freeze and last to freeze sections of the boule with reduced cracking in the center. Upon removal of the boule from the ampoule, the crystal fell apart revealing a section in the middle of the axial length containing large uncracked portions with excellent clarity. Portions were cut and polished from this section and shown in Figure 32. This result represents the first incidence when a complete slab of a single crystal could be cut from the boule that would not fall apart due to the severity of the cracking. Because of the improved quality, the single crystals produced in this experiment provided the material used for the aforementioned Laue diffraction studies and structural refinement.

E-82 was grown in the transparent furnace to further investigate the cracking behavior with measures to reduce volatilization. Special attention was paid to controlling the shape and position of the interface during growth through tuning the furnace zone settings to achieve a flattened or slightly convex interface

while minimizing the thermal gradient on the crystal to reduce aggressive detachment observed to cause premature cracking of the boule. During synthesis, the additional overpressure of argon prohibited degassing of the melt and resulted in gas bubbles adhering to the inner surface of the ampoule along the entire length of the melt. Despite the presence of the gas bubbles, growth of a single grain with a preferable flat or slightly convex growth interface was achieved and is illustrated in Figure 33.

The boule was also annealed close to the melting point for 48 hours prior to cooling to room temperature at 4°C/hr similiarly to E-77. While no cracking was observed during growth or annealing, the boule developed fine cracking along the first and last to freeze regions leaving a portion in the axial center with large uncracked grains of excellent clarity also observed with E-77. A photo of the boule with transmitted light is seen in Figure 34.

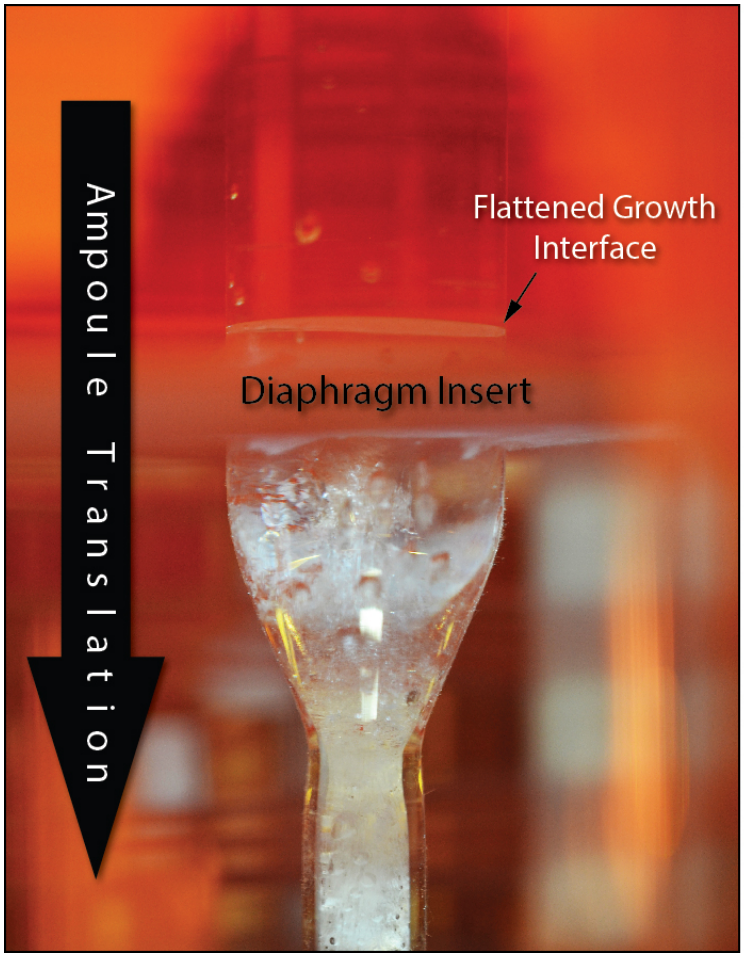

Figure 33. E-82 during growth with a flat to slightly convex interface between the melt and crystal. Gas bubbles adhering to the inner ampoule wall are attributed to the argon gas overpressure which prohibited complete degassing of the melt during synthesis.

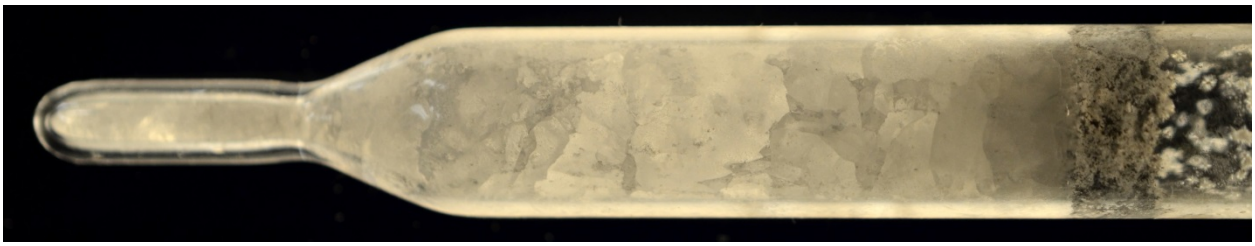

Figure 34. Boule E-82 grown with an argon gas partial pressure over the melt to reduce volatilization. A marked reduction in cracking is observed in a small portion in axial center of the boule. Note the solid condensate in the upper portions of the ampoule indicative of irreversible metal halide volatilization from the melt.

The growth experiments of E-77 and E-82 provided evidence that implementing countermeasures to reduce volatilization of the melt produces improvement to the size of uncracked portions yet the cracking behavior is still pervasive. An effort to further investigate the effects of shifts from the initial melt composition now follows.

4.3.5 The Effect of Non-stoichiometric Starting Composition on Crystal Quality

The issue of unbalanced volatilization of one component from the melt affecting crystal quality has been reported in literature for the Bridgman growth of $AgGaS_2$ as well as the Czochralski growth of langasite ($La_3Ga_5Si_{14}$) (*56, 57*). In the case of growth of $AgGaS_2$, a cloudy crystal is produced from the stoichiometric starting mixture due to volatilization but clarity is restored by annealing in an atmosphere loaded with additional Ag_2S after growth. That study also concluded that optically clear crystals could be grown from a starting mixture containing an excess of Ag_2S but was deemed impracticable due to the more effective annealing process. In the case of growth with langasite, an off stoichiometric starting mixture containing a Ga/Si ratio of 5.2 was considered optimal to produce crystals with minimal cracking. These published studies provided a motivation to conduct growth experiments with off stoichiometric starting compositions of $CsCe_2Cl_7$ to determine whether any affect to the cracking behavior could be observed.

Several 4 g samples containing compositions deviating from the stoichiometric mixture of $CsCe_2Cl_7$ were synthesized and grown with accelerated process variables of 3 mm/hr pulling rate and 25°C/hr cooling rate within 6 mm diameter quartz ampoules and a qualitative comparison of their crystal quality was used to determine an ideal composition to conduct a larger growth study. Of the compositions listed in Table 5, the composition with 1.66 mol % excess CsCl exhibited superior grain clarity and cracking behavior compared with the others. Thus a 37.5 gram charge of $CsCe_2Cl_7$ was prepared with an excess of 1.66 mol % of CsCl for growth in the transparent furnace with identical process variables to E-82 for comparison. The results of this growth experiment now follow.

The molten charge of E-91 was seen to not fully synthesize over a 24 hour period at the synthesis temperature prior to growth evidenced by some un-melted beads presumed to be $CeCl_3$. As a result of this observation, the melt containing ampoule was gently shaken for several minutes while inside the furnace in order to facilitate complete mixing. After an additional 24 hours at the synthesis temperature, there was no visual evidence of any un-melted beads and the growth process was continued.

Table 6. List of Screened Off-Stoichiometric Compositions of $CsCe_2Cl_7$.

Composition (excess in mol%)
2.66 % CsCl
2.00% CsCl
1.66% CsCl
1.12% CsCl
0.66% CsCl
Control
0.8% $CeCl_3$

While using zone settings of 745°C/585°C and diaphragm insert similar to E-82, the crystal was observed to supercool during initial self-seeding (Figure 35). The captured images show the supercooled melt was limited to the grain selecting capillary tip indicating that the 60°C thermal gradient characteristic of supercooling in $CsCe_2Cl_7$ was within the length of the capillary tip as previously described in Chapter 3. Further growth through the necked region produced a single grain which emerged to grow at the full 15 mm diameter.

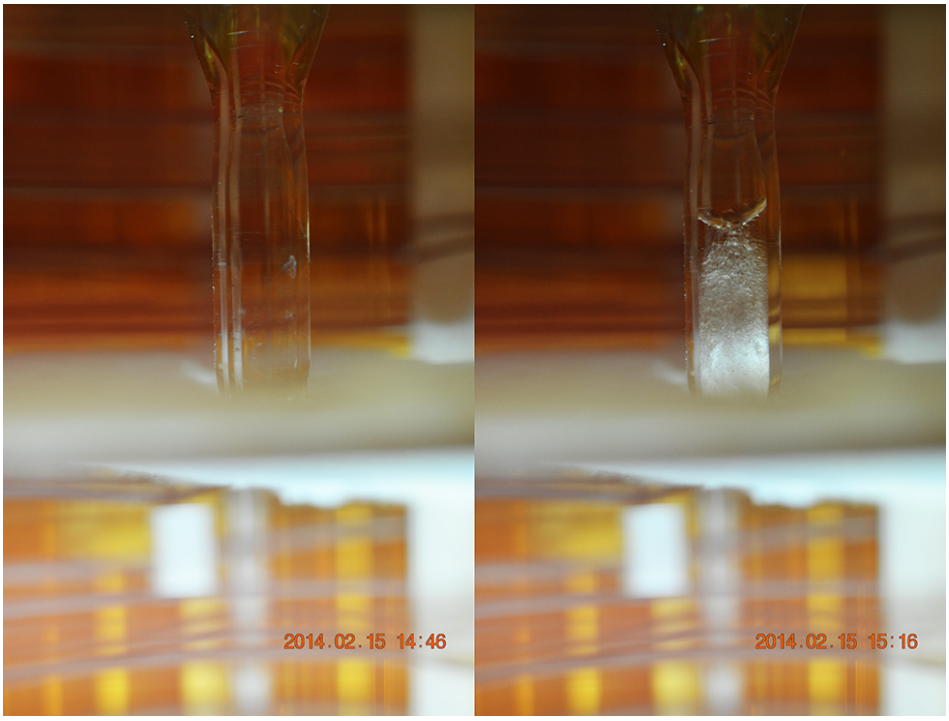

Figure 35. The $CsCe_2Cl_7$ supercooling during the self-seeding process aided by the grain selecting capillary geometry. 30 minutes and 0.5 mm of translation separate the supercooled melt in the left frame, with the spontaneous nucleation of numerous crystallites in the right frame.

The detachment from the ampoule of the crystal during growth was observed to produce minimal cracking at the crystal ampoule surface and an axially aligned crack developed prior to cooling. The residual melt remaining at the last to freeze portion was measured to freeze at approximately 530°C indicative of the eutectic composition on the CsCl side of the phase diagram illustrated in Figure 1. This observation indicates that the excess CsCl was effectively rejected by the solidifying $CsCe_2Cl_7$ phase at the growth rate of 1 mm/hr.

The boule was photographed with transmitted light at high temperature during cooling to reveal the interior defect structure evolution over time. The boule appeared to develop minor parallel bands of inclusions oriented approximately normal to the growth direction with only minor crack propagation during cooling from melt to 250°C as seen in Figure 36.

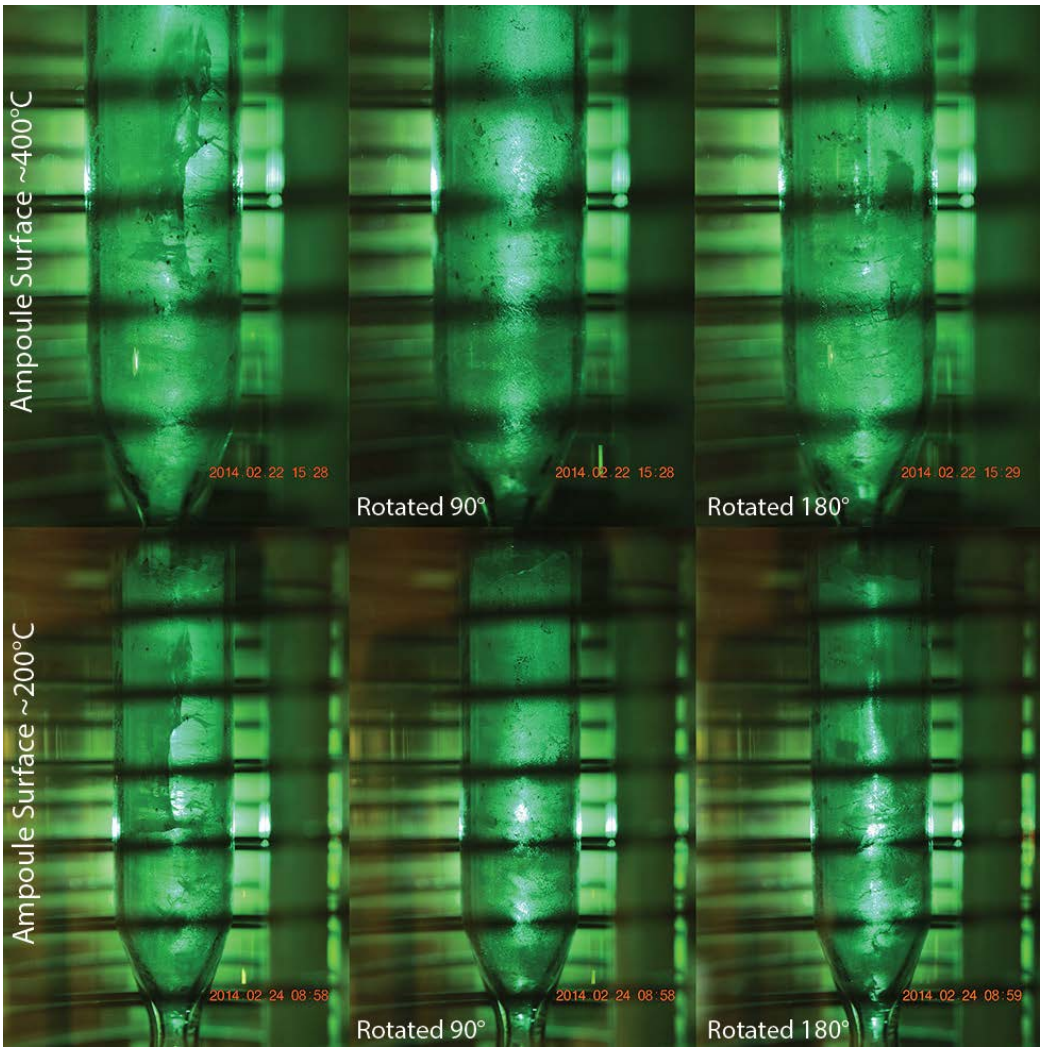

Figure 36. E-91 during cooling. The top frames show the boule at 400°C while the lower frames show only minor crack propagation at 200°C.

Upon extraction from the ampoule at room temperature, the crystal exhibited improved structural integrity as the entire boule was able to be polished to highlight excellent transparency through the entire 15 mm thickness. A 3 mm slab cut from the lower portion was polished to study the macroscopic defect structures. Transmitted polarized light reveals minor strain fields oriented along the direction of inclusion bands. Microphotographs of the inclusion bands reveal a spherule shape of individual inclusions comprising the bands (Figure 37).

The growth experiment of off-stoichiometric $CsCe_2Cl_7$ with excess 1.66 mol % CsCl produced a boule with greatly improved cracking behavior and clarity over previous attempts, without the use of an annealing step prior to cooling at 4°C/hr. The presence of minor strain fields in the E-91 crystal indicate a residual stress likely attributed to the presence of inclusions during the cooling process yet are minimal compared with strain fields observed in E-44 which appear parallel to much larger inclusion bands filling the entire volume. The growth of a singular grain was achieved through tuning zone settings in tandem with the use of the furnace diaphragm to produce an optimized thermal profile which was a compromise between growth stability and aggressive detachment induced cracking at the crystal-ampoule interface. The next section provides some basic scintillation performance characterization on the material grown under this study.

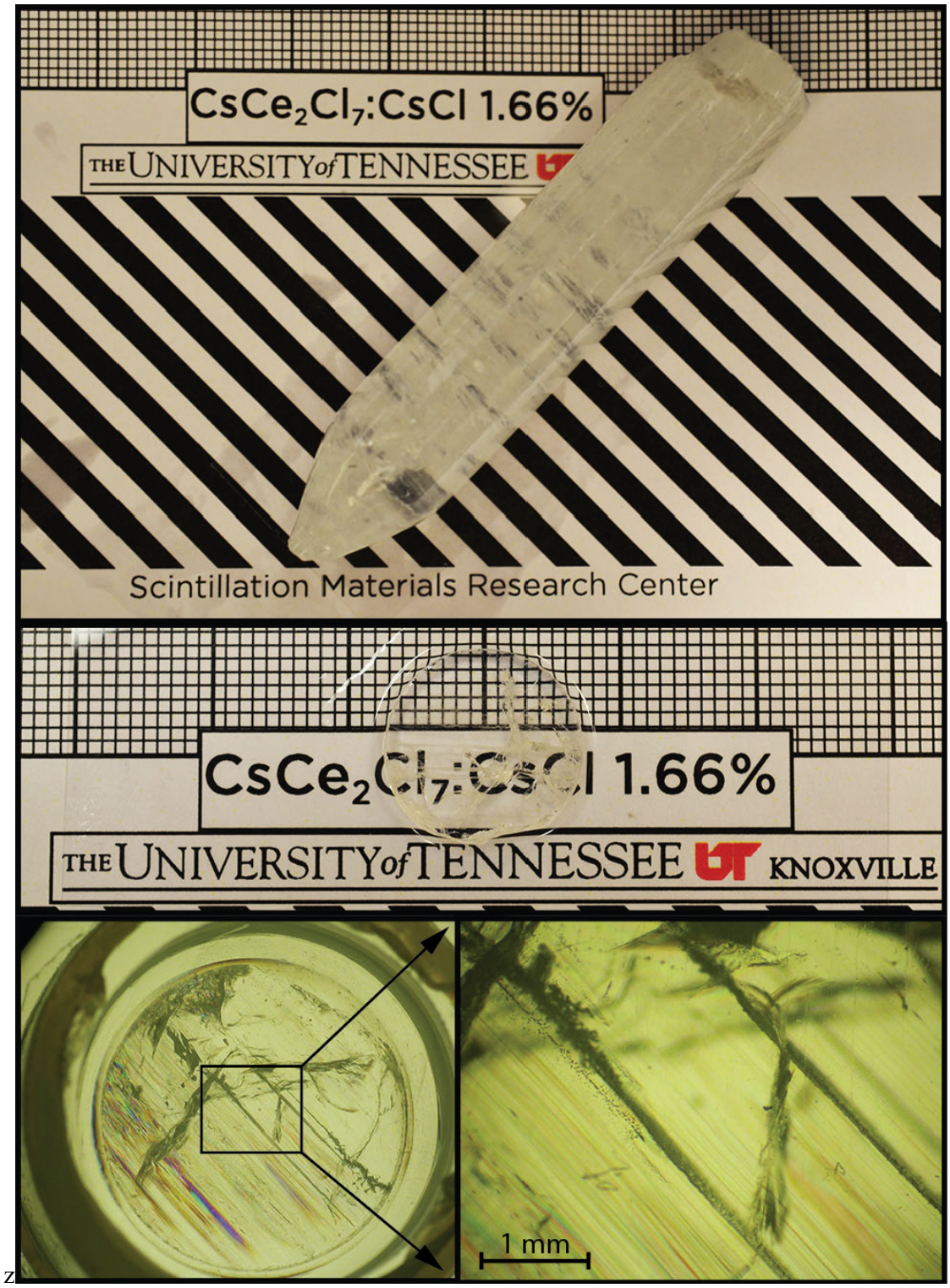

Figure 37. From top to bottom: The polished boule of E-91 showing good translucency through the full 15 mm thickness. A 3 mm thick polished slab taken from the lower portion of the boule. Microphotographs showing the strain field oriented along inclusion bands comprised of individual spherule inclusions.

4.4 Scintillation Performance Characterization

The absolute light yield was calculated from the position of the photopeak of the gamma response spectrum under excitation of 662 keV gammas from a ^{137}Cs source. The pulse height provided from this spectrum at a specific gain setting was then compared with the single photo electron (SPE) peak position which is produced under maximum gain settings to capture the thermally produced electron from the photocathode within the PMT. The radioluminescence spectrum of each sample was then used to determine an integral quantum efficiency value based upon the wavelength dependent quantum efficiency tables provided by the PMT manufacturer. In this manner, the fraction of emitted scintillation photons produced in the crystal that produce a photoelectron at the first dynode of the PMT is determined. A plot of calculated absolute light yield for each sample is shown in Figure 38. Because of a statistically large dependence on the SPE peak position, the calculated light yields for SPE values taken with a shaping time of 0.5 μs as well as 2.0 μs are included as error bars with the symbol located at the mean value.

The 662 keV photopeak from each spectrum was fitted with a Gauss function and the energy resolution was derived by dividing the full width at half maximum (FWHM) by the position of the peak centroid, both given as channels produced by the multichannel analyzer (MCA).

The light yield amongst all samples varied between approximately 25,000 and 26,500 ph/MeV with energy resolutions between 9.0 and 11.0%. Additionally, given the best conditions for energy resolution measurements, a small uncracked sample from boule E-77 was measured to produce a value of 7% for the 662 keV photopeak. This spectrum is shown in Figure 39. The improved measured energy resolution can be attributed to isolating a small portion of the crystal that was free of inclusions and cracks and using the Hamamatsu 6231-100 PMT which provides a higher quantum efficiency over the 3177-50 PMT.

The proportionality of response (nonproportionality) to gamma sources of various energies is shown in Figure 40 with $CsCe_2Cl_7$ along with a comparison of $LaCl_3$ and NaI(Tl). The result indicates that $CsCe_2Cl_7$ has a nonproportionality of approximately 87% of the ideal response in the 10-40 keV range when normalized to the 662 keV response. While not approaching the ideal response as can be seen in the plot of $LaCl_3$, this indicates a good proportionality when compared with LSO:Ce and NaI:Tl at similar energies (*58*).

1.5 mm thick polished plates of each sample were measured for transmittance of ultraviolet (UV), visible (VIS), and near infrared (NIR) light as a function of % transmitted versus wavelength. This measurement provided a direct measurement of the band gap of $CsCe_2Cl_7$ where for each sample a transmittance edge located at approximately 354 nm which corresponds to an energy gap between the valence band and conduction band of 3.5 eV. While an objective comparison of the maximum transmittance of each sample is difficult to produce due slight variances in surface finish, the samples from E-77, E-82, and E-91 showed superior transmittance at nearly all wavelengths with E-91 having a maximum transmittance of approximately 86%. The results indicate that the off stoichiometric starting mixture used in E-91 produced a boule with the least amount of light scattering defects affecting the light transmittance through the crystal. The plot of transmittance curves for all measured samples is shown in Figure 41.

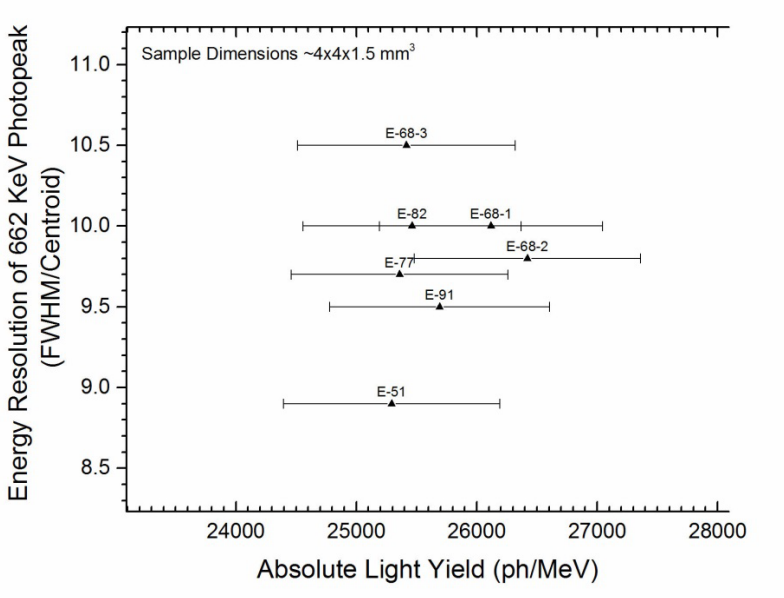

Figure 38. Absolute light yield versus energy resolution of the 662 keV photopeak for all grown samples of $CsCe_2Cl_7$.

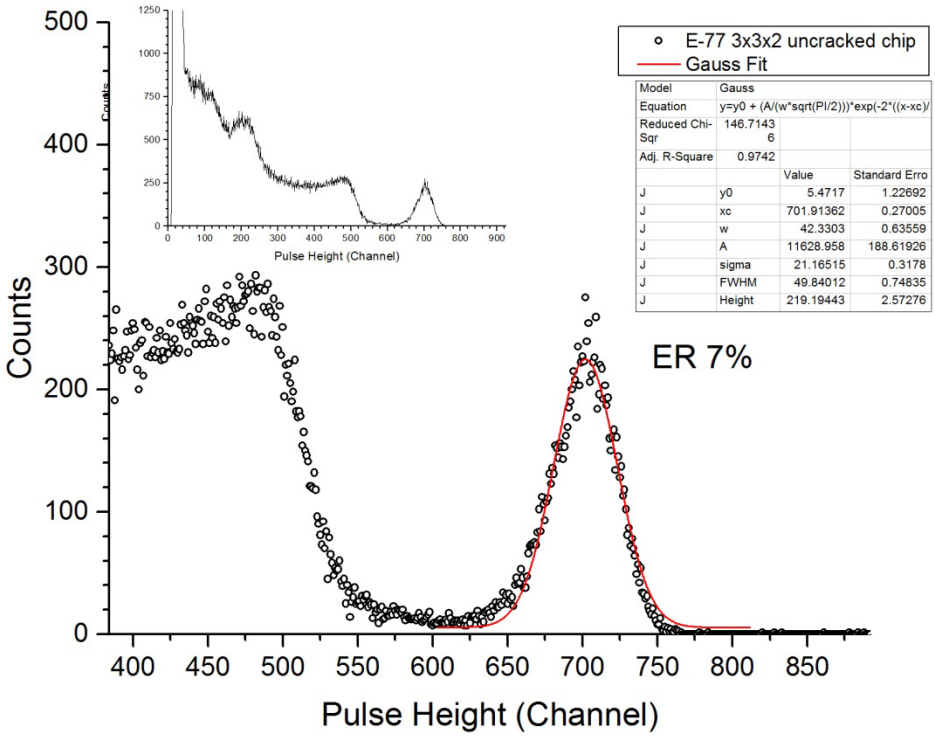

Figure 39. Gamma response spectra of $CsCe_2Cl_7$ under excitation by the 662 keV gamma from a ^{137}Cs source. Inset image contains entire spectra with linear scale.

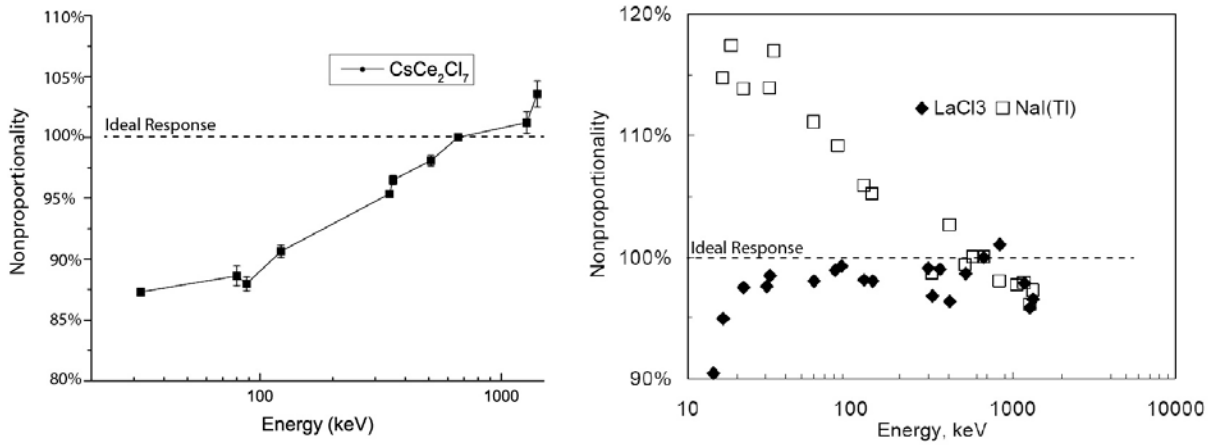

Figure 40. Left: Non proportionality of response of $CsCe_2Cl_7$ to various excitation energies. Right: Non proportionality of $LaCl_3$:Ce and NaI(Tl) Plot on right taken from (*59*).

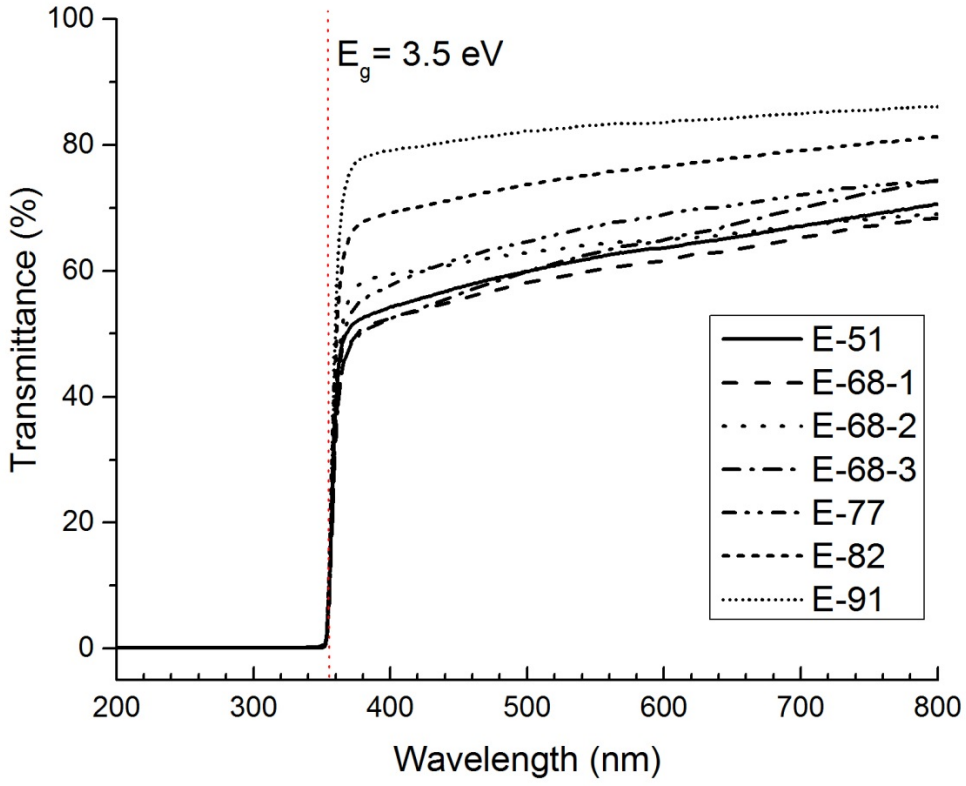

Figure 41. Transmittance measurement of $CsCe_2Cl_7$ samples grown in this study. A band gap of 3.5 eV is clearly indicated for all specimens measured.

Radioluminescence at 300 K of all samples are shown in Figure 42. The broad emission peak is asymmetrically centered at approximately 385 nm. Sample to sample variations in the tail extending into the longer wavelengths can be attributed to slight differences in crystal quality and purity. E-82 is shown to have the most pronounced tail and the argon backfill unique to this sample may be correlated as the gas supply may have introduced additional oxygen impurities.

The photoluminescence of one sample is shown in Figure 43. The emission band similar to what is seen in the radioluminescence spectrum was produced under excitation at 300 nm while the excitation for the emission at 383 nm is seen to overlap. The calculated Stokes shift is approximately 0.25 eV. This plot illustrates the large degree of self-absorption in $CsCe_2Cl_7$ as the emission band produced by the Ce^{3+} 5d-f4 transition produces a double peak emission in which the higher energy emission is reabsorbed by another

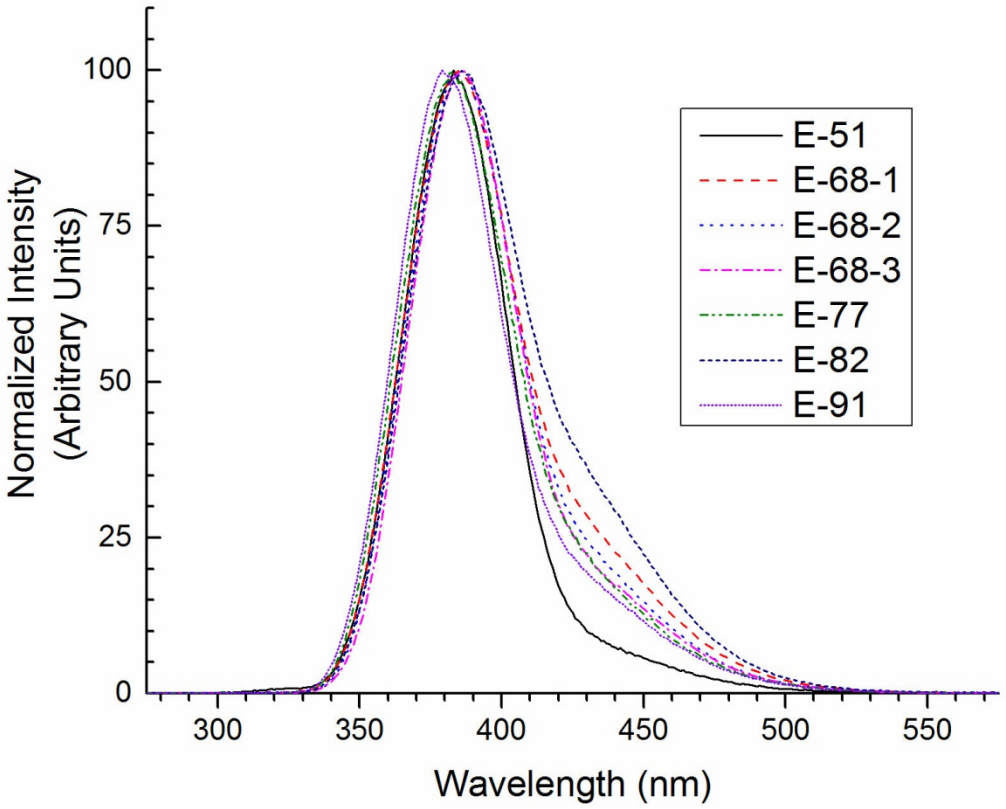

Figure 42. The radioluminescence of all samples showing a maximum emission wavelength at approximately 385 nm.

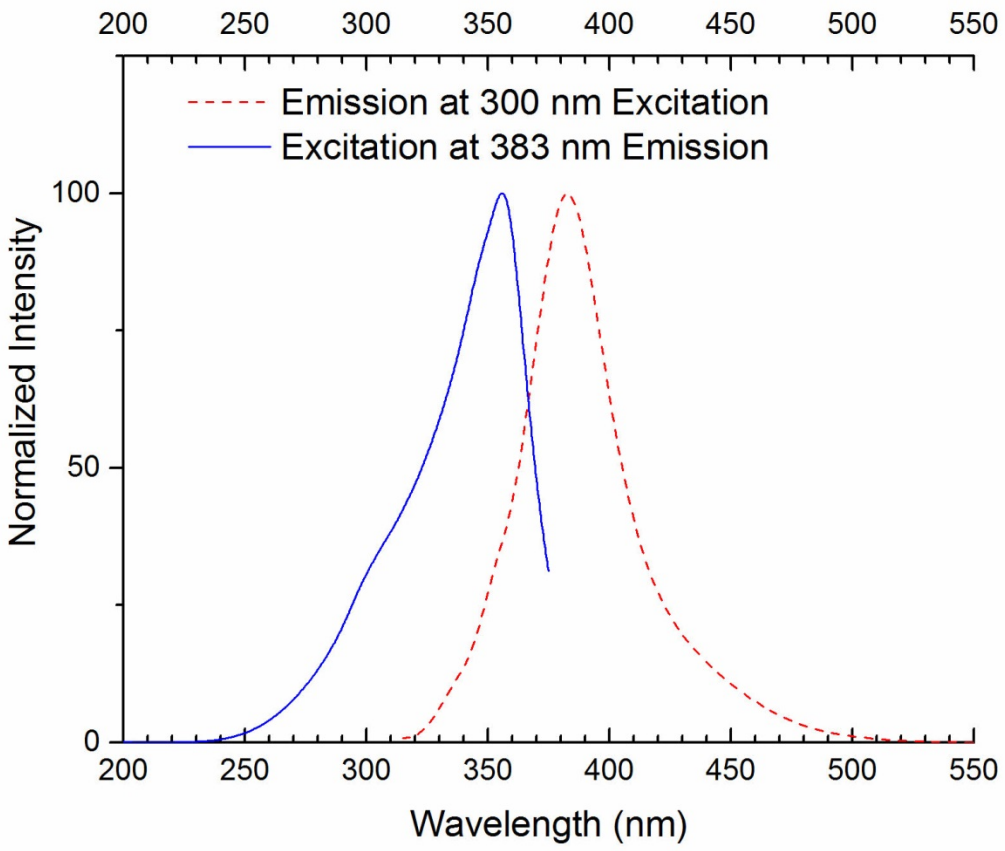

Figure 43. Photoluminescence emission and excitation spectrum of $CsCe_2Cl_7$ showing a large overlap of the absorption and emission bands.

Ce^{3+} site in the crystal as seen in a similar study on $CeBr_3$ in (*60*). The higher energy emission peak is only visible as a slight shoulder in emission band at approximately 350 nm.

The results from scintillation performance characterization reveal the limitation of energy resolution needed for isotope identification in security applications is largely attributed to the non-proportionality of the response (nPR) to various excitation energies. According to Dorenbos's paper (*61*) on non-proportionality and its link to energy resolution in pulse height spectra, the total measured energy resolution is a function of the variations in charge collection and multiplication in the PMT, as well as the intrinsic resolution of the scintillator. While the former is limited to Poisson's statistics due to the photoelectron yield in the PMT, the latter contribution to the resolution is a function of inhomogeneity in the crystal affecting the uniformity of the ionization track of the incident X-ray or gamma-ray. In addition to inhomogeneity, the intrinsic resolution is also attributed to the phenomenon of nPR in the crystal which causes the scintillation light yield (ph/MeV) to be dependent on the energy of the ionizing radiation. From

these analyses, the inhomogeneity in terms of an activator or luminescence center is assumed to be a nonfactor as Ce^{3+} is a major intrinsic component of $CsCe_2Cl_7$. Thus a large component of the decreased energy resolution must stem from the nPR of the crystal. Moreover, there would be two ways to increase the energy resolution in $CsCe_2Cl_7$, increase the light yield or improve the nPR. At the time of this study, no studies could be found on Ce^{3+} containing intrinsic scintillators which substantially increase the light yield. However an empirical study on the aliovalent doping of another intrinsic Ce^{3+} containing scintillator by Quarati et al (*62*) has shown to improve the nPR and increase the measured energy resolution from 4 to 3% for the 662 keV in $CeBr_3$. This constitutes an improvement of 25% to energy resolution and a future study employing this approach may expect similar gains in $CsCe_2Cl_7$.

The growth experiments of 8 unique samples of $CsCe_2Cl_7$ produced crystals with a large variance of total boule quality with respect to the presence of macroscopic cracking and inclusions yet small sections of each sample performed similarly under light yield with more variation in measured energy resolution. This result indicates that although the growth conditions and handling influenced the macroscopic appearance and cracking severity, changes to these protocols had a limited effect on the light yield while variations in energy resolution are attributed to variations in sample quality from boule to boule. Furthermore, because intact slabs of thickness larger than a few mm could only be produced from E-91 due to the severe cracking in the other boules, a comparison of the scintillation performance for larger dimensions was impossible.

A list of material properties found in literature along with those compiled in this study for $CsCe_2Cl_7$ are listed in Table 7 in the appendix section at the end of this manuscript.

Chapter 5. Conclusion

An investigation of the crystal growth of $CsCe_2Cl_7$ from the melt using the Bridgman method with various process variables has been presented. An in situ method of continuously observing crystal growth processes using high resolution time lapse photography has been developed to aid in the investigation of crystal growth of novel materials. Results have shown that limiting the ampoule volume above the melt during synthesis and growth prevents excessive volatilization from the melt while additional CsCl added to the melt further compensates this and reduces formation of inclusions due to supercooling and produces a more complete synthesis and abatement of crack nucleation. The prevention of secondary grain formation was shown to be effectively prevented through use of grain selecting ampoule geometry to promote self-seeding processes in conjunction with control over the crystal/melt interface during growth through tailoring the thermal gradient with the use of additional insulating diaphragms.

Many thermophysical properties pertaining to crystal synthesis and handling of $CsCe_2Cl_7$ have been determined for the first time under this study:

- The characteristic supercooling of $CsCe_2Cl_7$ was shown to be substantial at approximately 60°C through differential scanning calorimetry measurements.
- The hygroscopicity of $CsCe_2Cl_7$ is small in comparison with nearly every metal halide scintillator in advanced development providing a superior advantage in handling and packaging protocols.
- The monoclinic crystal structure has been refined through definitive single crystal Laue diffraction analyses and a crystallographic information file has been made available for future reference.
- The anisotropic thermal expansion coefficients have been determined through temperature dependent powder diffraction analyses and do not indicate a prohibitively large degree of anisotropy.

Additionally, the energy band gap of $CsCe_2Cl_7$ has been experimentally determined through transmission measurements for the first time.

Moreover, while minor cracking is still present in boules of 15 mm in diameter, yields of uncracked portions greater than 1 cm^3 are possible with the improved crystal synthesis procedures developed in this study. The existence of inclusions regardless of cracking still remains a cause of concern to the overall crystal quality and further research would be required to develop processes which obviate their formation. Furthermore, no significant improvements were seen in the scintillation performance as a result of the improved synthesis and due to this, an energy resolution surpassing that of NaI:Tl for 662 keV gamma rays is presently not possible with $CsCe_2Cl_7$ and thus do not justify further consideration for growth at larger volumes unless improvements can be made in this performance area.

Future Outlook

Continuing research on the source of non-proportionality in $CsCe_2Cl_7$ should produce improvements to the energy resolution and enhance the chances of further development in domestic security applications.

Future growth efforts will benefit from an ampoule wall coating of carbon or use of carbon crucibles to reduce adhesion between crystal and quartz seen to produce cracking from detachment upon cooling. Moreover, incorporating an active mixing mechanism into growth such as the accelerated crucible rotation method may improve synthesis of the melt and decrease supercooling effects shown to form inclusions.

The continuous observation equipment along with the transparent growth station developed in this study will continue to act as investigational tool in the growth of novel metal halide scintillators in the future.

List of References

1. G. F. Knoll, in *Radiation detection and measurement.* (Wiley, 2000), pp. 405-406.
2. G. F. Knoll, in *Radiation detection and measurement.* (Wiley, 2000), pp. 308-312.
3. P. Lecoq, A. Annenkov, A. Gektin, M. Korzhik, C. Pedrini. (Springer, Berlin, Heidelberg, 2006), pp. 23-26.
4. A. Yoshikawa, V. Chani, M. Nikl, Czochralski Growth and Properties of Scintillating Crystals. *Acta Physica Polonica, A.* 124, (2013).
5. R. Hofstadter, Alkali Halide Scintillation Counters. *Physical Review* 74, 100 (1948).
6. M. Moszyński *et al.*, Intrinsic energy resolution of NaI(Tl). *Nuclear Instruments and Methods in Physics Research Section A: Accelerators, Spectrometers, Detectors and Associated Equipment* 484, 259 (2002).
7. A. Iltis *et al.*, Lanthanum halide scintillators: Properties and applications. *Nuclear Instruments & Methods in Physics Research Section a-Accelerators Spectrometers Detectors and Associated Equipment* 563, 359 (Jul, 2006).
8. A. Giaz *et al.*, Characterization of large volume 3.5″ ×8″ LaBr3:Ce detectors. *Nuclear Instruments and Methods in Physics Research Section A: Accelerators, Spectrometers, Detectors and Associated Equipment* 729, 910 (11/21/, 2013).
9. M. J. Harrison *et al.* (2010), vol. 7806, pp. 14.
10. Y. Yokota, K. Nishimoto, S. Kurosawa, D. Totsuka, A. Yoshikawa, Crystal growth of Eu:SrI2 single crystals by micro-pulling-down method and the scintillation properties. *Journal of Crystal Growth* 375, 49 (2013).
11. R. Hawrami *et al.*, Bridgman bulk growth and scintillation measurements of SrI2:Eu2+. *Journal of Crystal Growth* 379, 69 (Sep, 2013).
12. L. A. Boatner *et al.*, Bridgman growth of large SrI2:Eu2+ single crystals: A high-performance scintillator for radiation detection applications. *Journal of Crystal Growth* 379, 63 (Sep, 2013).
13. L. Alaribe *et al.*, in *MRS Proceedings*. (Cambridge Univ Press, 2011), vol. 1341.
14. J. Glodo, R. Hawrami, K. S. Shah, Development of Cs2LiYCl6 scintillator. *Journal of Crystal Growth* 379, 73 (2013).
15. E. V. van Loef *et al.*, Crystal Growth and Scintillation Properties of Strontium Iodide Scintillators. *IEEE Trans. Nucl. Sci.* 56, 869 (Jun, 2009).
16. G. Bizarri, E. D. Bourret-Courchesne, Y. Zewu, S. E. Derenzo, Scintillation and Optical Properties of BaBrI:Eu2+ and CsBa2I5:Eu2+. *Nuclear Science, IEEE Transactions on* 58, 3403 (2011).
17. Z. Yan *et al.*, Eu2+-activated BaCl2, BaBr2 and BaI2 scintillators revisited. *Nuclear Instruments and Methods in Physics Research Section A: Accelerators, Spectrometers, Detectors and Associated Equipment* 735, 83 (2014).
18. G. Rooh *et al.*, The growth and scintillation properties of CsCe2Cl7 crystal. *Journal of Crystal Growth* 311, 128 (Dec 15, 2008).
19. M. Zhuravleva, K. Yang, C. L. Melcher, Crystal growth and scintillation properties of Cs3CeCl6 and CsCe2Cl7. *Journal of Crystal Growth* 318, 809 (2011).

20. I. C. Sun, I. S. Morozov, Vzaimodeistvie Khloridov Redkozemelnykh Metallov s Khloridami Shchelochnykh i Shchelochnozemelnykh Metallov. *Zhurnal Neorganicheskoi Khimii* 3, 1914 (1958).
21. J. Kapala, I. Rutkowska, Thermodynamic properties of the pseudo-binary CsCl-LnCl(3) (Ln = Ce, Pr, Nd) systems. *Calphad-Comput. Coupling Ph. Diagrams Thermochem.* 28, 275 (Sep, 2004).
22. M. Gaune-Escard, L. Rycerz, W. Szczepaniak, A. Bogacz, Entropies of phase transitions in the M3LnCl6 compounds (M=K, Rb, Cs; Ln=La, Ce, Pr, Nd) and K2LaCl5. *J. Alloy. Compd.* 204, 189 (1994).
23. G. N. Papatheodorou, O. J. Kleppa, Thermodynamic studies of binary charge unsymmetrical fused salt systems. Cerium(III) chloride-alkali chloride mixtures. *The Journal of Physical Chemistry* 78, 178 (1974/01/01, 1974).
24. H. J. Seifert, Ternary chlorides of the trivalent early lanthanides - Phase diagrams, crystal structures and thermodynamic properties. *J. Therm. Anal. Calorim.* 67, 789 (2002).
25. P. W. Bridgman, Certain Physical Properties of Single Crystals of Tungsten, Antimony, Bismuth, Tellurium, Cadmium, Zinc, and Tin. *Proceedings of the American Academy of Arts and Sciences* 60, 305 (1925).
26. D. C. Stockbarger, The production of large single crystals of lithium fluoride. *Rev. Sci. Instrum.* 7, 133 (Mar, 1936).
27. C. E. Chang, W. R. Wilcox, Control of Interface Shape in Vertical Bridgman-Stockbarger Technique. *Journal of Crystal Growth* 21, 135 (1974).
28. T. W. Fu, W. R. Wilcox, Influence of Insulation on Stability of Interface Shape and Position in the Vertical Bridgman-Stockbarger Technique. *Journal of Crystal Growth* 48, 416 (1980).
29. F. C. Frank, Supercooling of Liquids. *Proceedings of the Royal Society of London Series a-Mathematical and Physical Sciences* 215, 43 (1952).
30. M. E. Glicksman, *Principles of Solidification An Introduction to Modern Casting and Crystal Growth Concepts*. SpringerLink, Ed., (New York, NY : Springer Science+Business Media, LLC, New York, NY, 2011).
31. W. A. Tiller, K. A. Jackson, J. W. Rutter, B. Chalmers, The Redistribution of Solute Atoms During the Solidification of Metals. *Acta Metallurgica* 1, 428 (1953).
32. D. T. J. Hurle, Constitutional supercooling during crystal growth from stirred melts—I: Theoretical. *Solid-State Electronics* 3, 37 (1961).
33. J. W. Rutter, B. Chalmers, A Prismatic Substructure Formed During Solidification of Metals. *Can. J. Phys.* 31, 15 (1953).
34. K. Sangwal, Effects of impurities on crystal growth processes. *Progress in Crystal Growth and Characterization of Materials* 32, 3 (1996).
35. K. Sangwal, K. W. Benz, Impurity striations in crystals. *Progress in Crystal Growth and Characterization of Materials* 32, 135 (1996).
36. H. Fang, L. Zheng, H. Zhang, Y. Hong, Q. Deng, Reducing melt inclusion by submerged heater or baffle for optical crystal growth. *Cryst. Growth Des.* 8, 1840 (Jun, 2008).
37. N. N. Greenwood, *Chemistry of the elements*. A. Earnshaw, Ed., (Butterworth-Heinemann, Oxford. Boston, 1997).

38. **P. Lecoq, A. Annenkov, A. Gektin, M. Korzhik, C. Pedrini, A. Annenkov, A. Gektin, M. Korzhik, C. Pedrini, Eds. (Springer, Berlin, Heidelberg, 2006), pp. 124-173.**
39. **K. Yang, M. Zhuravleva, C. L. Melcher, P. Szupryczynski. (Google Patents, 2011).**
40. **M. Zhuravleva, K. M. Yang, C. L. Melcher, P. Szupryczynski. (Google Patents, European, 2011).**
41. **M. Zhuravleva, K. Yang, C. L. Melcher, Crystal growth and scintillation properties of Cs3CeC16 and CsCe2Cl7. *Journal of Crystal Growth* 318, 809 (Mar, 2011).**
42. **O. Guillot-Noel *et al.*, Scintillation properties of RbGd2Br7 : Ce advantages and limitations. *IEEE Trans. Nucl. Sci.* 46, 1274 (Oct, 1999).**
43. **S. B. Derenzo, M. Weber, M. Brennan, K., http://scintillator.lbl.gov/ (2013).**
44. **G. Meyer, The Synthesis and Structures of Complex Rare-Earth-Halides. *Progress in Solid State Chemistry* 14, 141 (1982).**
45. **G. Meyer, KDy2Cl7 and RbDy2Cl7, Phyllochlorodysprosates(iii) with Face-sharing and Edge-sharing Monocapped Trigonal Prisms. *Zeitschrift Fur Anorganische Und Allgemeine Chemie* 491, 217 (1982).**
46. **G. Meyer, P. Ax, A. Cromm, H. Linzmeier, Seven-coordinate trivalent rare earths: the phyllochlorides ARE2Cl7 (A = K, Rb, Cs; RE = Sm - Lu, Y) and the crystal structure of InY2Cl7. *Journal of the Less-Common Metals* 98, 323 (1984).**
47. **Z. A. Jones, P. Sarin, R. P. Haggerty, W. M. Kriven, CTEAS: a graphical-user-interface-based program to determine thermal expansion from high-temperature X-ray diffraction. *Journal of Applied Crystallography* 46, 550 (Apr, 2013).**
48. **L. F. Siah, W. M. Kriven, J. Schneider, In situ, high-temperature, synchrotron, powder diffraction studies of oxide systems in air, using a thermal-image furnace. *Measurement Science & Technology* 16, 1291 (Jun, 2005).**
49. **S. C. Bates, K. S. Knight, D. W. Yoel, in *Space Technology and Applications International Forum,* M. S. ElGenk, Ed. (Amer Inst Physics, Melville, 1998), pp. 711-717.**
50. **E. Niwa, K. Masumoto, Growth of AgGaS2 single crystals by a self-seeding vertical gradient freezing method. *Journal of Crystal Growth* 192, 354 (Aug, 1998).**
51. **N. Cherepy *et al.*, in *SPIE Optical Engineering+ Applications*. (International Society for Optics and Photonics, 2009), pp. 74490F-74490F-6.**
52. **P. Meincke, G. Graham, The thermal expansion of alkali halides. *Can. J. Phys.* 43, 1853 (1965).**
53. **E. W. Lemmon, R. T. Jacobsen, S. G. Penoncello, D. G. Friend, Thermodynamic properties of air and mixtures of nitrogen, argon, and oxygen from 60 to 2000 K at pressures to 2000 MPa. *J. Phys. Chem. Ref. Data* 29, 331 (May-Jun, 2000).**
54. **R. S. Feigelson, R. K. Route, Vertical Bridgman Growth of CdGeAs2 with Control of Interface Shape and Orientation. *Journal of Crystal Growth* 49, 261 (1980).**
55. **I. Lisek, J. Kapala, M. Miller, Thermodynamic study of the CsCl-CeCl3 system by Knudsen effusion mass spectrometry. *J. Alloy. Compd.* 280, 77 (Oct, 1998).**
56. **R. S. Feigelson, R. K. Route, Recent Developments in the Growth of Chalcopyrite Crystals for Nonlinear Infrared Applications. *Opt. Eng.* 26, 113 (Feb, 1987).**

57. **H. Takeda, K. Shimamura, V. I. Chani, T. Fukuda, Effect of starting melt composition on crystal growth of La3Ga5SiO14. *Journal of Crystal Growth* 197, 204 (1999).**

58. **M. Moszyński, Energy resolution and non-proportionality of scintillation detectors – new observations. *Radiation Measurements* 45, 372 (2010).**

59. **M. Balcerzyk, M. Moszyński, M. Kapusta, Comparison of LaCl3:Ce and NaI(Tl) scintillators in γ-ray spectrometry. *Nuclear Instruments and Methods in Physics Research Section A: Accelerators, Spectrometers, Detectors and Associated Equipment* 537, 50 (1/21/, 2005).**

60. **D. N. ter Weele, D. R. Schaart, P. Dorenbos, The Effect of Self-Absorption on the Scintillation Properties of Ce3+ Activated LaBr3 and CeBr3. *Nuclear Science, IEEE Transactions on* 61, 683 (2014).**

61. **P. Dorenbos, J. T. M. de Haas, C. W. E. Van Eijk, Non-proportionality in the scintillation response and the energy resolution obtainable with scintillation crystals. *Nuclear Science, IEEE Transactions on* 42, 2190 (1995).**

62. **F. G. A. Quarati, M. S. Alekhin, K. W. Kramer, P. Dorenbos, Co-doping of CeBr3 scintillator detectors for energy resolution enhancement. *Nuclear Instruments & Methods in Physics Research Section a-Accelerators Spectrometers Detectors and Associated Equipment* 735, 655 (Jan, 2014).**

Appendix

CsCe2Cl7

E-68-2 CsCe 2C17

Element	Concentration [% wt]
Ce	43.8
Eu	-
K	-
Sr	-
Cs	*14

* Analyzed by ICP-MS

Figure 44. ICP-MS compositional analysis of sample E-68-2 indicating an excess of Ce from the stoichiometric balance in $CsCe_2Cl_7$

Table 7. Table of Structural, Thermophysical, and Scintillation Properties of $CsCe_2Cl_7$.

Chemical Formula	$CsCe_2Cl_7$
Atomic Mass (g/mol)	661.3084
Crystal System	Monoclinic
Space Group	P21/b
Formula Units	16
a (Å)	19.365(1)
b (Å)	19.385(9)
c (Å)	14.876(1)
Gamma (°)	119.83(4)
Volume of Unit Cell ($Å^3$)	4844.506
Density (g/cm^3)	3.6
Z-eff	48
Thermal Expansion along a ($K^{-1} \times 10^{-5}$)	2.13
Thermal Expansion along b ($K^{-1} \times 10^{-5}$)	2.67
Thermal Expansion along c ($K^{-1} \times 10^{-5}$)	2.71
Anisotropy in α	≈0.8
Melting Point (°C)	672
Mass Change over 60 mins at 40% RH (%)	≈0.2
Characteristic Supercooling (°C)	≈60
Scintillation Decay Time (ns)	50
Light Output (ph/MeV)	≈25,500
Eres at 662 keV (%)	≈7-8
Emission Wavelength Max (nm)	385
Band Gap (eV)	≈3.5
Nonproportionality (nPR) to 14 keV	0.87

Vita

Adam Coleman Lindsey has spent the majority of his life living in eastern Tennessee and attended East Tennessee State University where he earned his Bachelor of Science degree in 2004. There he studied 3D visualization and animation. Adam spent several years working at a family restaurant business developing his management and people skills where he met his wife, Lisa. Together they are happy parents of four legged critters. Before pursuing material science and engineering, Adam briefly assisted his father in an optics startup company based in California and provided him with a flavor of engineering first hand. An avid fan of civil engineer/writer Henry Petroski, and professor at Northeast State Community College Dr. Mark Pollock, they instilled within Adam a desire to enter into the challenging field of engineering and make a difference through application of “slightly less common sense”. Adam has a passion for cooking, music, archery, the outdoors, and working with his hands. His motto is “the joy lies within the struggle”.